Manipulating the inverse Faraday effect using inversely designed plasmonic nanostructures

Ye Mou

Sorbonne Université

Physique en Île-de-France (ED 564)

Institut des NanoSciences de Paris / Nanophotonique et optique quantique

Manipuler l'effet Faraday inverse par l'utilisation de nanostructures plasmoniques inversement conçues

Par Ye MOU

Thèse de doctorat de la physique

Dirigée par Mathieu MIVELLE

Présentée et soutenue publiquement le 24 Juin 2024

Devant un jury composé de :

DELEPORTE Emmanuelle	Professeure	Présidente du jury
BOER-DUCHEMIN Elizabeth	Professeure	Rapporteure
GERARD Davy	Maître de conférences	Rapporteur
BONOD Nicolas	Directeur de recherche	Examinateur
GRESILLON Samuel	Maître de conférences	Examinateur
MIVELLE Mathieu	Chargé de recherche	Directeur de thèse

To see a World in a Grain of Sand

And a Heaven in a Wild Flower

Hold Infinity in the palm of your hand

And Eternity in an hour

"**Auguries of Innocence**" by William Blake

Acknowledgments

First and foremost, I want to express my deepest gratitude to my Ph.D. supervisor, Mr. Mathieu Mivelle, for supervising me during the past three years. His unwavering support, continuous encouragement, insightful feedback, professional expertise and single-minded dedication have been instrumental in fostering my growth as a young researcher in science. Without his patient guidance, selfless help and exceptional mentorship, there is no doubt that I could not finish my research projects successfully and complete this Ph.D. thesis on time.

Secondly, I want to extend my sincere appreciation to all my colleagues at the Institut des NanoSciences de Paris (INSP) - UMR 7588 as well as the collaborators outside of the laboratory with whom I worked. Their wholehearted support, diverse perspectives and insightful discussions helped me a lot and enriched my Ph.D. research journey. I will never ever forget that. Also, I am deeply thankful to Sorbonne University, CNRS and INSP for providing me with essential resources, facilities, and opportunities for conducting this Ph.D. research. The academic environment and research infrastructure at the university and laboratory have been remarkably beneficial to my academic growth and professional development.

Thirdly, I also want to express my genuine appreciation to Prof. Hervé Aubert and Prof. Junwu Tao who are both from INP-ENSEEIHT in Toulouse for writing recommendation letters for me when I applied for the Ph.D. program of Sorbonne University. Additionally, I want to thank one of my best friends Xingyu Yang who is now a fourth-year Ph.D. candidate in our group. Meaningful discussions with him in physics as well as his technique support are warmly acknowledged.

Furthermore, I would like to acknowledge the China Scholarship Council (Grant No. 202108070083) for financially supporting my study in France for three years. Moreover, other funding agencies such as the Agence National de la Recherche (ANR-20-CE09-0031-01), the Institut de Physique du CNRS (Tremplin@INP 2020) and the doctoral school ED 564 Physique en Île-de-France are also greatly appreciated.

In addition, I want to express my profound gratitude to the members of my Ph.D. thesis committee for their valuable input, constructive criticism, and comprehensive guidance, which have significantly improved the quality of this thesis.

Last but not least, I want to extend my heartfelt gratitude to my family especially my parents who are in China right now. Their support, encouragement, patience, understanding, sacrifice and belief have been a constant source of motivation giving me energy and inspiring me to move forward. I love them forever!

Ye Mou

June 2024

Contents

General introduction

There are seven chapters in total in this manuscript and it is organized as follows: one state-of-the-art chapter, one theory chapter regarding to the inverse Faraday effect in metals, one chapter focus on inverse design including numerical simulation and optimization parts, three chapters of manipulating the inverse Faraday effect using inversely designed plasmonic nanostructures in different aspects and one general conclusion chapter where I will present some perspective for this work as well.

Chapter 1: State of the art. In this first chapter, a small introduction is shown in the section 1.1 at the beginning of the chapter. The motivation of my Ph.D. is discussed in the section1.2. In the section 1.3, the inverse Faraday effect in general is briefly described. After that, the plasmonic nano-antennas and their abilities of manipulating light are reviewed in the section 1.4. Then in the section 1.5, the recent experimental results from Matthew Sheldon's group demonstrating the inverse Faraday effect in plasmonic gold nanoparticles are presented shortly. Finally, a conclusion part is given in the section 1.6.

Chapter 2: The origin of the inverse Faraday effect in metals. The chapter 2 serves as a theoretical part of the manuscript related to the inverse Faraday effect in metals. In the section 2.1, the flow of the theory as an introduction part is described concisely. The theory of inverse Faraday effect in metals based on R. Hertel's work is discussed. After that, a simplified version of conduction process of drift currents' formula is presented in the section 2.2. Then in the section 2.4, stationary magnetic field induced by drift currents is described using the Biot-Savart law. Section 2.5 reviews the state of the art about manipulating the inverse Faraday effect by using plasmonic nano-antennas. Finally, section 2.6 presents a conclusion of manipulating the inverse Faraday effect using plasmonic nanostructures as a short introduction of following chapters.

Chapter 3: Inverse design for plasmonic nano-antennas. The chapter 3 presents a powerful concept i.e., inverse design which is useful for optimizing plasmonic nano-antennas in order to further manipulate the inverse Faraday effect. In the section 3.1, the Finite-Difference Time-Domain (FDTD) method and basic plasmonic nanostructure is introduced. In the section 3.2, the numerical FDTD method and the commercial FDTD software Lumerical are both presented and discussed. Lastly, section 3.3 includes the optimization parts which

contains three sub-sections: topology optimization, objective function and metaheuristic algorithm.

Chapter 4: A chiral inverse Faraday effect. In this chapter, we demonstrate that the inverse Faraday effect can be chiral, i.e., occurring for only one single helicity of incoming light, by using an inversely designed plasmonic nano-antenna to manipulate light locally at the nanoscale. This is the first aspect of manipulating the inverse Faraday effect by using plasmonic nanostructures.

Chapter 5: A reversed inverse Faraday effect. In this chapter, using an inverse-designed plasmonic nano-antenna, we illustrate that the magneto-optical process of the inverse Faraday effect can be a reversed mechanism compared to the so-called "classical" inverse Faraday effect. This serves as the second aspect of manipulating the inverse Faraday effect by using plasmonic nanostructures.

Chapter 6: Femtosecond drift photocurrents. In this chapter, two types of nanostructures for generating unidirectional femtosecond drift photocurrents are discussed. In the section 6.1, photocurrent and its application are briefly introduced. In the section 6.2, by maximizing the in-plane stationary magnetic field due to the inverse Faraday effect, an inversely designed plasmonic nano-antenna is optimized and investigated for generation unidirectional drift photocurrents at the center of the structure which can be used as a tuneable THz nanosource. Inspired by the inverse-designed nanostructure and a recent theoretical work from our group about the linear inverse Faraday effect, section 6.3 presents a relatively simple nanodevice containing nanorods positioned close to a gold nanostrip which could be used for generation of unidirectional photocurrents at the origin of the inverse Faraday effect. Furthermore, both simulation and experimental results are discussed, and they present a good agreement. Overall, this presents the third aspect of manipulating the inverse Faraday effect by using plasmonic nanostructures.

Chapter 7: General conclusion and perspective. In this chapter, a general conclusion is given where I also discuss about some perspective about the Ph.D. project.

This Ph.D. thesis demonstrates that the inverse Faraday effect can be manipulated by using inversely designed plasmonic nanostructures in different aspects. We are confident that this will lead to numerous applications in research fields such as ultrafast data storage and data

processing, magnetic skyrmion, magnetic circular dichroism, nanoscale THz spectroscopy, and many others.

Chapter 1 State of the art

1.1 Introduction

In this chapter, I will firstly discuss about the motivation of my Ph.D. project. After that. the inverse Faraday effect will be introduced and the state of the art about the inverse Faraday effect, plasmonic nano-antenna and the recent experimental results about the inverse Faraday effect in plasmonic gold nanoparticles will be also described.

1.2 Motivation

While the electronic industry has successfully entered the nanoworld following Moore's law, the speed of manipulating and storing data lags, creating the so-called ultrafast technology gap. Processors already have a clock speed of a few gigahertz, while the storage on a magnetic hard disk requires a few nanoseconds. This bottleneck can also be found in magnetic random access memory devices.

The use of ultrafast pulses of light has demonstrated effectiveness in manipulating magnetic orders on very short time scales. However, the physical processes involved are still poorly understood, and such a control reaches the micrometer scale at best, effectively preventing their use for high-density data storage.

This Ph.D. research project aims to develop an entirely new approach to manipulating magnetic domains based on the engineering of plasmonic nanodevices. These devices optically generate ultrashort, intense, and reversible pulses of stationary magnetic fields at the nanoscale, a challenge that no other technique can achieve so far.

For that purpose, we engineer innovative inversely designed plasmonic nanostructures to tailor light-matter interactions at the nanoscale. Under the right illumination conditions, the electromagnetic fields generated by the nanostructure set the electrons in a metal (such as in a coil) in pseudo-continuous drift motion, in turn yielding the creation of a strong stationary magnetic field.

By specifically creating and manipulating ultrafast, strong, confined, and reversible pulses of magnetic fields in an all-optical fashion, we will enable the manipulation of magnetic

domains at the nanoscale and over very short timescales (a few tens of femtoseconds), opening the way to applications in ultrafast data storage and data processing. As well it will also open entirely new horizons in technological and research areas as diverse as electron spin manipulation, spin precession, spin current, and spin waves, in improving the capability to control the acceleration of charged particles in laser-plasma interaction or nano-MRI studies, amongst others.

1.3 Inverse Faraday effect

In optics, the inverse Faraday effect is the effect opposite to the Faraday effect. The Faraday effect is a phenomenon that describes the interaction between light and a magnetic field in a material [1-3]. Specifically, it describes the rotation of the light polarization in the material as a function of the amplitude of an external magnetic field oriented in the direction of light propagation. Conversely, the inverse Faraday effect (IFE) is a magneto-optical process enabling the magnetization of matter by optical excitations only.

The inverse Faraday effect, discovered in the 60s [1-3] and described in different materials, dielectric or metallic, is the result of non-linear forces that light applies to the material's electrons [4-7]. The principle of the inverse Faraday effect is shown in Figure 1.1. A circularly polarized electromagnetic wave is launched on a material generating, in turn, a static magnetization $\boldsymbol{M}$ of the latter. This magnetization is proportional to the vector product $\boldsymbol{E}(\omega)\times\boldsymbol{E}^{*}(\omega)$, with $\boldsymbol{E}$ the complex form of the optical electric fields oscillating at the angular frequency ω, the star * represents the complex conjugate and bold characters are vectors (same for the whole manuscript). Although it has been shown that the inverse Faraday effect could occur in optical beams carrying an orbital angular momentum [8], this expression shows that only a circularly or elliptically polarized light will generate this magnetization. Particularly, a right-circular polarization (RCP in red color in the Figure 1.1) will create a static magnetization in the direction of light propagation. In contrast, a left-circular polarization (LCP in green color in the Figure 1.1) will do so in the opposite direction to the propagation. In addition, the induced static magnetization $\boldsymbol{M}$ is comparable to the saturated magnetization of the material.

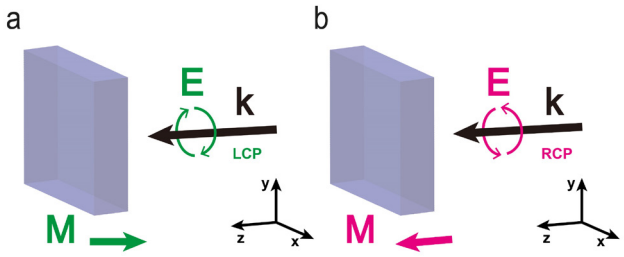

Figure 1.1 *: Principle of the inverse Faraday effect. A circularly polarized electromagnetic wave magnetizes a material. This magnetization is oriented a) against the direction of the wave propagation when the light is left circularly polarized and b) in the direction of the light propagation when it is right circularly polarized.*

Particularly, in this Ph.D. manuscript, it should be noted that only the inverse Faraday effect occurring in plasmonic nano-antennas will be investigated and discussed.

1.4 Plasmonic nano-antenna

Plasmonic nano-antennas are nanoscale structures designed to manipulate the interaction between light and matter. These nanodevices are able to provide enhanced and controllable light-matter interactions and strong coupling between far-field radiation and localized sources at the nanoscale [9]. Different research communities benefit from the field of plasmonic nano-antennas, as it holds the potential for very promising and unprecedented subwavelength light-matter interactions, strong coupling between far-field radiation and localized sources at the nanoscale, generation of strong field gradients locally, as well as the exciting possibilities of realizing efficient wireless links between optical nanocircuit components [9-14].

Due to plasmonic nano-antennas' ability to manipulate light at the nanoscale, they can strongly enhance optical electromagnetic fields and generate strong field gradients locally. For example, Yiqin Chen et al. [15] illustrated that through a topology optimization to inversely design a metallic nanoparticle dimer with the goal of optimizing the near-field enhancement factor in its sub-10 nm gap, they finally obtained an optimized plasmonic nanostructure shown in the Figure 1.2a with high near-field electric field enhancement in the gap (Figure 1.2b).

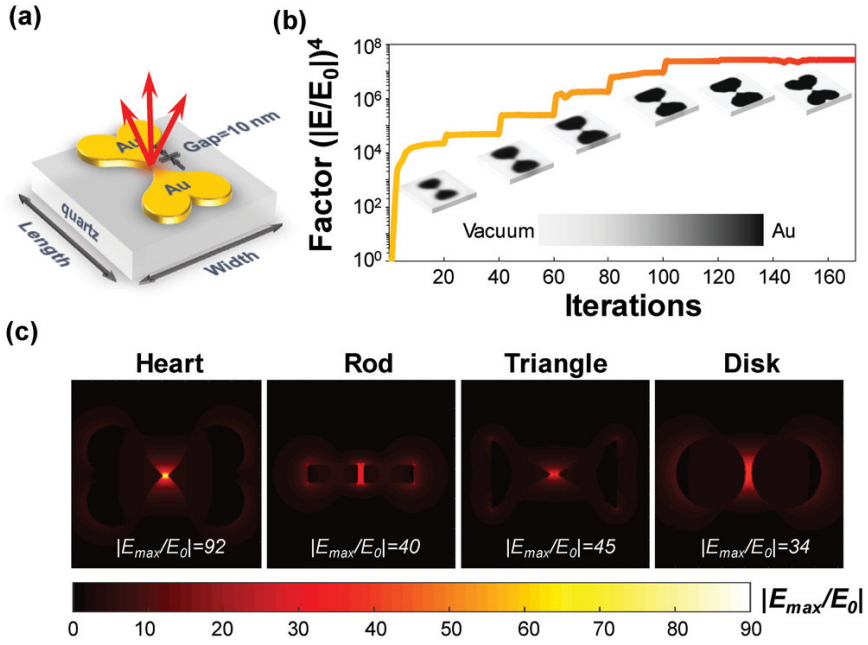

Figure 1.2 *: Taken from [15]. Summary of inverse design motivated by the electric field enhancement feature. a) The gold nanoparticle dimer's 3D model, which has certain material and geometric properties predetermined. b) The electric field enhancement factor in the nanodimer gap in function of optimization algorithm iterations. c) The electric field enhancement distribution of heart-, rod-, triangle-, and disk-shaped nanoparticle dimers at an XY plane.*

Moreover, Thorsten Feichtner et al. [16] proposed another type of inverse-designed plasmonic nano-antenna (Figure 1.3a) based on topology optimization which exhibits strong light localization and enhancement (Figure1.3d).

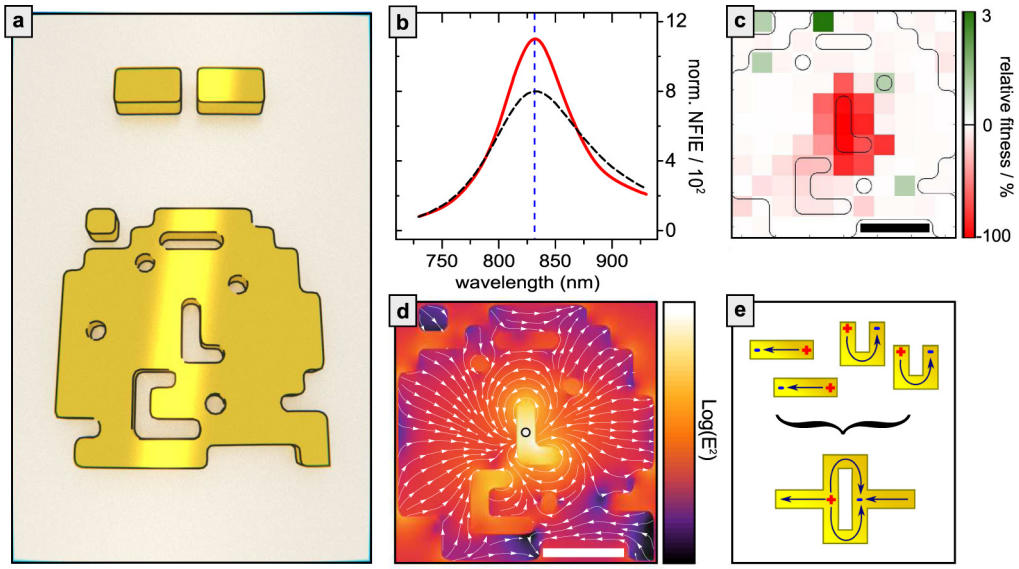

Figure 1.3 *: Taken from [16]. Properties of the evolutionary algorithm optimized nano-antenna: a) A 3D schematic of the dipolar nano-antenna (top) and the optimized one based on topology optimization (bottom) on substrate. b) Near field intensity enhancement (NFIE) spectrum at the very center of the dipolar nano-antenna shown in the top of a) (black dashed) and the optimized one shown in the bottom of a) (red). The optimization wavelength is marked blue. c) Toggle plot of the optimized nano-antenna. d) Electric field intensity enhancement and current direction (white arrows) in the center XY plane of the optimized nano-antenna. e) Model for the operation principle of the optimized nano-antenna combining current patterns from two U-shape resonators and two nanorod. All scale bars are 100 nm.*

In addition, plasmonic nano-antennas are also often used for manipulating polarization state of light [17-20]. Therefore, based on these characteristics of plasmonic nano-antennas and the formula of the inverse Faraday effect, plasmonic nano-antennas are quite suitable to create the strong inverse Faraday effect and manipulate it the way we want.

1.5 The inverse Faraday effect in plasmonic nano-antennas

Recently, several theoretical and experimental papers have already demonstrated that the enhancement of optical electric fields and field gradients by resonant plasmonic nano-antennas allowed to generate, through the inverse Faraday effect, strong stationary magnetic fields $\boldsymbol{B}$ (as opposed to the optical magnetic field $\boldsymbol{H}$ in this manuscript) [21-25].

In particular, Matthew Sheldon and his group reported experimental quantification of optically induced magnetization in plasmonic gold nanoparticles due to the inverse Faraday effect in 2020 [22]. The study reveals that the induced magnetic moment due to the inverse

Faraday effect is significant under ultrafast pulse excitation. The mechanism involves the coherent transfer of angular momentum from the optical field to the electron gas, leading to all-optical subwavelength strategies for optical isolation without the need for external magnetic fields. The research findings highlight the potential of plasmonic nanomaterials in terms of induced magnetic field strength, spatial confinement, and ultrafast time response. To be specific, the inverse Faraday effect, which is an optomagnetic phenomenon, can induce a magnetization whose direction depends on the helicity of incoming light. In their study, the magnetization can be described by

$$\boldsymbol{M}_{ind} = \frac{\lambda \upsilon}{2\pi c}\left(I_{RCP} - I_{LCP}\right)$$

where λ is the wavelength of light in vacuum, υ is the Verdet constant, c is the speed of light and $I_{RCP}\left(I_{LCP}\right)$ is the incident intensity of right (left) circularly polarized light. Moreover, Faraday rotation at origin of the Faraday effect which is thought to the reciprocal consequence of the inverse Faraday effect can be described as follows with the same Verdet constant:

$$\Delta\theta = \upsilon \boldsymbol{B}_{app} L$$

where $\Delta\theta$ is the Faraday rotation angle, $\boldsymbol{B}_{app}$ is the applied magnetic field and L is the effective travel distance of light inside the medium.

Based on those mentioned above, to measure the induced magnetization generated by the inverse Faraday effect in plasmonic gold nanoparticles, they performed ultrafast pump–probe Faraday rotation measurements on 100-nm-diameter gold nanoparticle colloids. Firstly, the spectrally resolved Verdet constant was determined from static Faraday rotation measurements on the sample colloid solution in a cuvette with 1 cm path length (Figure 1.4a). On the same sample in a flowing cell with 2mm path length (Figure 1.4b), the inverse Faraday effect was induced by a circularly polarized pump beam (green line in the Figure 1.4b). The induced magnetization due to the inverse Faraday effect was expressed by the Faraday rotation angle ($\Delta\theta$) of a linearly polarized probe beam (purple line in the Figure 1.4b). Based on the previously measured Verdet constant, therefore the magnitude of the optical rotation of the probe enabled quantitative determination of the strength of the induced magnetization due to the inverse Faraday effect in the plasmonic gold nanoparticle colloids. More details can be found in the reference [22].

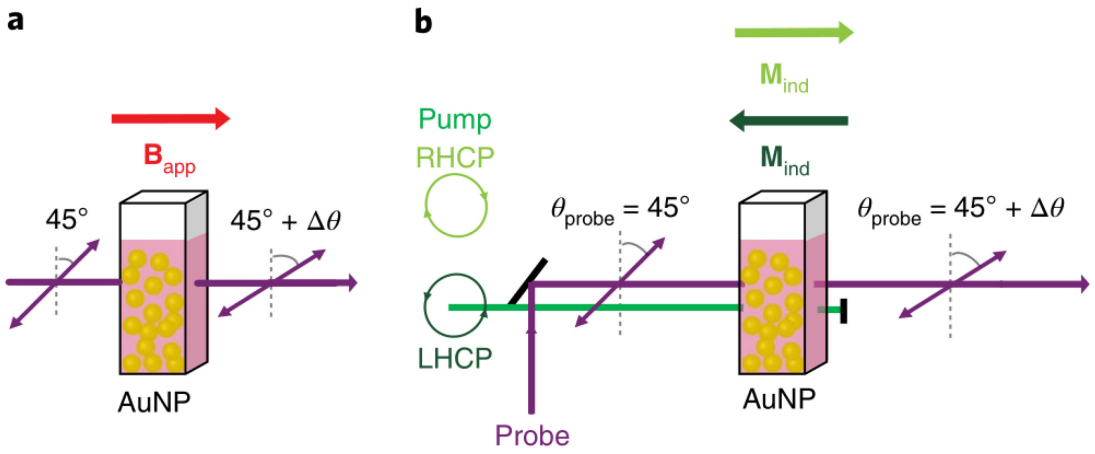

Figure 1.4 *: Taken from [22]. A 3D schematic of the Faraday effect and the inverse Faraday effect in gold nanoparticle colloids. a) The rotation of the light's polarization plane when it passes through a magnetized medium is known as the Faraday effect. b) The inverse Faraday effect induces a magnetization of a medium,* $\boldsymbol{M}_{ind}$*, during a circularly polarized light excitation (green line). The direction of induced magnetization depends on the helicity of the incoming light. The optical rotation angle of a probe beam (purple line) indicates* $\boldsymbol{M}_{ind}$ *value.* $\boldsymbol{B}_{app}$ *represents the external applied static magnetic field; Δθ refers to the Faraday rotation angle; R(L)CP denotes the right(left) circularly polarized light.*

In this manuscript, different inversely designed plasmonic nano-antennas made of gold with substrate of glass will be used to manipulate the inverse Faraday effect providing a brand-new perspective on the light-matter interactions at the nanoscale with various important applications in magnetic domain such as ultrafast data storage, ultrafast data processing and so on, which may be as the foundation components for the quantum computer in the future.

1.6 Conclusion

In summary, plasmonic nano-antennas play a crucial role in manipulating light at the nanoscale, enabling various applications in nanophotonics and nanoplasmonics. Therefore, they are extremely suitable for generating the inverse Faraday effect and manipulating it on demand because of their ability to strongly enhance the optical electromagnetic fields, create strong field gradients and manipulate the polarization state of light in the near field. In addition, experimental results in 2020 about quantification of optically induced magnetization in plasmonic gold nanoparticles due to the inverse Faraday effect strongly confirm this hypothesis and exhibit strong feasibility as well.

In my Ph.D. projects, different plasmonic nano-antennas with glass substrate, inversely designed by metaheuristic algorithms based on topology optimization, are deeply investigated to generate, and manipulate the inverse Faraday effect.

Chapter 2 The origin of the inverse Faraday effect in metals

2.1 Introduction

In the chapter 1, we have briefly introduced the inverse Faraday effect in general and plasmonic nano-antennas as well. Since we want to manipulate the inverse Faraday effect by using the plasmonic nanostructures, the theory of the inverse Faraday effect in metals should be then discussed to better understand this magnetization process. In this chapter, we will firstly discuss about the theory using the drift currents terminology to describe the origin of the inverse Faraday effect based on the work of R. Hertel. After that, according to the Biot-Savart law, the stationary magnetic field induced by these drift currents can be estimated. Finally, the state-of-the art about manipulating the inverse Faraday effect in plasmonic nanostructures are also discussed.

2.2 Theory

In metals, the inverse Faraday effect has been described as the result of the metal's free conduction electrons set in motion by non-linear forces from the incident light. As described by R. Hertel who is now a CNRS researcher at Strasbourg in France, by considering the free electrons of a metal as a collisionless plasma, the theories of plasma physics can be applied to metals, allowing precise descriptions of the creation and the behavior of drift currents. By their nature, these drift currents are independent of time and always flow in the same direction, a direction defined by the polarization of incoming light. They can, therefore, be considered, to a certain extent, as direct currents, allowing the generation of stationary magnetic fields. In addition, as demonstrated by R. Hertel et al. in two successive scientific papers, these drift currents can have two characteristics, one microscopic and relying on optical electric fields [7], and the other macroscopic, resulting from the gradients of optical electric fields [26].

In this manuscript, we propose here a simplified description of this theory [7], whose formalism allows an implementation of common FDTD simulation techniques available to the nano-optics community, in order to optimize plasmonic nano-antennas to manipulate the inverse Faraday effect at the nanoscale.

2.3 Drift currents

It is well known that light can apply nonlinear forces on moving free charges and in particular electrons [27]. A relevant example is the ponderomotive force [28] used to accelerate charges in plasma for instance [29]. As the time average value of these forces are nonzero, they are at the origin of optically induced drift currents. A way to account for these drift currents is to start from the general equation of a current generated in a metal by an electromagnetic wave $\boldsymbol{J}_\omega = e \cdot n \cdot \boldsymbol{v}$, where $\boldsymbol{J}_\omega$ is the conductive current, e is the charge of the electron (with e < 0), n is the density of free electrons in the metal, and v is the velocity. When the free electrons are exposed to an electromagnetic wave, their density can then be written $n = \langle n \rangle + \delta_n$, where $\langle n \rangle$ is the electron density at rest and δ_n is the oscillating part of n at the angular frequency of the incoming light ω. The current then becomes $\boldsymbol{J}_\omega = e \cdot \langle n \rangle \cdot \boldsymbol{v} + e \cdot \delta_n \cdot \boldsymbol{v}$, where $e \cdot \delta_n \cdot \boldsymbol{v}$ can be seen as a perturbation of $e \cdot \langle n \rangle \cdot \boldsymbol{v}$. The time average drift current $\boldsymbol{J}_d$ then corresponds to the nonzero part of the time average $\langle \boldsymbol{J}_\omega \rangle$. (i.e., $\boldsymbol{J}_d = e \cdot \langle \delta_n \cdot \boldsymbol{v} \rangle$) Hence, by identifying δ_n and $\boldsymbol{v}$, it is possible to calculate the drift currents and their associated stationary magnetic fields.

The expression for δ_n can be extracted from the continuity equation:

$$\frac{\nabla \cdot \boldsymbol{J}_\omega}{e} + \frac{\partial n}{\partial t} = 0 \tag{1}$$

which can be integrated and rewritten as [7]

$$n = \langle n \rangle - \frac{1}{e} \frac{\nabla \cdot \boldsymbol{J}_\omega}{i\omega} = \langle n \rangle + \delta_n \tag{2}$$

The oscillating part of *n* is then

$$\delta_n = -\frac{1}{e} \frac{\nabla \cdot \boldsymbol{J}_\omega}{i\omega} \tag{3}$$

The expression of ***v***, meanwhile, can be obtained directly from the expression of the conduction current which in first approximation is written $\boldsymbol{J}_\omega = e \cdot \langle n \rangle \cdot \boldsymbol{v}$, assuming that $\langle n \rangle \gg \delta_n$ [7].

Hence, the velocity is

$$\boldsymbol{v} = \frac{\boldsymbol{J}_\omega}{e\langle n \rangle} \tag{4}$$

The drift currents in a metal subjected to an electromagnetic wave is then written:

$$\boldsymbol{J}_d = \frac{1}{2e\langle n \rangle} \mathrm{Re}\left(\left(-\frac{\nabla \cdot \boldsymbol{J}_\omega}{i\omega} \right) \cdot \boldsymbol{J}_\omega^* \right) \tag{5}$$

with $\boldsymbol{J}_\omega = \sigma_\omega \boldsymbol{E}$, where $\boldsymbol{E}$ is the optical electric field and σ_ω is the dynamic conductivity of the metal that can be readily obtained from phenomenological values, $\sigma_\omega = i\omega\varepsilon_0 (\varepsilon - 1)$, where ε_0 is the dielectric permittivity of vacuum and ε is that of the metal.

2.4 Stationary magnetic fields

Hence, according to the Biot–Savart law shown in Equation (6), we can deduce the stationary magnetic fields generated by these drift currents, induced by light.

$$\boldsymbol{B}(r) = \frac{\mu_0}{4\pi} \iiint_v \frac{\boldsymbol{J}_d \times \boldsymbol{r'}}{|\boldsymbol{r'}|^3} dV \tag{6}$$

where μ_0 is the vacuum magnetic permeability, dV is the volume element and $\boldsymbol{r'}$ is the vector from dV to the observation point.

Moreover, we can notice here that the drift current $\boldsymbol{J}_d$ is quadratic regarding the electric field, and therefore, $\boldsymbol{J}_d$ and $\boldsymbol{B}$ will be linear in terms of optical power of incident light. Also, it is known that under high excitation power, the properties of metals can change, due to the creation of hot electrons [30, 31]. For simplicity, these effects are not considered in this manuscript; a way to include them would be to determine the dielectric permittivity ε of the metal under the influence of these high optical powers of incident wave.

2.5 The state of the art

Recently, in plasmonic nano-antenna community, using Finite-Difference Time-Domain (FDTD) simulations, physicists have already theoretically predicted the inverse Faraday effect generated by plasmonic antennas at the nanoscale. For example, Matthew T. Sheldon and his group reported in 2017 that spherical Au nanoparticles can generate drift

currents and static magnetic fields which can exceed 1 mT under 10^{15} W/m^2 optical intensity [24].

After that, Mathieu Mivelle and his group theoretically predicted in 2021 that a plasmonic nano-antenna called bull-eye nanostructure containing 10 concentric metallic rings, optimized by genetic algorithm, can generate a strong stationary magnetic pulse of the order of the Tesla at the nanoscale and for only a few femtoseconds, something that no other technique allows nowadays [32]. Specifically, following Equation 5 and Equation 6 mentioned before and using FDTD simulations, they have genetically optimized the design of a realistic gold photonic nanoantenna (Figure 2.1) to generate a strong ***B***-field confined to the center of the gold nanostructure (Figure 2.3). The nano-antenna consists of a bull-eye-shaped nanostructure composed of 10 concentric grooves made in a 40 nm gold layer placed on a glass substrate. They chose the smallest width of the grooves to be 6 nm, while the largest should be smaller than 30 nm. Likewise, the width of the metallic rings had to be chosen between 20 nm and 50 nm. They carefully selected these parameters to design a nanoantenna that, for instance, a helium focused ion beam (He-FIB) could fabricate in a cleanroom facility, both for reasons of etch resolution and processing time. A plane wave light pulse with a full width at half-maximum power temporal duration of 5.3 fs sent from the bottom of the nanostructure (Figure 2.1) and with a power density of 10^{12} W/cm^2 excites the antenna. This fluence was chosen because of the resistance of the thin gold layer to these peak powers at those time scales. Nevertheless, it is possible to use even higher powers by inserting the gold nanostructure in a matrix resistant to high energies such as sapphire or glass. This technique could potentially create extremely intense stationary magnetic fields, with the disadvantage of confining it inside the material. They chose the wavelength to be 800 nm and the polarization to be circular. This polarization state is known to generate a strong inverse Faraday effect. Within these constraints, the genetic algorithm was allowed to modify the diameters and sizes of the grooves independently of each other. Finally, an inversely designed optimal plasmonic nano-antenna is obtained which can generate a strong ***B***-field confined to the center under a circular polarization of excitation due to the inverse Faraday effect.

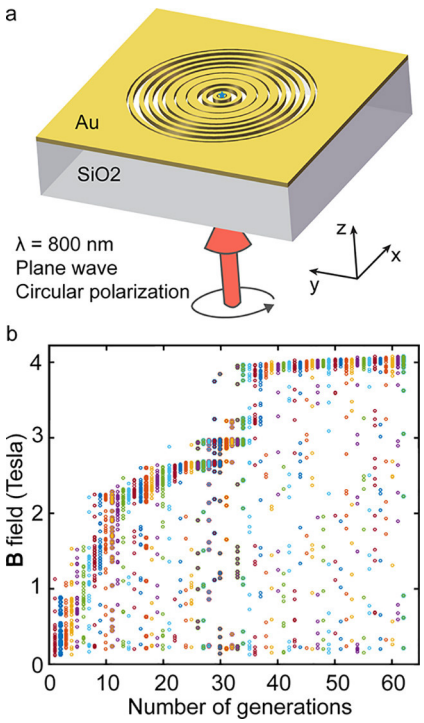

Figure 2.1 *: (a) Schematic of the photonic nanoantenna. The antenna consists of a bull-eye structure made of 10 grooves in a 40 nm gold layer deposited on a glass substrate. The excitation is made by a plane wave light pulse (5.3 fs) launched from the bottom of the structure. The wavelength is 800 nm, and the polarization is circular and right-handed. (b) Amplitude of the magnetic field in the center of the photonic structures during the selection process. Each star corresponds to a single simulation, and each generation contains 40 structures.*

This intense stationary magnetic field, confined at the nanoscale and for a few femtoseconds, results from annular optical confinement and not from the creation of a single optical hot spot (Figure 2.2).

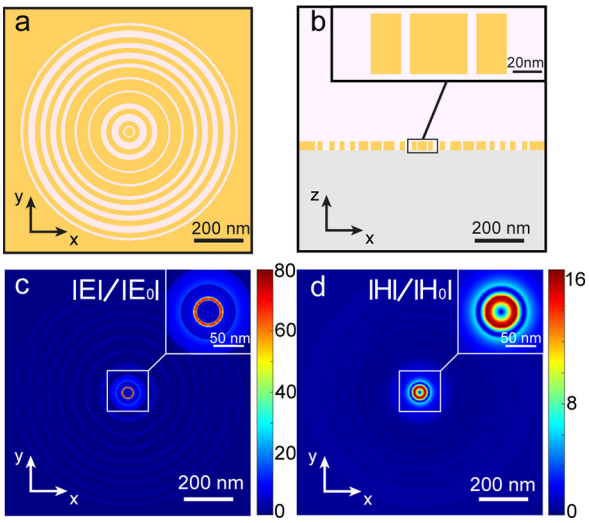

Figure 2.2 *: The optimized nanoantenna geometry in (a) an (xy) plane and (b) an (xz) plane. Amplitude distribution in the middle of the antenna in an (xy) plane of (c) the electric* ***E*** *and (d) the magnetic* ***H*** *optical fields, normalized by respectively the electric* $\boldsymbol{E_0}$ *and magnetic* $\boldsymbol{H_0}$ *optical fields without the photonic antenna.*

Moreover, by controlling the incident circular polarization state, they demonstrated that the orientation control of the created stationary magnetic field and its reversal on demand (Figure 2.3). This result is significant since it demonstrates the tunability of the magnetic field orientation as a function of the excitation polarization and thus its application possibilities.

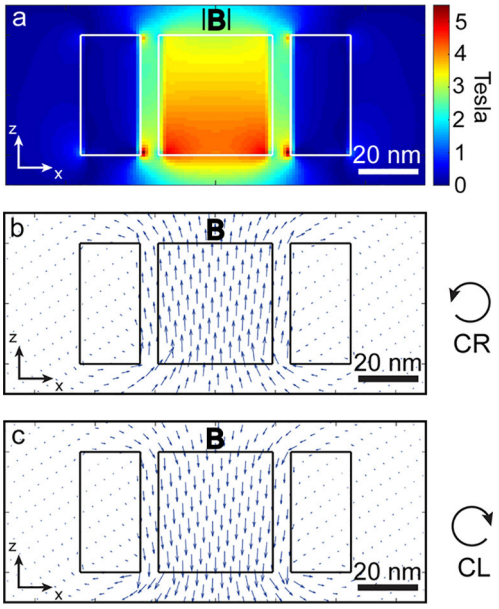

Figure 2.3 *:* ***B****-field distribution. (a) Distribution of the amplitude of* ***B****-field generated at the center of the optimized nanostructure (the metal boundaries are indicated by white rectangles). (b) and (c)* ***B****-field vectorial lines for the same area than (a) and for (b) a right-handed and (c)*

left-handed circular polarization state of incoming light. The black rectangles highlight the metal boundaries, the black arrows indicate the polarization states of incoming light.

What's more, the stationary magnetic field's temporal behavior and the drift currents associated with it reveal the sub-cycle nature of this light–matter interaction at the nanoscale (Figure 2.4).

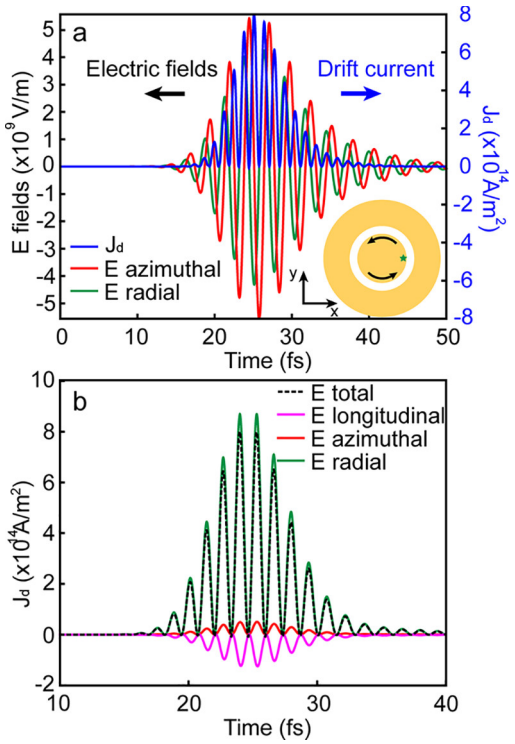

Figure 2.4 *: Temporal response of drift currents. (a) Temporal evolution of the drift currents (blue curve), superimposed on the temporal evolution of the radially (green curve) and azimuthally (red curve) polarized electric fields, inside the metal core of the plasmonic nanoantenna, symbolized by the green star in the inset drawing. (b) Contribution of the different components, longitudinal (along z), azimuthal and radial, of the electric optical field in generating drift currents.*

Overall, the manipulation of drift currents by a plasmonic nano-antenna for the generation of stationary magnetic field pulses finds applications in the ultrafast control of magnetic domains with applications in ultrafast data storage technologies.

Since the inverse Faraday effect's discovery in the 60s, it was believed that only circular polarizations could magnetize matter by this magneto-optical phenomenon. However, Xingyu Yang et al. from Mathieu Mivelle's group demonstrated in 2023 that a gold nanorod excited by

a linear polarization state of light generates non-zero stationary magnetic fields by the inverse Faraday effect when the incident polarization state of the light is not parallel to the long axis of the rod [33]. This new physical concept results from the local manipulation of light by a plasmonic nano-antenna. To be specific, a gold nanorod of length L = 120 nm, thickness T = 40 nm, width W = 20 nm, and placed on a glass substrate is excited by a linearly polarized plane wave of intensity 10^{12} W/cm^2, wavelength 800 nm, and propagating along the positive z-axis (Figure 2.5a and e). Two linear polarizations state of incoming light are studied in Figure 2.5. As can be seen remarkably, the current distribution for a 45° polarization generates a uniform magnetic field at the center of the nanorod (Figure 2.5h), demonstrating for the first time that an inverse Faraday effect is possible using a linear polarization of the light, which was previously thought to be impossible.

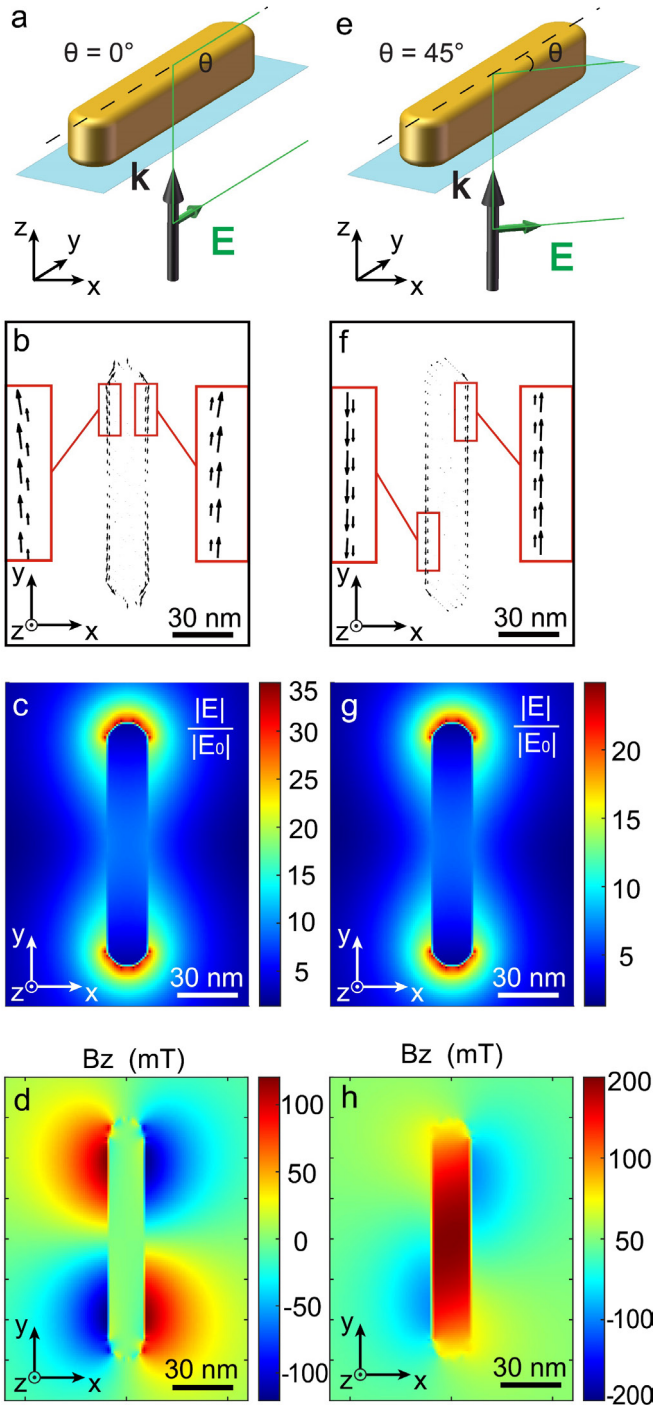

Figure 2.5 *: The inverse Faraday effect in a gold nanorod under linear polarization. Generation of drift currents and stationary magnetic fields in a gold nanorod excited by linear polarization (a)–(d) along the antenna long axes (θ = 0°) and (e)–(h) at 45° from the x-axis. (a) and (e) Schematic representation of the gold nanorod excited by linear polarization at θ = 0° and 45° from the antenna long axes, respectively, at the wavelength of 800 nm and for an intensity of 10^{12} W/cm^2. For the two excitation conditions shown in (a) and (e), the normalized electric field distributions (b) and (f), associated drift currents (c) and (g), and generated stationary magnetic fields (d) and (h) are shown, respectively.*

In addition, multiple linear polarizations with different polarization angles with respect to the long axis of a gold nanorod are theoretically studied using FDTD simulations. It's observed that the stationary magnetic field produced is reversible on demand simply by changing the polarization angle with respect to the long axis of the nanorod (Figure 2.6). This type of behavior would be extremely useful in the all-magnetic ultrafast manipulation of magnetic domains since two opposite magnetic field orientations are achievable for the same power density and heat generation in the structure which we will discuss more in the chapter 6. Moreover, the magnetic field intensity generated by the structure is up to 25 times higher than a gold nanoparticle excited by a circular polarization of the same power and frequency.

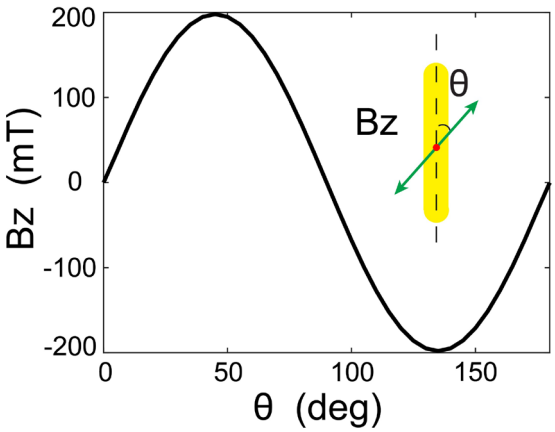

Figure 2.6 *: Stationary magnetic field along z generated by a linear inverse Faraday effect at the center of the plasmonic antenna as a function of the incident polarization angle* θ.

2.6 Conclusion

In this chapter, the origin of the inverse Faraday effect in plasmonic nanostructures is explained and described by using the simplified description of drift current theory originally proposed by R. Hertel in 2006. Moreover, the stationary magnetic fields induced by these drift currents can be then easily estimated using the Biot-Savart law (Equation 6). Furthermore, a bull-eye shape nano-antenna, which contains ten concentrical gold rings, is inversely optimized by the genetic algorithm in order to generate strong and ultrafast stationary magnetic field pulses confined at the center of the nanostructure under a circular polarization of excitation. Furthermore, the direction of the stationary magnetic field generated by the bull-eye nanostructure is reversible on demand simply by changing the circular polarization state of incident light. In addition, it was also theoretically demonstrated for the first time that stationary magnetic fields could be generated through a gold nanorod under a linear polarization of

excitation with polarization angle not parallel to the long axis of the nanorod due to the linear inverse Faraday effect. These studies demonstrate the advantages of optical nanostructures for generating high IFE, at the nanoscale and potentially at very fast timescales. In addition, the research on the use of linear polarization state of light to generate the IFE also demonstrates the advantages of plasmonic nanostructures for manipulating light polarization at the nanoscale, opening up extremely interesting prospects for further manipulating the magneto-optical IFE process, as I will demonstrate in the following chapters of this manuscript.

Chapter 3 Inverse design for plasmonic nano-antennas

3.1 Introduction

With the purpose of manipulating the inverse Faraday effect, the design of plasmonic nano-antennas is a crucial step to achieve that purpose. Considering the non-intuitive characteristics of plasmonic nanostructures for manipulating the inverse Faraday effect, the inverse design compared to the traditional forward design has naturally come to our mind. In this chapter, we will firstly introduce the physical theory behind the optical simulation, i.e., the Finite-Difference Time-Domain (FDTD) method which is the fundamental component of inverse design process. Then, the commercial FDTD software i.e., Lumerical FDTD and the basic plasmonic nanostructure that I used for my Ph.D. projects are discussed. Finally, the whole inverse design process including topology optimization, objective function and metaheuristic algorithm is described as well.

3.2 Numerical simulations

3.2.1 Introduction of Finite-Difference Time-Domain (FDTD)

The Finite-Difference Time-Domain (FDTD) or Yee's method is a numerical method commonly used in the field of electromagnetic simulations [34] especially for optics simulation ranging from visible wavelength to Near-IR up to Mid-IR. The FDTD approach is a part of the broad category of grid-based finite difference modeling techniques. The FDTD method solves the Maxwell’s equations on a discrete spatial and temporal grid. Each field component is solved at a slightly different location within the grid cell (Yee cell), as shown below in Figure 3.1.

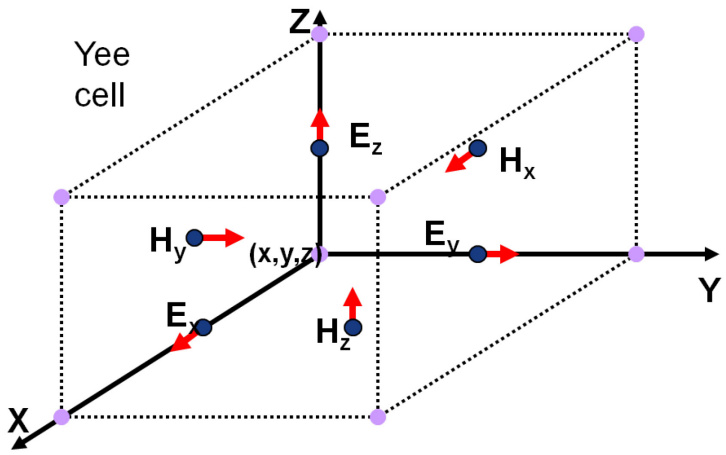

Figure 3.1 *: Taken from [35]. Yee cell which represents the discretization of space in the numerical model and the distribution of the electromagnetic field in this cell.*

Central-difference approximations to the space and time partial derivatives are used to discretize the time-dependent Maxwell's equations in partial differential form. Due to its time-domain nature, FDTD method can cover a wide frequency range with a single simulation run. The method is well explained in the references [36-38]. In this manuscript, the FDTD method won't be described in detail.

The accuracy of FDTD simulations' result is directly related to the mesh size, FDTD simulation window, boundary condition as well as the external excitations. In my Ph.D. project, all simulations are conducted by the commercial software Lumerical FDTD provided by the ANSYS, Inc.

3.2.2 Lumerical FDTD by Ansys, Inc.

In the following sections, basic components of the commercial software Lumerical FDTD and the basic structure of plasmonic nano-antenna that I used for my Ph.D. projects will be described and explained.

3.2.3 Simulation window

The simulation window is a basic component of the software to define a region where the FDTD simulation is performed. All other components geometry size should be within this region otherwise they won't be considered. The simulation window can be 3D or 2D according to the demand of projects. After adding the simulation window in the software with certain

geometry size, the simulation time, the simulation temperature, and background index can be configured. Moreover, general mesh size can be set to define the cell inside this window and the mesh size can be override by adding additional mesh size components which will be explained in the mesh size section.

In addition, the boundary conditions for each layer in X, Y and Z can be chosen from Perfectly Matched Layer (PML), Periodic, Perfect Magnetic Conductor (PMC) and so on. To be specific, in my Ph.D. projects, the dimensions of the 3D computational window for the simulations were 750*750*900 nm^3 (Figure 3.2). The simulation time is fixed to be 1000 fs and the simulation temperature is fixed to be 300 K.

3.2.4 Perfectly Matched Layer (PML) boundary condition

A perfectly matched layer (PML) is an artificial absorbing layer for wave equations, commonly used to truncate computational regions in numerical methods to simulate problems with open boundaries, especially in the FDTD methods [39, 40]. The primary characteristic of a PML that sets it apart from a regular absorbing material is its ability to strongly absorb outgoing waves from the interior of a computational region without reflecting them back into the interior. This property is achieved by designing the PML such that waves incident upon it from a non-PML medium do not reflect at the interface. Thus, it can avoid all unwanted reflections during the simulation creating a plane wave which is exactly what we need for my Ph.D. projects. The whole schematic of FDTD simulations for my Ph.D. project is shown in the following Figure 3.2.

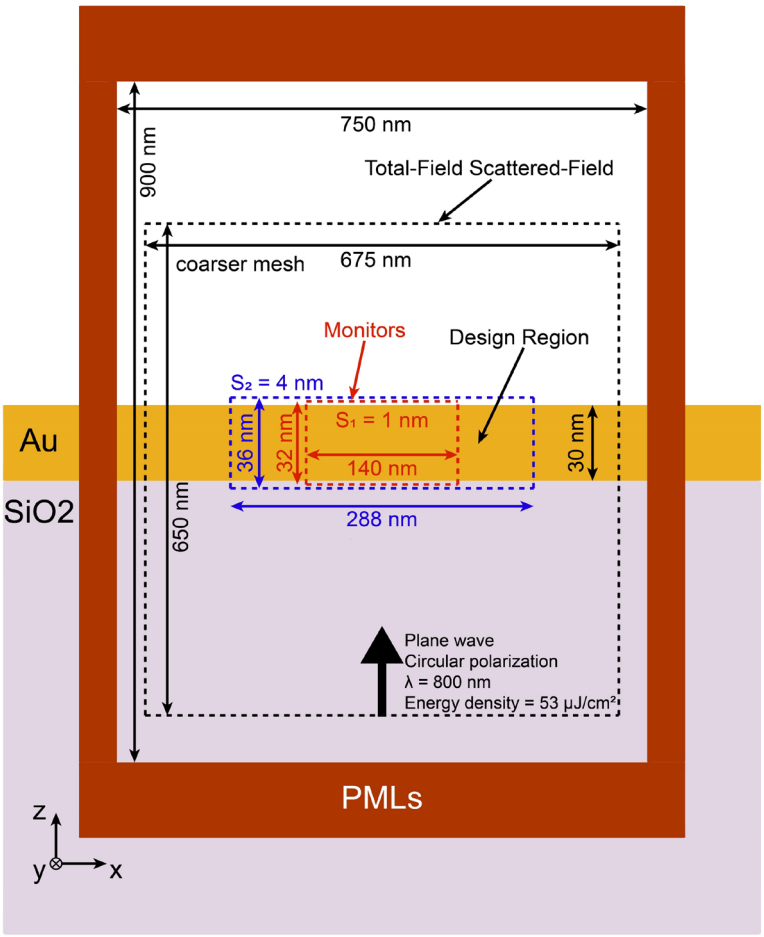

Figure 3.2 *: Schematic diagram of FDTD simulation at a XZ plane for a nanostructure under a circular polarization of excitation with PML boundary conditions.*

3.2.5 Mesh size

After choosing the general mesh setting in the FDTD simulation window, finer mesh could be defined by adding the mesh size component to override the defined mesh by the FDTD simulation window before. In addition, according to the official tutorial of Lumerical FDTD provided by the ANSYS company, there are two key challenges associated with solving Maxwell's equations on a finite mesh [41]:

1. There are numerical errors associated with the finite mesh size, even in homogenous material. For example, the speed of light on a finite mesh is not the same as real space, but depends on dx, dy, dz and dt. Lumerical's graded meshing with automatic mesh generation solves this problem by adjusting the mesh to the refractive index of the materials. For example, the mesh in a material of n=2 will be twice as small as in a material with n=1, because the

wavelength is smaller in the higher index material. This ensures that the numerical errors associated with the finite mesh are kept below a certain threshold in all regions of the simulation.

2. It is not possible to resolve interfaces to higher precision than the size of the mesh used. One solution is to use mesh override regions to force a very small spatial mesh near interfaces. The disadvantage of this method is that it can greatly increase simulation times and memory requirements. In the FDTD method, the simulation time scales as 1/(dx^4) for 3D simulations. A better solution for many applications is to use conformal mesh technology. In some cases, a combination of both solutions is required.

In general, we recommend using conformal meshing as much as possible, and sometimes mesh override regions to force a smaller mesh size in critical regions. Specifically, for my Ph.D. projects, several meshes are used for the discretization of the computational space, a coarser non-uniform mesh of 4 to 16 nm for the external unstructured parts, of the simulation, a finer mesh of 4 nm for a central nanostructured part of 288*288*36 nm^3 in X, Y, and Z, respectively containing the nanostructures, and an even finer mesh of 1 nm for the part where the drift currents and magnetic field are calculated of 140*140*32 nm^3 in X, Y, and Z (Figure 3.2).

3.2.6 External excitation

The external source that we used for the projects is Total-Field Scattered-Field (TFSF) source. According to the official tutorial of the software Lumerical FDTD, the TFSF source is an advanced version of the plane-wave source designed primarily for particle scattering simulations, where the particle may be in a homogeneous medium or on a multi-layer substrate.

The TFSF source is used to inject a finite span plane wave into a computational region whose primary purpose is to separate the incident and scattered fields. There are both incident and scattered fields inside the source region that we defined and there are only scattered fields outside the source. Moreover, in this manuscript, the range for the TFSF in X, Y and Z were 675*675*650 nm^3 (Figure 3.2). In addition, in order to generate circularly polarized light excitation, two TFSF source at the same position with same geometrical range but with 90 degrees phase difference and polarization angle difference were used. More specifically, in the coordinates of the simulation used for the Ph.D. project, for one TFSF source, the polarization

angle and phase are fixed to be 0. For the other TFSF at the same position with same range, the polarization angle is fixed to be 90 and the phase can be either 90 for a Right Circular Polarization (RCP) or -90 for a Left Circular Polarization (LCP).

3.2.7 Monitor

The monitor in the Lumerical FDTD software is a data collector which can return electric field distributions, magnetic field distributions, power density distributions and refractive index distributions in the spatial range we chose. According to the demand and configuration, it can return 3D distributions, 2D distributions or even data values only for one specific point.

There are multiple types of monitors which are provided directly by the software, such as “Refractive index”, “Field time”, “Movie”, “Frequency-domain field and power” and so on. In my Ph.D. projects, two different types of monitors are used for collecting data during simulations. One is the “Frequency-domain field and power” monitor to collect optical electric field $\boldsymbol{E}$ at the near field; The other is “Refractive index” monitor to collect refractive index distribution of the whole nanostructure for the calculation of dynamic conductivity of the metal in order to get the conductive currents.

3.2.8 Material database

The material database allows you to manage (create, modify, delete) the materials that are available for use in your simulations. The Material Database also allows for the definition of complex materials using experimental data or parametrized models. The Material Database stores the material data to be used in the simulation. It also provides an interface to change material properties like color, mesh order, and model parameters. Experimental data can also be loaded into the database [42].

The optical material database includes refractive index data for several common materials such as metals like gold, copper and so on. In my Ph.D. project, there are three main materials in total which were used for simulations. The first one is gold which is used for the plasmonic nano-antennas. The textbook values of Johnson and Christy provided by the software were used for the gold properties in the simulations. The second one is the silicon dioxide (glass) used as the substrate of plasmonic nano-antennas. The optical constants for that material in the software comes from the “Handbook of Optical Constants of Solids” edited by Edward

D. Palik. The last one is vacuum with refractive index of 1. In addition, the refractive index for background material of simulation is fixed to be 1 as well.

3.2.9 Basic structure

In my Ph.D. project, the structure of plasmonic nano-antennas is realized in a 30 nm thick gold layer deposited on a glass substrate. The excitation is made by a TFSF plane wave light pulse launched from the bottom of the nanostructure with centered wavelength of 800 nm. The basic schematic of the plasmonic nano-antenna is shown in Figure 3.3. The design region range in X, Y and Z is 280*280*30 nm^3 where topology optimization will be applied to inversely design different shapes to satisfy different optimization objectives. The dimensions shown here are all carefully chosen making the nanostructure be feasibly fabricated using nanofabrication techniques in the clean room such as e-beam lithography, focused ion beam, helium ion beam and so on.

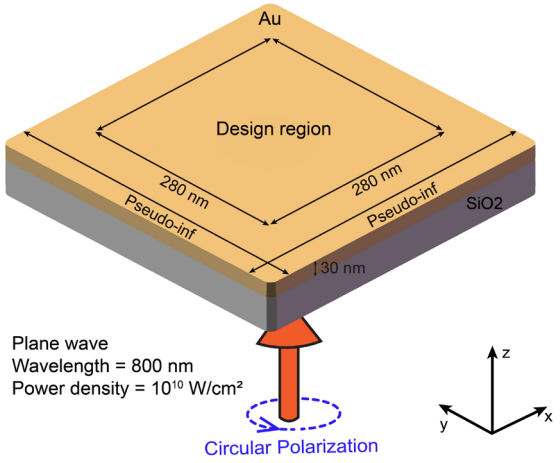

Figure 3.3 *: The schematic of a plasmonic nano-antenna realized in a 30 nm thick gold layer deposited on a glass substrate.*

3.2.10 Conclusion

In this section, the FDTD method and the Lumerical FDTD software from ANSYS, Inc are both discussed. Moreover, the basic components of the software are described as well. In addition, the basic structure of the plasmonic nano-antenna for my Ph.D. projects is also illustrated in the Figure 3.3.

3.3 Optimization

3.3.1 Topology optimization

3.3.1.1 Introduction

Topology Optimization (TO) is a mathematical method which spatially optimizes the distribution of material within a defined design region, by meeting given constraints previously established and minimizing a predefined objective function [43]. Recently, the plasmonic nano-antennas' community pays more and more attention to the topology optimization for non-intuitive nanostructure design, which has been already applied extensively in many other domains such as mechanical structures [44] or other physical systems [45]. The topology optimization is defined by the allocation of material either existing or not at specific points in a defined design region, to satisfy a certain objective function. This means that each grid point is a design parameter, leading to the geometry being optimized in a pixel-like fashion [46].

In my Ph.D. projects, the non-intuitive plasmonic nano-antennas are urgently needed to meet some specific objective function to obtain some specific physical phenomena concerning the inverse Faraday effect at the nanoscale as we expected. Based on that, the topology optimization solved by metaheuristic algorithm is then introduced in the following sections.

3.3.1.2 Design region and parameters

To start with, the topology optimization is applied to a predefined design region shown in Figure 3.3 with range of 280*280*30 nm^3 in X, Y and Z, respectively. The unitary element that we used is a vacuum nanocylinder with thickness of 30 nm and diameter of 28 nm. Based on that, a 10-by-10 binary matrix containing 100 binary parameters in total can be used to represent a structure.

Here, more precisely, 1 represents that there is an allocation of material. Conversely, 0 represents there is a vacuum nanocylinder indicating no material there. Therefore, different structure has different 10-by-10 binary matrix to represent itself meaning that the shape of structure can be mathematically defined through the 10-by-10 binary matrix. The purpose of project is then to find a 10-by-10 binary matrix to satisfy the predefined objective function at most. Under this condition, some optimization algorithms could be used to help us find the

optimal 10-by-10 matrix, such as metaheuristic algorithms like Genetic Algorithm (GA) which will be discussed in the section 3.3.3.

3.3.1.3 Topological process

For each 10-by-10 binary matrix representing one shape of the plasmonic nano-antenna, a vacuum nanocylinder will be at the position if the element of matrix at that position is 0 otherwise there is an allocation of material. Moreover, once the distribution of material is determined by the 10-by-10 binary matrix, the obtained structure then will be smoothed to avoid all the roughnesses not experimentally realistic and generating non-physical effects. The Figure 3.4 shows the whole topological process for one certain nanostructure.

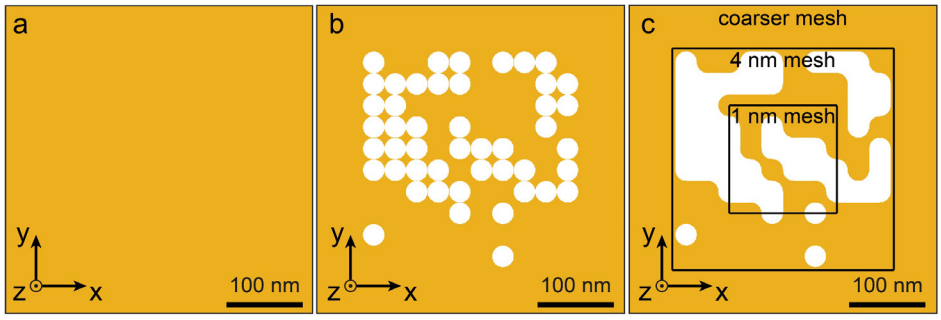

Figure 3.4 *: Construction of the elements from a 10-by-10 binary matrix. a) Starting from a 30 nm thick uniform layer of gold. b) Nanocylinder vacuum holes are made according to a 10-by-10 binary matrix where 0 representing there is a vacuum nanocylinder and 1 representing there is a material. c) The obtained structure is then smoothed to avoid all the roughnesses not experimentally realistic and generating non-physical effects. In addition, the different mesh areas are also shown in c.*

3.3.1.4 Conclusion

In this subsection, the topology optimization is introduced under the framework of the inverse design for plasmonic nano-antennas. The details about this technique such as parameters' definition and topological process are well explained and discussed as well.

3.3.2 Objective function

In mathematical optimization and operations research, an objective function [47] is a function that that serves as a criterion for determining the best solution to an optimization problem. An optimization problem seeks to minimize or maximize the objective function.

In the inverse design of plasmonic nano-antennas domain, the demand for a physical phenomenon is usually translated into an objective function in a mathematical language. The precise definition of the objective function is a key factor in accurately describing this demand. In my Ph.D. projects, the best shape of a plasmonic nano-antenna or its corresponding 10-by-10 binary matrix needs to be found to maximize or minimize the objective function that we predefined according to the demand of a specific physical phenomena that we want the nano-antenna to realize. Based on that, the general mathematical formula for the objective function can be written as follows:

$$\underset{structure}{argmax}\, f\left(\boldsymbol{B}\right) \tag{7}$$

where f is an objective function that takes the stationary magnetic field $\boldsymbol{B}$ generated by the nanostructure as an input and its output is a value mathematically representing to a specific physical phenomenon related to the inverse Faraday effect which we want to obtain finally after optimization.

From the equation above, it clearly shows that a best structure or the best 10-by-10 binary matrix needs to be found to maximize the predefined objective function according to the expected physical phenomena which is normally related to the stationary magnetic fields induced by drift currents due to the inverse Faraday effect in my projects.

3.3.3 Metaheuristic algorithm

3.3.3.1 Introduction

Metaheuristic optimization algorithm is a modern optimization method which get ideas from some natural behaviors, some industrial process and so on. These methods are nearly all based on possibility with group search and use some technical means to avoid the local minimum which is crucial topic in optimization problems. The simulated annealing (SA) [48, 49], particle swarm optimization (PSO) [50], and genetic algorithm (GA) [51] are the three most representative methods among them. In the following sections, these three optimization algorithms will be introduced, and algorithm details will be discussed as well in order to gain a deeper understanding of the mechanisms behind them.

3.3.3.2 Simulated Annealing (SA)

The principle of simulated annealing is from the principle of metal annealing. In 1983, this approach was used by S. Kirkpatrick et al. [52] for a solution of the traveling salesman problem. They also proposed its current name, simulated annealing. The biggest advantage of simulated annealing is that it accepts bad solutions with probability in each iteration. This mechanism makes it possible for the search process to jump out of the local optimal solution. The algorithm flow is as follows:

(1) Initialization: the initial temperature T (sufficiently large), the initial solution state S (the starting point of the algorithm iteration), L is the number of iterations for each T

(2) Do steps (3) to (6) for $k = 1, \ldots, L$:

(3) Generate a new solution S'

(4) Calculate the increment $\Delta T = C(S') - C(S)$, where $C(S)$ is the evaluation function If $\Delta T < 0$, accept S' as the new current solution, otherwise accept S' as the new current solution with the probability $exp\left(-\frac{\Delta T}{T}\right) > random\_number$ ([0, 1]).

(5) If the termination condition is met, the current solution is output as the optimal solution, and the program ends.

(6) The termination condition is usually taken as the termination of the algorithm when several consecutive new solutions are not accepted or $T < T_{min}$.

(7) T decreases gradually ($T = \alpha \cdot T$ with $\alpha \in (0,1)$), and if $T > T_{min}$, then go to step (2).

So, the core of the simulated annealing optimization algorithm is the (4) step. If you get a better solution, then the better solution will be accepted unconditionally. If you get a bad solution, the bad solution will not be unconditionally discarded, but accepted by probability. This mechanism largely ensures that the algorithm can jump out of the local optimal solution and search in a larger solution space. Moreover, in the (2) step, the algorithm does not clearly indicate how the new solution should be generated, so simulated annealing is often used in

combination with other optimization algorithms to enable other algorithms to obtain the ability to jump out of the local optimal solution.

3.3.3.3 Particle Swarm Optimization (PSO)

The particle swarm optimization algorithm mainly uses the wisdom of the group to search for the optimal solution of an objective function that is discontinuous or cannot be differentiated. Each particle has its own position X_{id} and velocity V_{id} where *i* represents the i_{th} particle in the group and *d* represents the i_{th} particle after *d* times of updating. V_{id+1} refers to the i_{th} particle's velocity after $d+1$ time of updating which is used to get the next position X_{id+1} of the particle. The iteration rules are as follows:

$$
\begin{aligned}
&V_{id+1} = V_1 + V_2 + V_3 \\
&V_1 = \omega \cdot V_{id} \\
&V_2 = C_1 \cdot random\_number \cdot \left(P_{id} - X_{id}\right) \\
&V_3 = C_2 \cdot random\_number \cdot (P_d - X_{id}) \\
&X_{id+1} = X_{id} + lr \cdot V_{id+1}
\end{aligned}
$$

For the speed update, there are three parts V_1, V_2 and V_3. V_1 represents the inertia of the particle, and ω is called the inertia parameter. V_2 represents that the particle considers the best solution found by itself and obtains certain information from it. P_{id} represents the optimal solution found by the particle. C_1 is called cognitive attraction. V_3 represents that the particle considers the best solution found by all particles and obtains information from it. P_d represents the optimal solution found by the entire particle swarm. C_2 is called social attraction. *lr* is called learning rate which represents how much the particle will learn from itself and the whole group. Normally, $lr, random\_number \in [0,1]$ and $C_1, C_2 \in [0,4]$.

The choice of PSO parameters can have a large impact on optimization performance. Perez and Behdinan [53] demonstrated that the particle swarm is only stable if the following conditions are satisfied:

$$
\begin{aligned}
&0 < \left(C_1 + C_2\right) < 4 \\
&\left(\left(C_1 + C_2\right)/2\right) - 1 < \omega < 1
\end{aligned}
$$

If conditions shown above are both satisfied, the system will be guaranteed to converge to a stable equilibrium point. However, whether this point is the global minimum cannot be guaranteed, and its acceptability as a solution should be verified by the user. For particle swarm optimization algorithms, there are generally two termination conditions to choose from. One is the maximum number of iterations; the other is the difference between two adjacent iterations within a specified range.

3.3.3.4 Genetic Algorithm (GA)

The genetic algorithm (GA) is a metaheuristic inspired by the process of natural selection that belongs to the larger class of evolutionary algorithms. Genetic algorithms are commonly used to generate high-quality solutions to optimization and search problems by relying on biologically inspired operators such as selection, breeding and mutation [51]. Generally speaking, the biggest feature of this optimization algorithm is that it takes relatively little time to find a relatively good solution.

Specifically, the first key step of genetic algorithm is to code the parameters which need to be optimized using the most suitable form for following optimization. They will then play the role of DNA during the optimization process. There are multiple ways of coding the parameters such as binary code and so on. For example, Thorsten Feichtner et al. [54] demonstrated in 2012 that using a genetic algorithm with genetic information represented in a unique binary code i.e., the matrix elements are set to “1” if occupied by a gold cube and “0” when empty (Figure 3.5), they finally optimized a plasmonic nanostructure with high near-field intensity enhancement (Figure 3.6c). In this manuscript, binary code is also used for all projects where 1 represents the existence of material at one certain position and 0 refers to the vacuum there.

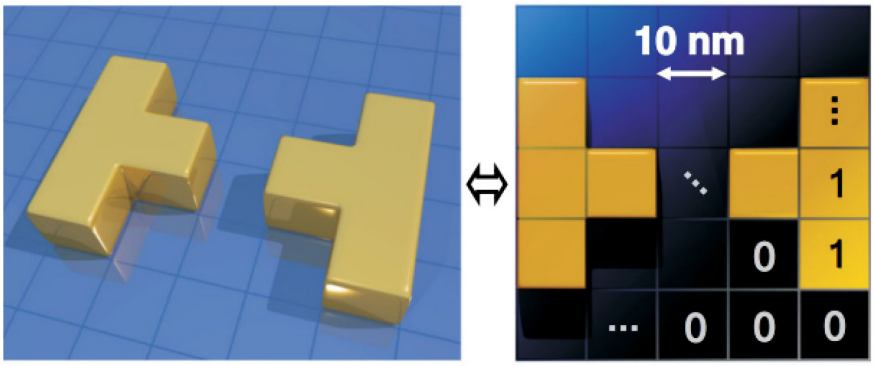

Figure 3.5 *: Taken from [54]. A representation of a nano-antenna based on topology optimization. Left: a 3D view of a bowtie nano-antenna consisting of eight gold cubes. Right: top view at an XY plane indicating the transition to a 5×5 binary matrix representation, where each ''1'' refers to the presence of a 10×10×11 nm³ block of gold material and each "0" indicates the absence of gold material.*

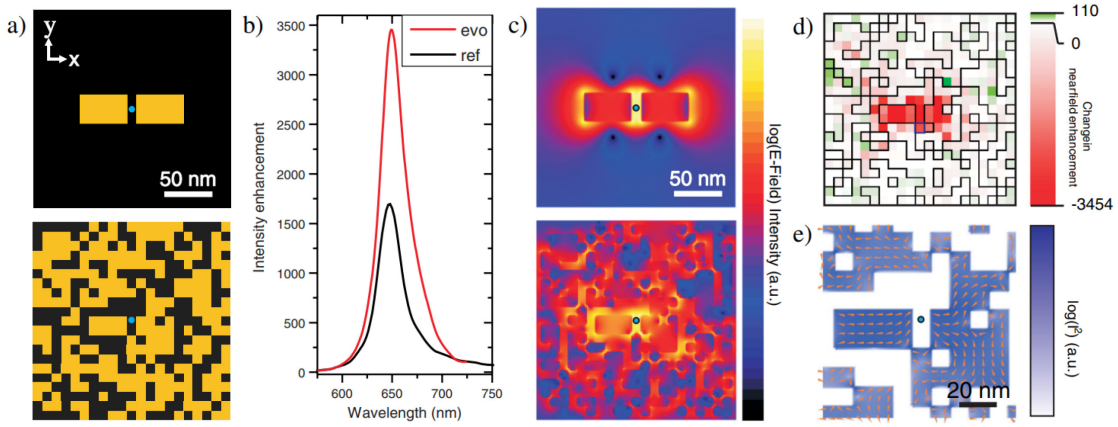

Figure 3.6 *: Taken from [54]. Comparison at wavelength of 647 nm between a resonant linear dipole nano-antenna built from two rectangular arms of 46×30×11 nm³ with a gap of 10 nm and a nano-antenna optimized by the Evolutionary Algorithm (EA). a) shows the geometry of both nanostructures from the +z direction at an XY plane. The blue spot refers to the position of the near-field optimization by the EA. The spectra in b) are taken at this blue marked position excited by a broadband Gaussian excitation. c) shows the logarithmic electric field intensities in near field at wavelength of 647 nm when the nanostructures are illuminated by a monochromatic Gaussian focus with NA = 1. In d) the change of near-field enhancement at the optimization position is shown for each single block when it is toggled. e) is a zoom of the central part of the optimized nano-antenna shown in the bottom of a), showing the strength and direction of the currents.*

Furthermore, there are three main operators during the GA optimization process which are selection, breeding, and mutation. **Selection**: The selection operator is to select good

structures in terms of their corresponding values of objective function in the last generation to keep good features for the following new generations. **Breeding**: The crossover operator for breeding is to use two selected structures' binary parameters from the last generation to create the new structures in the next generation by exchanging some parameters of these two selected structures. Therefore, as we can see this is an approach to increase the research region. **Mutation**: The mutation operator is to randomly chose some parameters of one selected structure to be randomly changed based on probability. This is also a technique to increase the research region. The whole general genetic algorithm process used for my Ph.D. projects is illustrated in Figure 3.7.

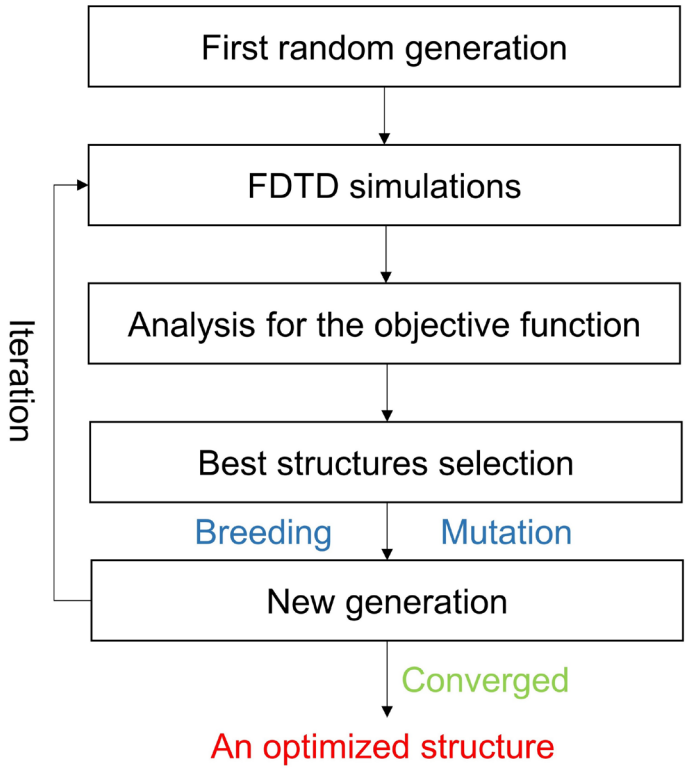

***Figure 3.7** : The workflow of genetic algorithm. Starting from a certain number of randomly initialized structures, the FDTD simulations will be applied to each of them to get the objective function values. Based on the values, new generation will be generated through selection, breeding, and mutation operators. The process will be iterated until algorithm is converged. Finally, an optimized structure is obtained.*

To be specific, in my Ph.D. projects, 200 random structures are generated for the first generation, and it always keeps the same number of structures for every generation. The size of generation is normally set to a relatively large number in order to guarantee the genetic algorithm be converged within that number of generations.

3.3.3.5 Conclusion

In this subsection, three most representative metaheuristic algorithms are reviewed and discussed. Considering the nature of the optimization problem here and the characteristic of each algorithm [55-60], we finally choose the genetic algorithm as the most suitable optimization algorithm to solve the inverse design problems of plasmonic nano-antennas for manipulating the inverse Faraday effect due to its excellent performance in solving unconstrained zero-one integer programming problems.

3.3.4 Conclusion

In summary, the inversely designed plasmonic nano-antennas based on topology optimization solved by genetic algorithm will be used to manipulate light locally in order to manipulate the inverse Faraday effect on demand. Three different related sub-projects will be discussed in the next three following chapters.

Chapter 4 A chiral inverse Faraday effect

4.1 Introduction

As described in chapter 1 and 2, the inverse Faraday effect (IFE) is a magneto-optical process enabling the magnetization of matter by optical excitation only (Figure 1.1). This magnetization is made possible by the action of non-linear optical forces on the matter's electrons. In particular, in a metal, the free electrons subject to these non-linear forces are set in a drift motion at the origin of the IFE. If we consider these electrons as free-moving charges, the expression of these drift currents can be described using the plasma community's formalism (Equation 5). These drift currents are, therefore, a function of the optical electric field and its divergence. Because of their ability to manipulate fields and field gradients, nanophotonics and nanoplasmonics are then particularly well suited to generate a strong IFE and thus create, through the Biot-Savart law (Equation 6), strong stationary magnetic fields ($\boldsymbol{B}$).

Moreover, a plasmonic IFE will confine the created $\boldsymbol{B}$-field to sub-wavelength scales due to its nanometric scales. Finally, the generation of the $\boldsymbol{B}$-field by IFE is due to light–matter interactions; therefore, by using ultra-short optical pulses, nanoplasmonics is today the only technique allowing the creation of intense, confined, and ultra-fast magnetic field pulses. These unique properties have applications in many fields of magnetic research and technology [61]. Indeed, since the pioneering work of Beaurepaire et al. [62], researchers have been looking for ways to manipulate and study magnetization at very short time and spatial scales [63-66], mainly through the use of femtosecond lasers, intending to control and accelerate current data storage technologies. Unfortunately, the physical processes involved in this type of interaction are still poorly understood. Likewise, the transient processes of magnetic interactions, such as spin precession, spin–orbit coupling, and exchange interactions, have their roots in the femtosecond time scale [67]. The ability to probe and address these different processes and their transient mechanisms using ultrashort pulses of magnetic fields would benefit countless research activities in magnetism: from Zeeman splitting [68], magnetic trappings [69], magnetic skyrmions [70], magneto-plasmonics [71], ultrafast magnetic modulations [72], and magnetic circular dichroism [73] to spin control [74], spin precession [75], spin currents [76], and spin waves [77].

In addition, the IFE is a symmetrical process, i.e., the magnetization of matter by a right circular polarized wave will be opposite to a left circular polarized wave. In particular, the magnetic field created for a right circular polarization will be oriented in the propagation direction of the light, and that of a left circular polarization will be oriented in a counter-propagative way (Figure 1.1). Although, by analogy with what has been demonstrated in the past in the chiral interactions between light and matter, it is known that a chiral nanostructure interacts differently with right or left circularly polarized light [78]. In these studies, this translates, for instance, into a different distribution of the local chirality density and/or measurements of far field circular dichroism on these chiral structures.

Here, we demonstrate the generation of a chiral IFE through the manipulation of light at the nanoscale and, in particular, via the local manipulation of the spin density (characterizing the degree of circular polarization of a wave). Using a genetic algorithm, we have generated a plasmonic nanostructure that creates a non-zero $\boldsymbol{B}$-field for a single helicity of light. Moreover, we show that the mirror image of the optimized plasmonic nanostructure generates a non-zero $\boldsymbol{B}$-field oriented in the opposite direction and only for the other helicity of light. Also, under the illumination conditions used here, the amplitude of the created $\boldsymbol{B}$-field is estimated to be 6 mT. Finally, this chiral IFE results from the photonic nanostructures' ability to manipulate light in the near field. Indeed, we demonstrate that this effect is due to generating a spin-density hot spot within this nanostructure for a single excitation polarization of light. These results are particularly important since they imply that this approach allows optically generating, even with unpolarized incoherent light, magnetic fields that are intense, ultrafast, nanoscale, and always oriented in the same direction. Thus, allowing for manipulation, at very short time and space scales, of many magnetic processes.

4.2 Results and discussions

Specifically, we have optimized, using a genetic algorithm [54, 79, 80], a plasmonic nanostructure made in a thin gold layer of 30 nm thickness deposited on a glass substrate (Figure 4.1). This nanostructure is based on a 2D matrix of 10-by-10 parameters, each parameter consisting of metal or air with a size of 28 nm, constituting a total structure size of 280*280 nm^2.

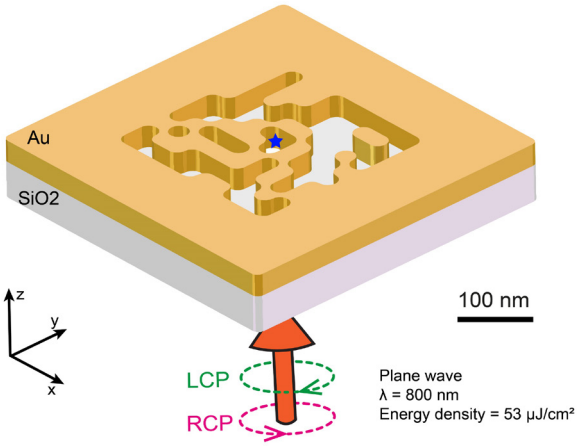

***Figure 4.1** : Optimized structure and excitation conditions. Example of a GA-optimized structure, realized in a 30 nm thick gold layer, for excitation by a right- or left-circular polarized plane wave at the wavelength of 800 nm and for an excitation energy density of 5.3 µJ/cm^2. The field **B** generated under the two excitation conditions (i.e., RCP and LCP) is evaluated at the center of the gold nanostructure in X, Y and Z (symbolized by the blue star).*

The excitation of the nanostructure is done by a circularly polarized plane wave, with a wavelength of 800 nm, launched from the substrate side and an energy density of 53 µJ/cm^2. This excitation power is chosen to be below the threshold of what the material can withstand [81, 82]. In addition, according to the Equation 5, it's observed that the amplitude of drift currents is strictly linearly proportional to the power density of incident wave. Thus, the amplitude of stationary magnetic fields is also linearly proportional to the power density of incident wave. Therefore, we can always decrease the power density of incident wave to avoid any non-desirable thermal effects and the IFE phenomenon will always exist regardless of the power intensity of incident wave. Each generation of the GA optimization is composed of 200 structures. For each structure, two simulations are performed, one with a right and another with a left circular polarization state of incoming light.

The topological process and mesh size for FDTD simulations have been described in the Figure 3.4 before. The choice of 1 nm mesh size for the central part is chosen because firstly convergence in the amplitude of the magnetic field is observed starting from this mesh size shown in Figure 4.2 below. In addition to that, the skin depth for gold material under the light excitation of 800 nm wavelength is around 3.89 nm. So, the mesh size for the area where the drift currents are calculated should be at least smaller than half of that value in order to guarantee the quality and precision of the FDTD simulation results especially for the calculation of drift currents according to its mathematical formula shown in the Equation 5. To summarize,

based on the two points mentioned before, 1 nm mesh size for the central part of the nano-antenna is the optimal choice with a balance between calculation time and quality of simulation results.

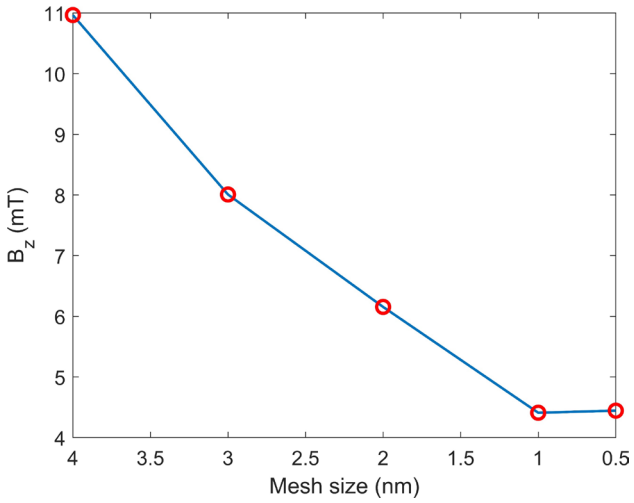

Figure 4.2 *: Amplitude of the stationary magnetic field oriented along Z and generated by the optimized nano-antenna for excitation by a right circular polarization and for different mesh sizes of the central zone. A convergence is observed from a mesh size of 1 nm, justifying the choice of the latter in the central zone of 140*140*32 nm^3.*

The excitation of the nano-antennas is performed by a pulsed plane wave of duration 5.3 fs spectrally centered at a wavelength of 800 nm. The peak power of the pulse is 10^{10} W/cm^2, which corresponds to an energy slightly lower than 0.048 pJ applied to the plasmonic nano-antennas (energy density of 53 µJ/cm^2). The convergence of the simulation was obtained when the energy inside the calculation window was lower than 10^{-5} of the initial injected energy. The optical response of each structure is calculated by a finite difference time domain method, and the associated electric field is then used to calculate the drift currents according to the non-linear Equation 5, in the center part of the structure. Hence, Biot-Savart law (Equation 6) estimates the field $\boldsymbol{B}$ generated under these two excitation conditions at the center of the nanostructure in X, Y and Z (symbolized by the blue star in Figure 4.1) from those calculated drift currents. Note that only the central volume of 1 nm mesh is considered to integrate the drift currents allowing the calculation of the $\boldsymbol{B}$ field via Equation 6. We then choose to maximize the difference $\boldsymbol{B}_{z-RCP} - abs\left(\boldsymbol{B}_{z-LCP}\right)$ as a GA optimization function, with $\boldsymbol{B}_{z-RCP}$ and $\boldsymbol{B}_{z-LCP}$ the $\boldsymbol{B}$-fields oriented along Z created by a right or left circular polarization, respectively. The evolution from a generation N to N + 1, N being the number of the generation, is then done by

keeping the 200 best structures of the generations 1 to N. The breeding of these 200 structures produces half of the structures of the generation N + 1, the other half being constituted of mutated structures with a mutation rate of 10 %. These optical and selection characteristics give an optimized structure after 76 generations (Shown 3D in Figure 4.1 and its XY plane in Figure 4.6a). The GA evolution process is shown in Figure 4.3 below. Each colored point in the Figure 4.3 represents one distinct structure and for each structure, two simulations with same conditions except polarization angle were performed in order to get the difference of stationary magnetic fields oriented along Z under two circular polarizations of excitation at a center point of the structure symbolized by the blue start in the Figure 4.1.

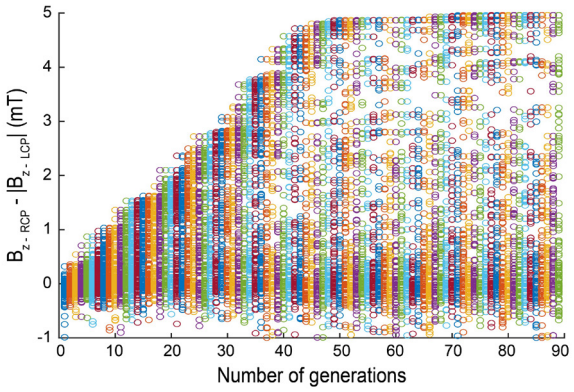

Figure 4.3 *: Evolutionary process. Evolution during the different generations of the optimization function consisting in maximizing the difference* $\boldsymbol{B}_{z-RCP} - abs(\boldsymbol{B}_{z-LCP})$, *with* $\boldsymbol{B}_{z-RCP}$ *and* $\boldsymbol{B}_{z-LCP}$ *the* ***B****-fields created by a right or left circular polarization, respectively. Each generation consists of 200 structures. The optimized structure appears after 76 generations.*

Moreover, the optical response of this optimized structure at an XY plane is shown in Figure 4.4 below.

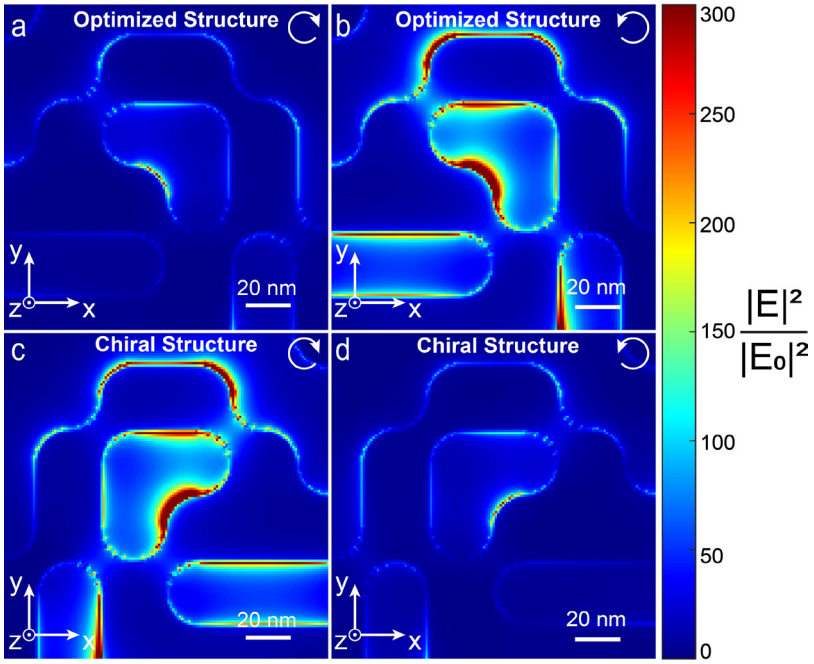

Figure 4.4 *: Optical responses in an XY plane. a) and b) spatial distributions of the optical electric intensity enhancement at the surface of the optimized structure (2 nm below the upper edge of the gold layer) for the left and right circular polarizations of excitation, respectively. c) and d) spatial distributions of the optical electric intensity enhancement at the surface of the mirror structure for the left and right circular polarizations of excitation, respectively. The white arrows indicate the polarization states of incoming light.*

From the optical response of this optimized structure (Figure 4.4) and via Equation 5, the associated drift currents are calculated inside the metal and their distributions at an XY plane is shown in Figure 4.5 below.

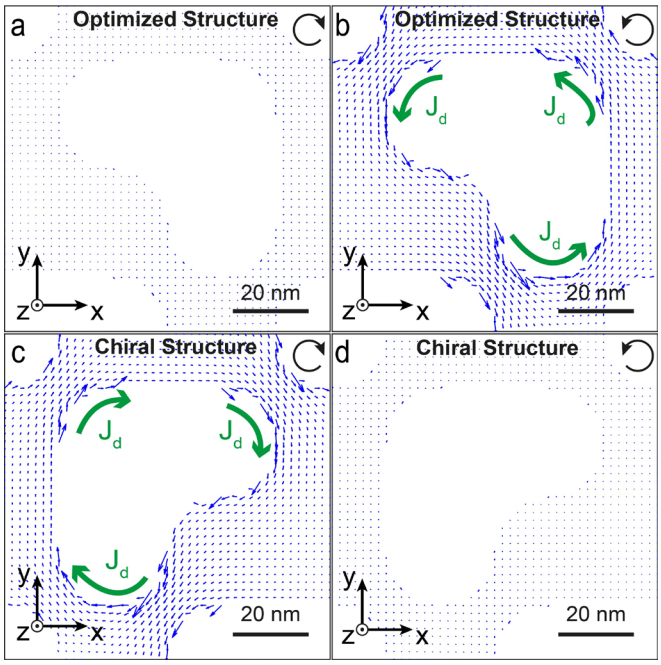

Figure 4.5 *: Distribution of drift currents in an XY plane. a) and b) spatial distributions of drift currents at the surface (2 nm below the upper edge of the gold layer) of the optimized structure for the left and right circular polarizations of excitation, respectively. c) and d) spatial distributions of drift currents at the surface of the mirror structure for the left and right circular polarizations of excitation, respectively. The black arrows indicate the polarization states of incoming light, the length of blue arrows represents the relative amplitude of drift currents.*

Using the Biot-Savart law, we calculate and show in Figure 4.6b and c the Z-oriented stationary magnetic field distribution in an XY plane at the Z-center of the optimized structure for left and right circular polarization, respectively. As can be seen, only the right circular polarization generates an intense ***B***-field of 6 mT, oriented in the direction of light propagation (along the positive Z), with an $abs\left(B_{RCP}\right)/abs\left(B_{LCP}\right)$ ratio of 11. Also, using the plasmonic mirror structure to the optimized one, we observe that under the same excitation conditions but for a left circular polarization, a ***B***-field of the same intensity is generated but oriented in a counter propagative way to the incident light (along the negative Z) and for a left circular polarization. This is the first time a chiral IFE has been observed, moreover with this intensity and at the nanoscale.

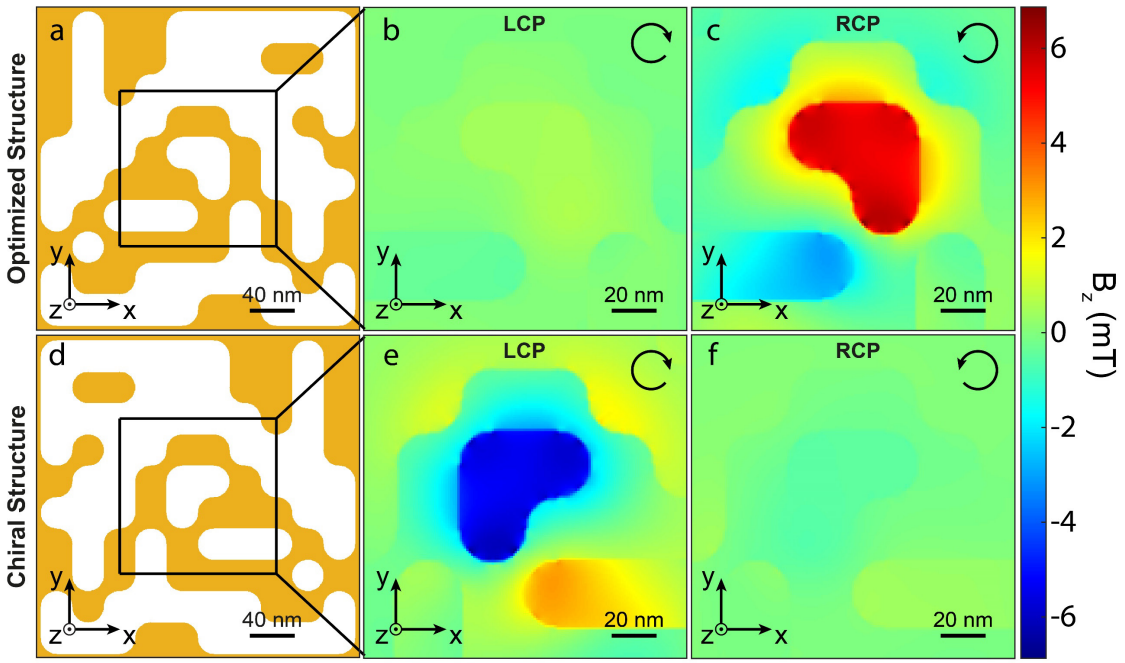

Figure 4.6 *: Stationary magnetic response of the optimized plasmonic nano-antennas. a) Schematic, in an XY plane, of the GA-optimized structure. b) and c) spatial distribution of the stationary magnetic field oriented along Z and generated in the Z-center of the structure within the black square range shown in a) for the left and right circular polarizations of excitation, respectively. d) Schematic, in an XY plane, of the mirror structure displayed in a). e) and f) spatial distributions of the* ***B****-field oriented along Z and generated in the Z-center of the mirror structure within the black square range shown in d) for the left and right circular polarizations of excitation, respectively. The black arrows indicate the polarization states of incoming light.*

What's more, the X and Y component of the ***B***-field at the same XY plane are shown in the Figure 4.7 below.

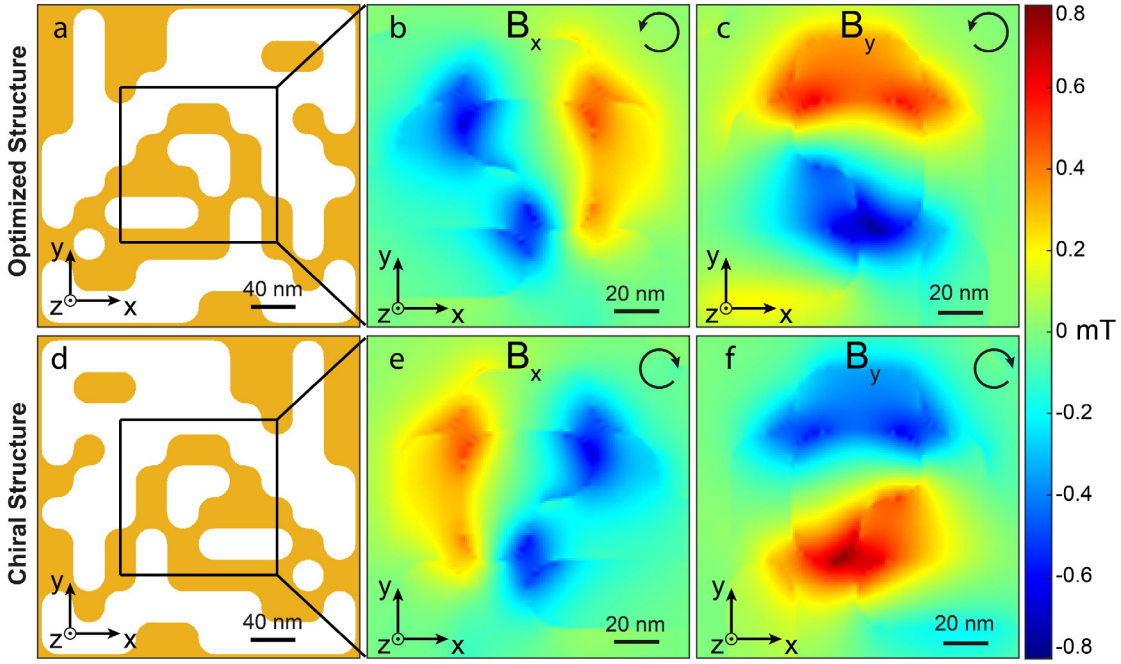

***Figure 4.7** : Vectorial stationary magnetic field components. a) Schematic, in an XY plane, of the GA-optimized structure. b) and c) spatial distributions of the **B**-field along X ($\boldsymbol{B}_x$) and the **B**-field along Y ($\boldsymbol{B}_y$) generated at the Z-center of the structure within the black square range shown in a) for the right circular polarizations of excitation. d) Schematic, in an XY plane, of the mirror structure. e) and f) Spatial distributions of $\boldsymbol{B}_x$ and $\boldsymbol{B}_y$ generated at the Z-center of the mirror structure within the black square range shown in d) for the left circular polarizations of excitation. The black arrows indicate the polarization states of incoming light.*

As can be seen, the Z component of stationary magnetic field is much stronger than its X component and Y component indicating that the direction of the stationary magnetic field is mainly dominated by its Z component.

In addition, as for full amplitude of the ***B***-field, the 2D and 3D distribution are shown in Figure 4.8 and Figure 4.9, respectively.

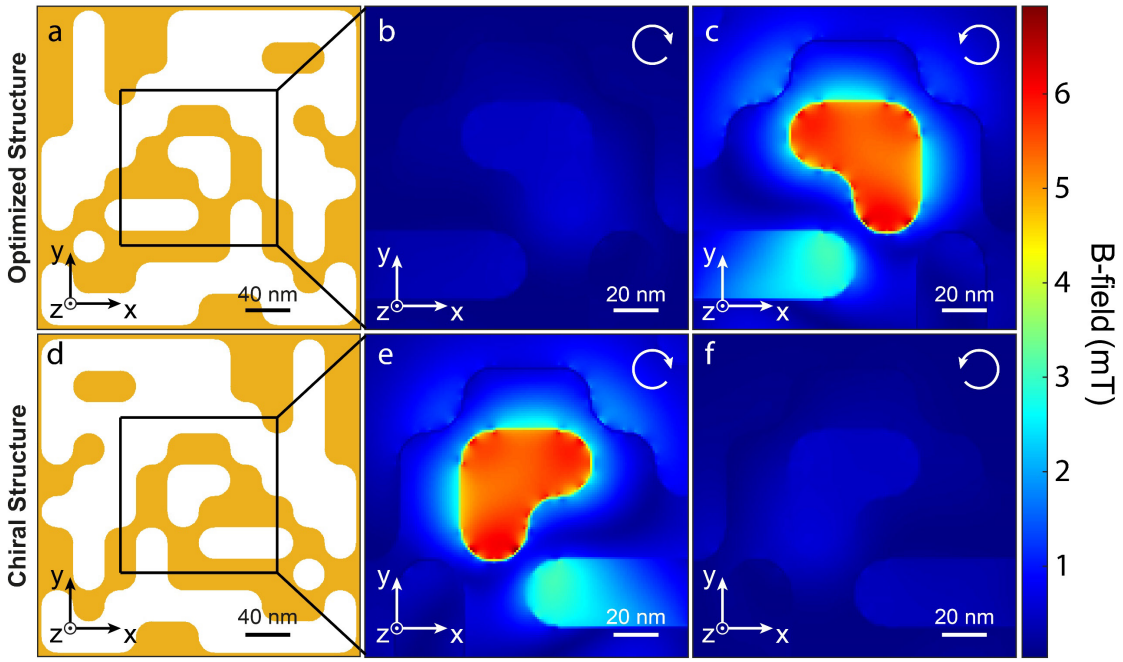

Figure 4.8 *: Amplitude of stationary magnetic fields. a) Schematic, in an XY plane, of the GA-optimized structure. b) and c) spatial distributions of the* ***B****-field amplitude at the Z-center of the structure within the black square range shown in a) for the left and right circular polarizations of excitation, respectively. d) Schematic, in an XY plane, of the mirror structure. e) and f) spatial distributions of* ***B****-field amplitude at the Z-center of the mirror structure within the black square range shown in d) for the left and right circular polarizations of excitation, respectively. The white arrows indicate the polarization states of incoming light.*

It's observed that a chirality for the IFE is generated by the GA optimized structure as well as its chiral structure.

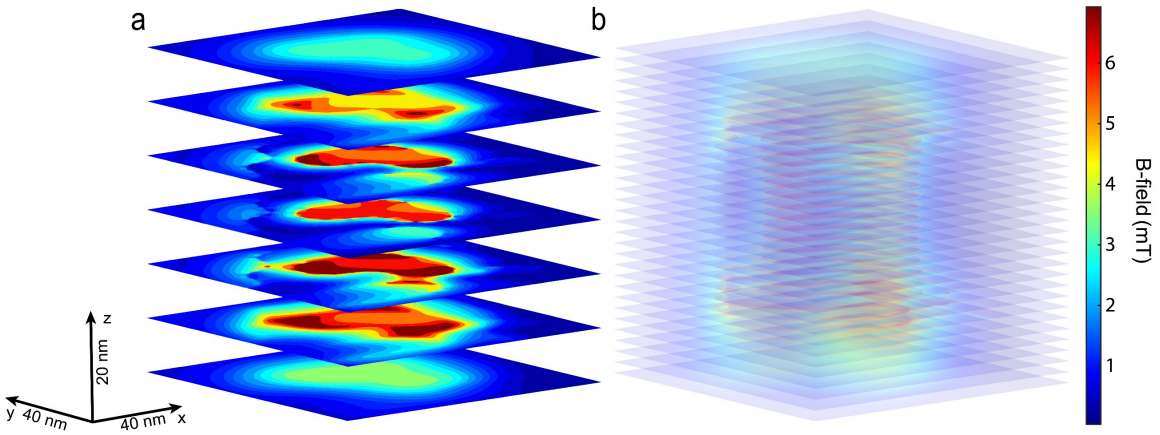

Figure 4.9 *: Amplitude of stationary magnetic fields in 3D. The amplitude distributions of the stationary magnetic field* ***B*** *at XY planes in different Z planes from -15 nm below the gold layer to +15 nm above it in steps of a) 10 nm and b) 2 nm. The distributions in figure b) are partially transparent to obtain a 3D representation of this stationary magnetic field distribution.*

From the Figure 4.9, we can see the amplitude of stationary magnetic field distributions in 3D are quite uniform only the values will change a little bit with the Z plane changes demonstrating a good chirality in 3D.

The observation of this new physical effect is due to the ability of optical nano-antennas to manipulate light and its characteristics in the near field. Indeed, it is known that the manipulation of electromagnetic fields in the near field allows, for instance, to control of local densities of states [83-85], radiation patterns [86], chirality densities [87, 88], or even some nonlinear effects [89]. However, from Equation 5, we can see that a necessary condition must be met to generate drift currents at the origin of the IFE (i.e., the light incident on the metal must carry a certain degree of ellipticity). In particular, we can see that a right circular or elliptical polarization will generate a stationary magnetic field oriented in the same direction as the propagation of the light. In contrast, a left circular polarization will create it opposite to the propagation direction (Figure 1.1). Also, a linear polarization will not generate a drift current and, therefore, no magnetic field. Here, we use the unique properties of plasmonic nanostructures to manipulate the spin densities of light locally, or in other words, the local helicity of light to generate a chiral IFE. The equation describing the electric spin density of light is:

$$\boldsymbol{s} = \frac{1}{|\boldsymbol{E}_0|^2}\,\mathrm{Im}\left(\boldsymbol{E}^* \times \boldsymbol{E}\right) \tag{8}$$

With $\boldsymbol{E}_0$ being the electric field of the incoming light.

The spin density is a vectorial physical quantity that describes the polarization state of light in a given plane. This density can take positive or negative values corresponding to a right or left elliptical polarizations. In particular, in our reference system, a positive spin density corresponds to a right-handed helicity, a negative spin density corresponds to a left-handed helicity, and a zero density corresponds to a linear polarization. The distributions of spin density at the center XY plane are shown in Figure 4.10 below.

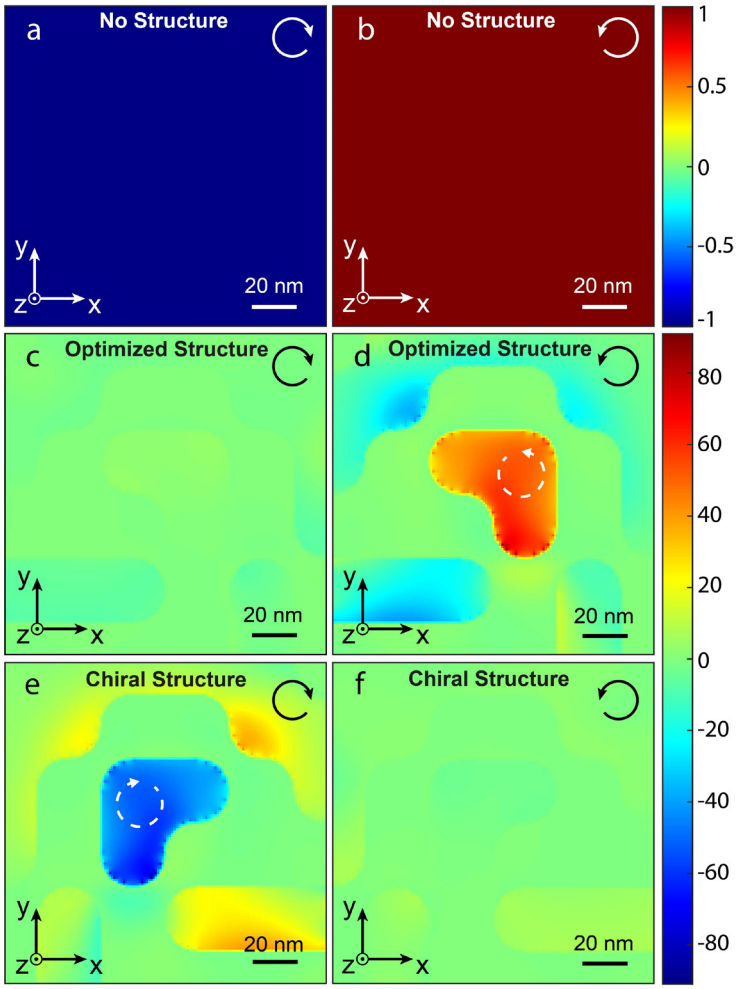

Figure 4.10 *: Distributions of spin density. (a) and (b) spin density for left and right circularly polarized plane waves, respectively. (c) and (d) local spin density in the Z-center of the optimized plasmonic nano-antenna for left and right circular polarization of excitation, respectively. (e) and (f) local spin density in the Z-center of the mirror plasmonic structure of the optimized one, for excitation by (e) a left or (f) right circularly polarized wave. The white and black arrows indicate the polarization states of incoming light, the white dashed arrows show the direction of local elliptical polarization states.*

In the far field, the spin density can only take values between −1 and 1, −1 being a left circular polarization and 1 a right circular polarization (Figure 4.10a and b). On the other hand, in the near field, the spin density normalized to the incident intensity $|\boldsymbol{E}_0|^2$ can take much larger values due to the increase of the fields, leading to the concept of super-circular light by analogy with super-chiral light [33]. Therefore, since the generation of drift currents requires an elliptical or circular polarization (Equation 5), by creating locally non-zero spin densities, the generation of an IFE is possible in a plasmonic nano-antenna. Here, the chiral property of our optimized design comes from the fact that for excitation for two different circular polarizations,

only one polarization generates locally a non-zero spin density (Figure 4.10c and d), the one that is right circular (Figure 4.10d). This behavior results from constructive and destructive interferences of the light locally around the plasmonic structure. Similarly, for the mirror plasmonic structure (Figure 4.10e and f), only one opposite light helicity generates a non-zero spin density, the left circular polarization (Figure 4.10e). Moreover, as can be seen in Figure 4.10d and e, the signs of the local spin densities generated in the nanostructures are opposite. It is positive in the case of a right circular excitation (Figure 4.10d), corresponding to a right elliptical polarization, and negative in the case of a left circular excitation (Figure 4.10e), corresponding to a left elliptical polarization. As a result of the IFE, the optimized structure thus generates a $\boldsymbol{B}$-field oriented in the propagating wave direction and the mirror structure in the counter-propagating one. Finally, the high amplitude of the generated $\boldsymbol{B}$-field is directly related to the super-circular nature of the light generated by these plasmonic nano-antennas, creating, in turn, strong drift currents.

4.3 Conclusion

In conclusion, in this sub-project, we have demonstrated for the very first time that the magneto-optical process of the inverse Faraday effect can be a chiral mechanism occurring only for one helicity of incoming light. This new physical effect is due to manipulating the light polarization locally at the nanoscale. Using an inverse design algorithm (i.e., genetic algorithm) based on natural selection with topology optimization technique, we have shown the generation of a non-zero spin density locally in a plasmonic nano-antenna only for a single helicity of incoming light, making the selective magnetization possible as a function of the excitation polarizations. Also, we have demonstrated that using a mirror structure obtained through the mirror symmetry to the GA-optimized structure allows the generation of a $\boldsymbol{B}$-field equivalent in size and amplitude but of opposite orientation, demonstrating a chirality effect in terms of the stationary magnetic fields. Finally, due to the super-circular light created by these nanostructures, a concept which is similar to super-chiral light and describes an elliptical polarization of the light where the optical electric fields are strongly increased, the generated $\boldsymbol{B}$-field has amplitude of 6 mT, which makes it one of the most intense generated at these scales and by the inverse Faraday effect.

Chapter 5 A reversed inverse Faraday effect

5.1 Introduction

As described in the previous chapters, from Equation 5, we can see that in order to generate drift currents at the origin of the IFE, the light incident on the metal must carry some degree of ellipticity. Specifically, we note that a right circular or elliptical polarization will generate a magnetic field oriented in the same direction as the propagation of the light. In contrast, a left circular polarization will create it in the opposite direction of propagation (Figure 1.1).

In this sub-project, we demonstrate, by manipulating light at the nanoscale, that we can generate a reversed inverse Faraday effect, i.e., an inverse Faraday effect whose magnetization is oriented in the direction of light propagation for a left circular polarization and oriented in the opposite direction to the propagation of light for a right circular polarization, as opposed to a so-called “classical” inverse Faraday effect.

To do so, we have inversely designed, thanks to an evolutionary algorithm, a plasmonic nanostructure allowing us to manipulate the polarization of the light around this nanostructure locally. In particular, the created nano-object allows us to generate a left ellipticity of the light in the near-field for an excitation by a right circularly polarized light and, conversely, a right local ellipticity for an excitation by a left circularly polarized light. Also, due to the optical field enhancement capability of the plasmonic nanostructure, we show that this reversed inverse Faraday effect is very efficient, allowing the generation of a 6 mT stationary magnetic field for the light power considered in this study. Finally, thanks to the possibility of inverse design algorithms to optimize several parameters simultaneously, the plasmonic nano-objects developed here possess chirality properties allowing this reversed inverse Faraday effect to generate a single helicity of light, the mirror structure creating a non-zero stationary magnetic field for the reverse helicity.

5.2 Results and discussions

In this sub-project, using a genetic algorithm (GA), we inversely optimized a plasmonic nanostructure made in a thin gold layer of 30 nm thickness deposited on a glass substrate shown in Figure 5.1.

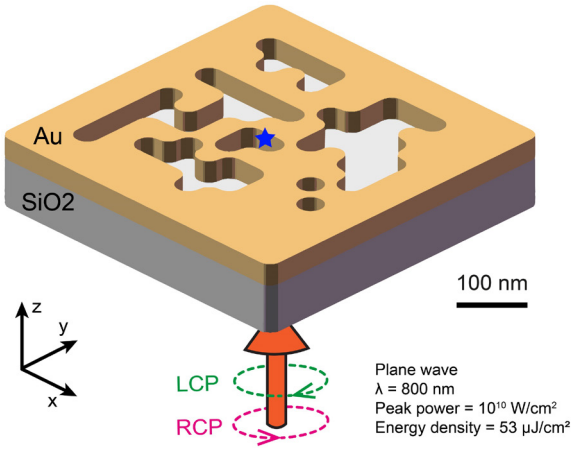

Figure 5.1 *: Optimized structure and excitation conditions. An example of a GA-optimized nano-antenna, consisting of a 30 nm thick gold layer and designed for excitation by a plane wave with a right- or left-circular polarization at a wavelength of 800 nm and an excitation energy density of 53 µJ/cm², is shown. The resulting stationary magnetic field* ***B*** *generated under these two excitation conditions is assessed at the center of the gold nanostructure in the X, Y, and Z directions, as represented by the blue star in the structure.*

As previously discussed, the mesh size, topological process and other FDTD simulations' parameters are kept same. To create the desired reversed inverse Faraday effect, each generation of the GA optimization was composed of 200 structures, and for each structure, two simulations were performed using right and left circular polarizations. The associated drift currents were calculated (Equation 5), and Biot-Savart law (Equation 6) estimated the Z-components of the fields $\boldsymbol{B}_{RCP}$ and $\boldsymbol{B}_{LCP}$, generated under these two excitation conditions at the center of the nanostructure in X, Y, and Z (symbolized by the blue star in Figure 5.1), where $\boldsymbol{B}_{RCP}$ corresponds to the stationary magnetic field under a right circular polarization of excitation, and $\boldsymbol{B}_{LCP}$ corresponds to the left circular polarization. We then chose, as an objective function of GA optimization, to maximize the difference $abs\left(\boldsymbol{B}_{z-RCP}\right)-abs\left(\boldsymbol{B}_{z-LCP}\right)$ with $\boldsymbol{B}_{z-RCP}$ being negative which is not the case for the sub-project in chapter 4. This objective function's purpose was to generate a chiral response of the plasmonic structure and create a

reversed IFE. The evolution from a generation N to N+1, N being the number of the generation, was achieved by keeping the 200 best structures from generations 1 to N and breeding them to produce half of the elements of the next generation, with the other half being constituted of mutated elements with a mutation rate of 10%. The GA evolution process is shown in the Figure 5.2 below.

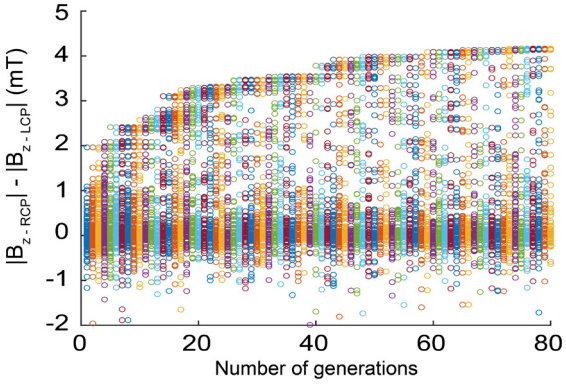

Figure 5.2 *: Evolutionary process. Evolution during the different generations of the objective function consisting in maximizing the difference* $abs(\boldsymbol{B}_{z-RCP}) - abs(\boldsymbol{B}_{z-LCP})$ *with* $\boldsymbol{B}_{z-RCP}$ *being negative,* $\boldsymbol{B}_{z-RCP}$ *and* $\boldsymbol{B}_{z-LCP}$ *are the Z component* ***B****-fields created by a right or left circular polarization, respectively. Each generation consists of 200 structures. The optimized structure appears after 73 generations.*

As can be seen, after 73 generations, an optimized structure is found, represented in Figure 5.3a. The optical response of this nano-antenna is shown in Figure 5.3b and c. These figures show the distribution of the electric field enhancement in an XY plane at the Z surface of the gold layer for excitation by a left and right circularly polarized light, respectively.

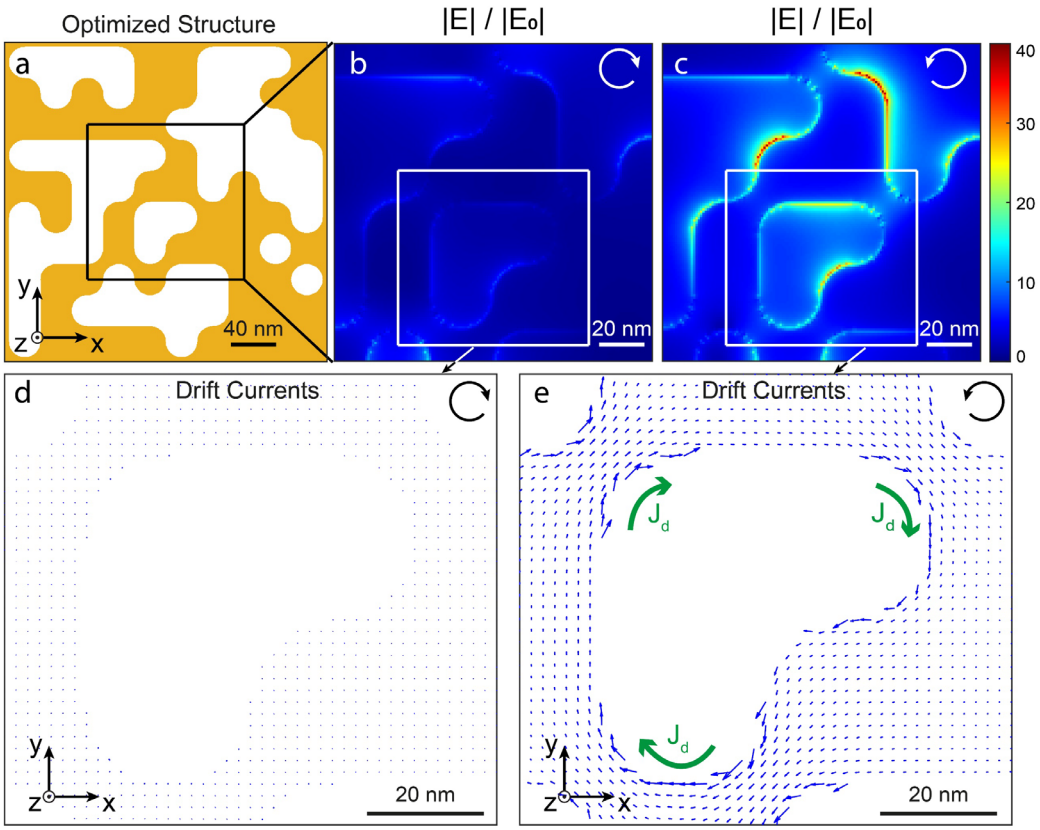

Figure 5.3 *: a) Schematic of the GA-optimized nanostructure in an XY plane. Spatial distribution of the electric field normalized by the incident wave at the Z-surface of the optimized nano-antenna and in an XY plane symbolized by the black square in a) for excitation by a b) left and c) right circularly polarized plane wave. Spatial distribution of drift currents at the Z-surface of the optimized nanostructure in an XY plane symbolized by the white squares in b) and c), for excitation by a d) left and e) right circularly polarized light. The white and black arrows indicate the polarization states of incoming light, the length of blue arrows in d) and e) represents the relative amplitude of drift currents.*

As one can see, only the right circular polarization strongly increases the electric field locally, in good agreement with the optimization function given to the GA (the chirality objective). From these electric field distributions and via Equation 5, the drift currents present in the metal are calculated and plotted in Figure 5.3d and e in the same plane as the electric field distribution. These currents exist only for one polarization of the light, the right circular polarization, in good agreement with the chirality objective as well. Finally, these currents have a clockwise symmetry while the right circular polarization used to excite the nano-antenna has an anti-clockwise symmetry, also in good agreement with the GA selection and opposite to a "classical" inverse Faraday effect. The 3D spatial distributions of drift currents, spin density and stationary magnetic field oriented along Z direction are also shown below in Figure 5.4.

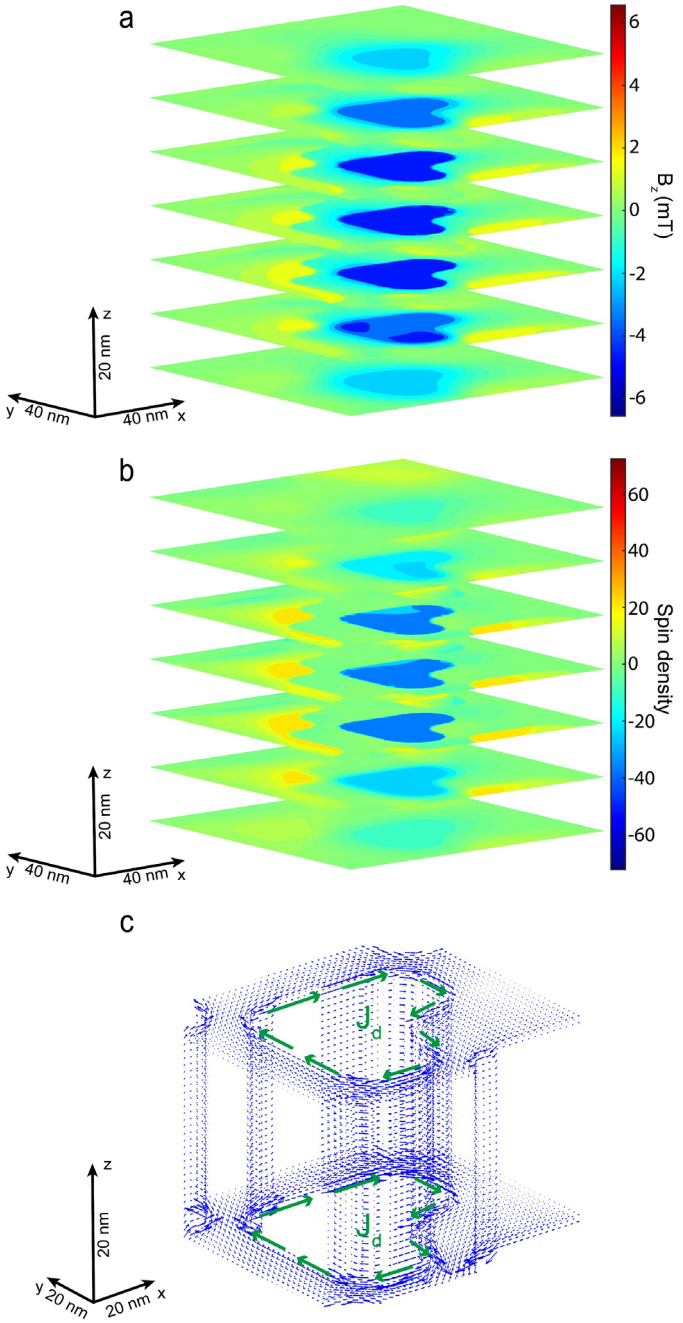

Figure 5.4 *: 3D spatial distributions. a) XY distribution of stationary magnetic field oriented along Z in different Z planes from -15 nm below the gold layer to +15 nm above it in steps of 10 nm. b) XY distribution of spin density in different Z planes from -15 nm below the gold layer to +15 nm above it in step of 10 nm. c) XY distribution of drift currents in different Z planes from the bottom of the gold layer to the top surface of the gold layer in steps of 1 nm (The green arrows in c) show the direction of drift currents). The length of blue arrows in c) represents the relative amplitude of drift currents.*

From these currents and via Equation 6, it is then possible to calculate the stationary magnetic field generated by the optimized nano-antenna. The Figure 5.5 below represents these

distributions of the stationary magnetic field oriented along Z at the center of the optimized plasmonic nano-antenna.

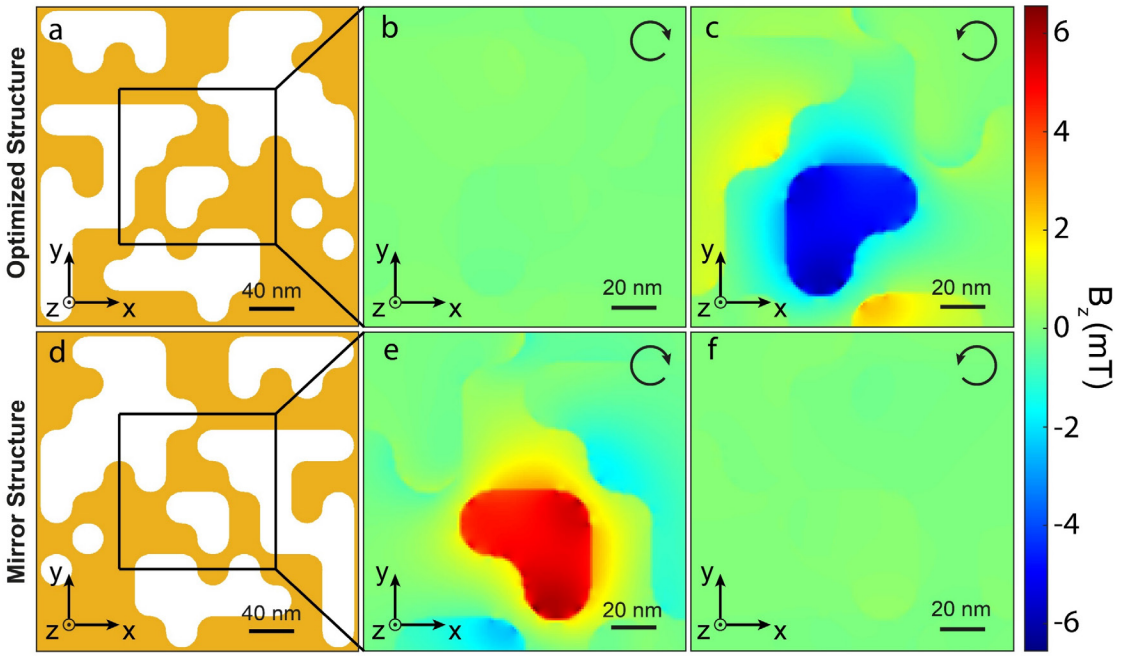

Figure 5.5 *: Magnetic response of the optimized plasmonic nano-antennas. a) This figure shows again a schematic of the GA-optimized structure in an XY plane. b) and c) the spatial distribution of the stationary magnetic field oriented along Z generated in the Z-center of the structure within the black square range shown in a) is displayed for left and right circular polarizations of excitation, respectively. d) The figure also includes a schematic of the mirror structure displayed in a) in an XY plane. e) and f) spatial distributions of the* ***B****-field oriented along Z and generated in the Z-center of the mirror structure within the black square range shown in d) for left and right circular polarizations of excitation, respectively. The black arrows indicate the polarization states of incoming light.*

In particular, Figure 5.5b and c represent the magnetic field in an XY plane at the center Z of the optimized structure described in Figure 5.5a, derived from the drift currents described in Figure 5.3d and e, respectively, for left and right circularly polarized excitation. What's more, the distributions of full amplitude of the stationary magnetic fields are shown in Figure 5.6 below.

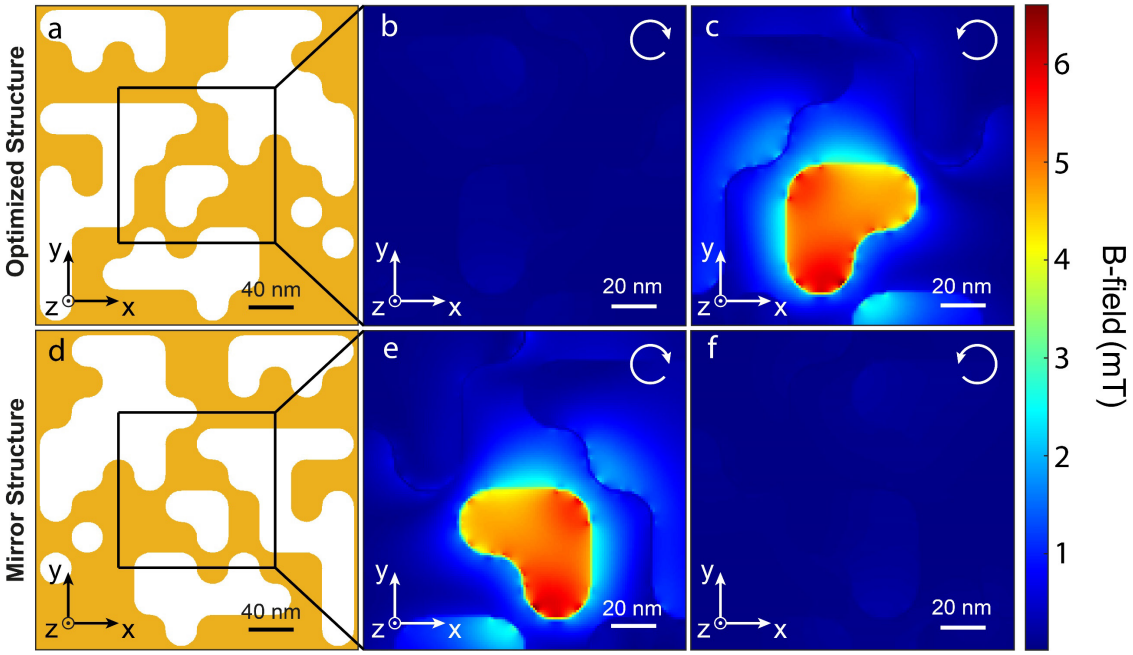

Figure 5.6 *: Amplitude of stationary magnetic fields. a) Schematic, in an XY plane, of the GA-optimized structure. b) and c) spatial distributions of the* ***B****-field amplitude at the Z-center of the structure within the black square range shown in a) for the left and right circular polarizations of excitation, respectively. d) Schematic, in an XY plane, of the mirror structure. e) and f) spatial distributions of* ***B****-field amplitude at the Z-center of the mirror structure within the black square range shown in d) for the left and right circular polarizations of excitation, respectively. The white arrows indicate the polarization states of incoming light.*

Once again, we can see that a stationary magnetic field is generated for only one excitation polarization, the right circular one, demonstrating the chiral effect expected by the optimization function. Also, and as expected in this study, the magnetic field generated by the structure of Figure 5.5a is negative and thus oriented towards negative Z, in contrast to a "classical" IFE, which magnetizes the matter in the direction of light propagation for this type of polarization of excitation. This result shows that manipulating light at the nanoscale allows the generation of a reversed IFE, which was not believed possible until today.

Also, and as requested in the optimization code, when the mirror structure is used (Figure 5.5d), a magnetic field is generated only for the opposite polarization, i.e., left circular (Figure 5.5e and f), in this case, positive and thus always opposite to the magnetization by a "classical" IFE (see Figure 5.4a for a 3D representation of the magnetic field in the structure). Furthermore, if we consider drift currents of whole volumetric area of the nanostructure, the stationary magnetic field oriented along Z and its full amplitude are shown in Figure 5.7 and Figure 5.8, respectively.

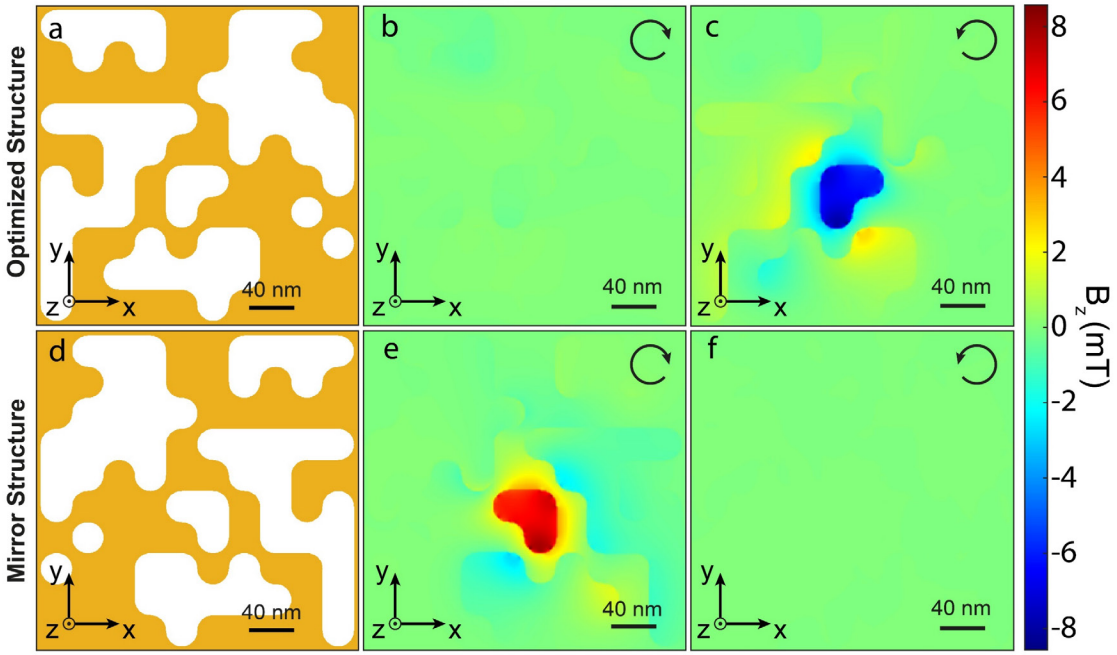

Figure 5.7 *: Magnetic response of the optimized plasmonic nano-antennas. a) This figure shows a schematic of the GA-optimized structure in an XY plane. b) and c) the spatial distribution of the stationary magnetic field oriented along Z induced by the whole volumetric drift currents of the nano-antenna generated in the Z-center of the structure shown in a) is displayed for left and right circular polarizations of excitation, respectively. d) The figure also includes a schematic of the mirror structure displayed in a) in an XY plane. e) and f) spatial distributions of the* ***B****-field oriented along Z induced by the whole volumetric drift currents of the nano-antenna and generated in the Z-center of the mirror structure shown in d) for left and right circular polarizations of excitation, respectively. The black arrows indicate the polarization states of incoming light.*

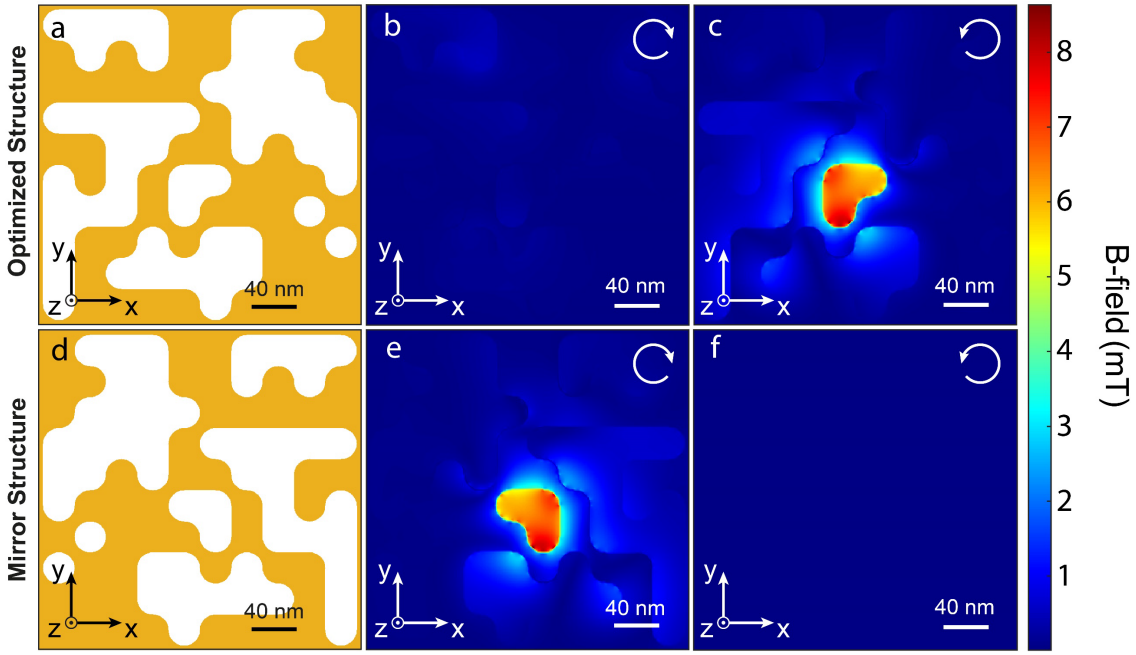

Figure 5.8 *: Amplitude of stationary magnetic fields. a) Schematic, in an XY plane, of the GA-optimized structure. b) and c) spatial distributions of the* ***B****-field amplitude induced by the whole volumetric drift currents of the nano-antenna at the Z-center of the structure in a) for the left and right circular polarizations of excitation, respectively. d) Schematic, in an XY plane, of the mirror structure. e) and f) spatial distributions of* ***B****-field amplitude induced by the whole volumetric drift currents of the nano-antenna at the Z-center of the mirror structure shown in d) for the left and right circular polarizations of excitation, respectively. The white arrows indicate the polarization states of incoming light.*

From the Figure 5.7 and 5.8, compared with the Figure 5.5 and 5.6, the distributions of the stationary magnetic field don't change at all, but the values increase since much broader range of drift currents are considered to estimate the stationary magnetic fields. It implies that the GA optimized nano-antenna can generate the reversed inverse Faraday effect at the global range presenting also a global chirality. What's more, the Figure 5.9 and Figure 5.10 show the distribution of the stationary magnetic field oriented along Z and its full amplitude under linear polarizations of excitation with different polarization angles but same energy density as before, respectively.

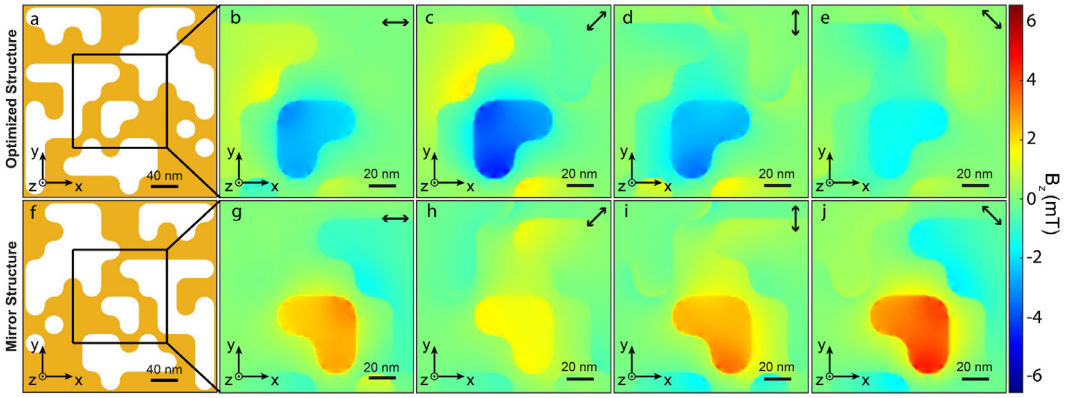

Figure 5.9 *: Magnetic response of the optimized plasmonic nano-antennas. a) Schematic, in an XY plane, of the GA-optimized structure. b-e) Spatial distributions of stationary magnetic fields oriented along Z and generated in the Z-center of the structure within the black square range shown in a) for 0-, 45-, 90-, and 135-degree linear polarizations of excitation, respectively. d) Schematic, in an XY plane, of the mirror structure. g-j) Spatial distributions of stationary magnetic fields oriented along Z and generated in the Z-center of the mirror structure within the black square range shown in f) for 0-, 45-, 90-, and 135-degree linear polarizations of excitation, respectively. The black double arrows indicate the linear polarization states of incoming light.*

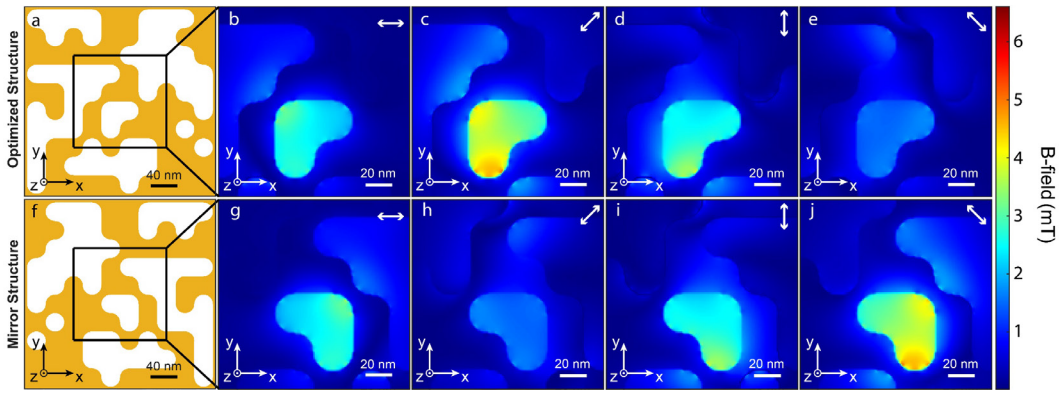

Figure 5.10 *: Amplitude of stationary magnetic fields for linear polarizations of excitation. a) Schematic, in an XY plane, of the GA-optimized structure. b-e) Spatial distributions of stationary magnetic field amplitude generated in the Z-center of the structure within the black square range shown in a) for 0-, 45-, 90-, and 135-degree linear polarizations of excitation, respectively. d) Schematic, in an XY plane, of the mirror structure. g-j) Spatial distributions of stationary magnetic field amplitude and generated in the Z-center of the mirror structure within the black square range shown in f) for 0-, 45-, 90-, and 135-degree linear polarizations of excitation, respectively. The white double arrows indicate the linear polarization states of incoming light.*

From the Figure 5.9 and Figure 5.10, due to the chirality of the GA optimized nano-antenna, it can still generate strong stationary magnetic fields under linear polarizations of

excitation with any polarization angles at the same energy density. Besides, the spectral response for the nano-antenna is also shown below in Figure 5.11.

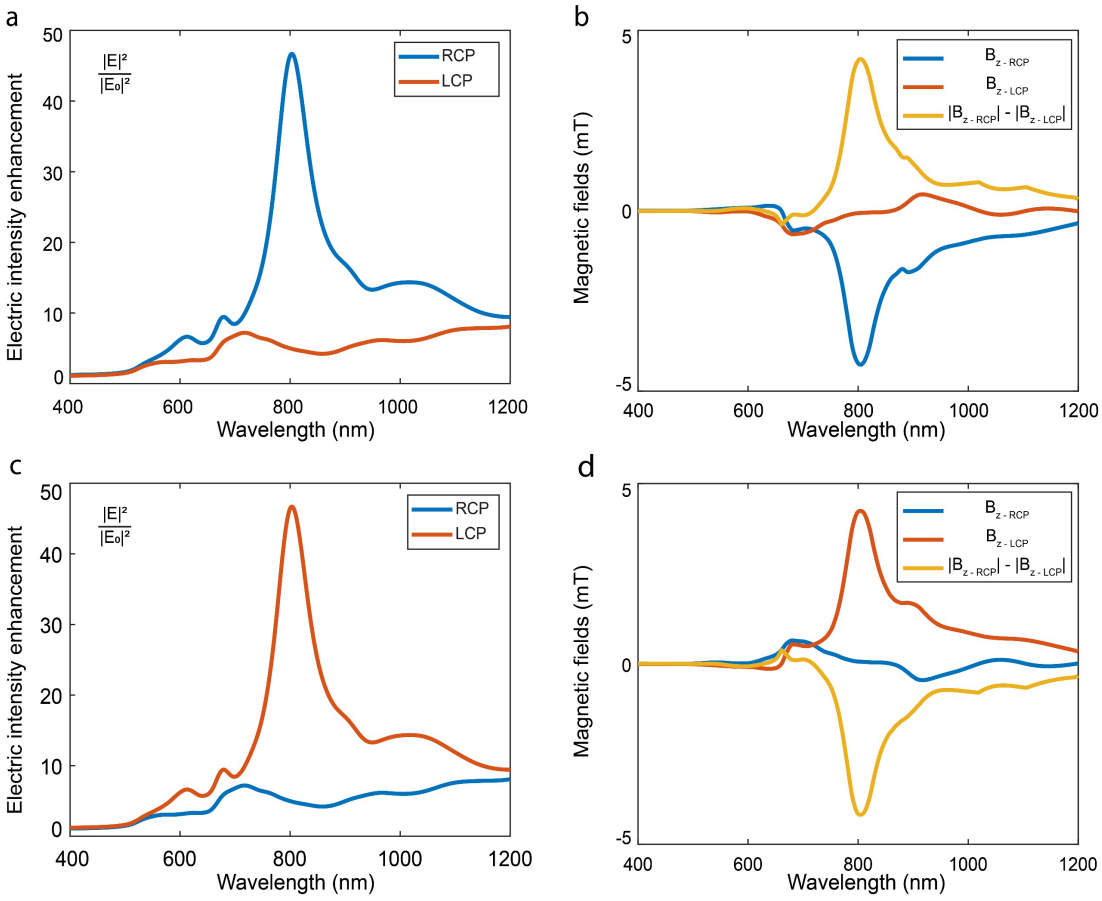

Figure 5.11 *: Spectral responses for the optimized nanostructure and its mirror structure. a) and b) spectral responses of electric field intensity enhancement and Z-oriented stationary magnetic field at the center point (symbolized by the blue star in the Figure 5.1) for the optimized structure, respectively. c) and d) spectral responses of electric field intensity enhancement and Z-oriented stationary magnetic field at the same center point for the mirror structure, respectively.*

As can be seen from the Figure 5.11 above, the GA optimized structure has very sharp spectral responses within the range of 400 nm to 1200 nm only for right circular polarization (Figure 5.11a and b) and its mirror structure has also very sharp spectral responses only for left circular polarization (Figure 5.11c and d) since they all have one main peak at 800 nm wavelength under which the GA algorithm is performed implying the success of GA optimization process.

In addition, it is also interesting to note that the structure generated by the GA is quite robust and depends very little on the overall dimensions of the structure. The Figure 5.12 below

shows the behavior of the GA optimized nano-antenna in terms of magnetic field generation for structures identical in shape but of varying dimensions.

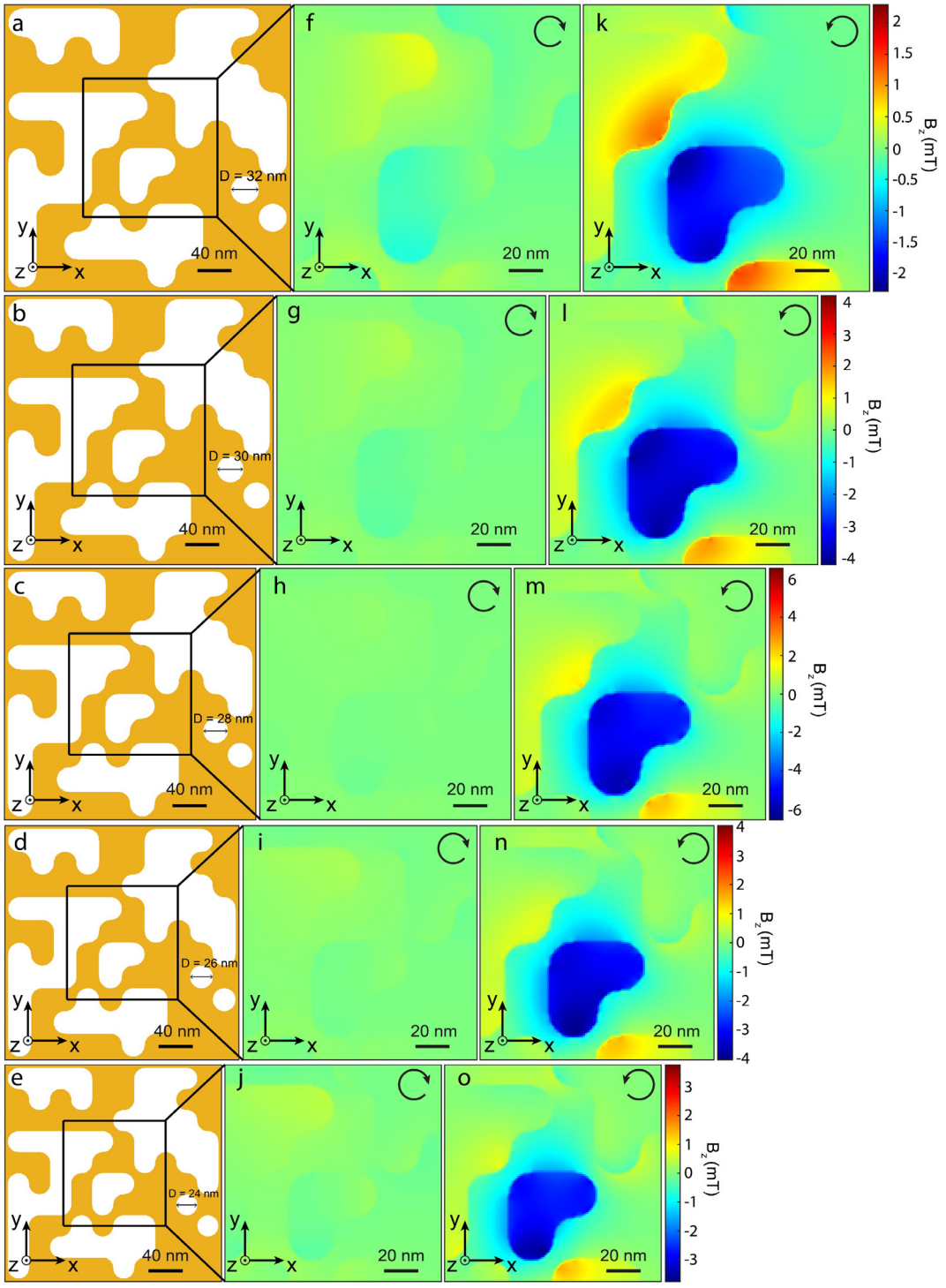

Figure 5.12 *: Schematic diagrams and stationary magnetic field distributions for different dimensions of the optimized nanostructure and different polarizations of excitation. a-e) Schematic diagrams of the optimized structure for different dimensions. f-j) Stationary magnetic field distributions at the Z-center of the structures within the black square range described respectively in a-e) for a left circular polarization of excitation. k-o) Stationary*

magnetic field distributions at the Z-center of the structures within the black square range described respectively in a-e) for a right circular polarization of excitation. The black arrows indicate the polarization states of incoming light.

The ability of optical nano-antennas to manipulate light and its characteristics in the near field is at the origin of this new physical effect. The spin density as described in Equation 8 in the chapter 4 is a vectorial physical quantity that describes the polarization state of light in a given plane. Here, in this sub-project we still use the unique ability of plasmonic nano-antennas to locally manipulate the spin densities of light, or in other words, its local helicity, to generate a reversed IFE. The distributions of spin density at an XY plane are shown in Figure 5.13 below.

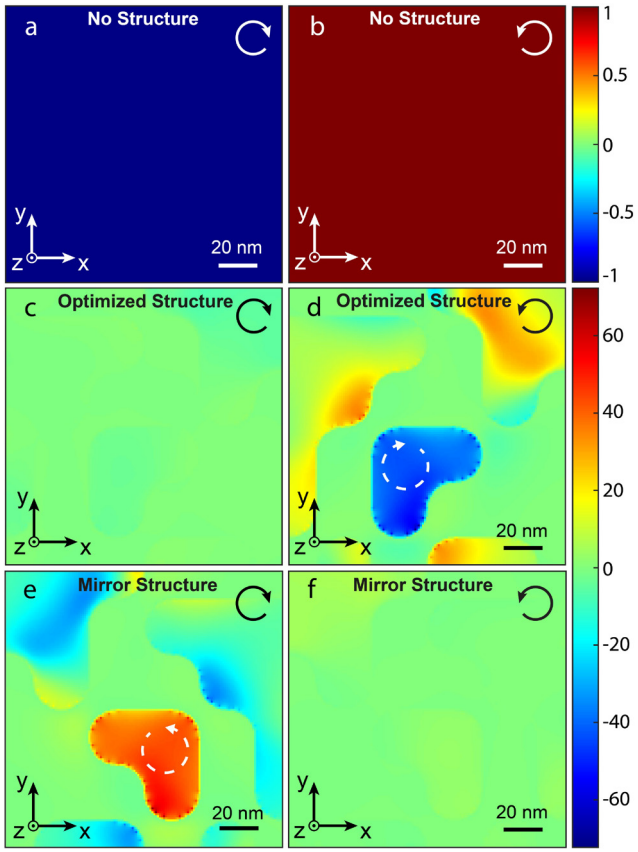

Figure 5.13 *: Distributions of spin density. a) and b) show the spin density for left and right circularly polarized plane waves, respectively. Panels c) and d) show the local spin density in the Z-center of the optimized structure for a left and a right circular polarization of excitation. e) and f) show the local spin density in the Z-center of the mirror structure for excitation by a left and right circularly polarized wave, respectively. The full line white and black arrows indicate the polarization states of incoming light, the white dashed arrows show the direction of local elliptical polarization states.*

In the present case, the capability of our optimized nanostructure to generate a reversed IFE comes from the fact that when the latter is excited by a right circularly polarized plane wave, it generates locally a hot spot of left elliptically polarized spin density (Figure 5.13b and d), thus creating a magnetization opposite to a “classical” inverse Faraday effect (Figure 5.5c and Figure 5.7c).

Moreover, the chirality properties of our nanostructure stem from the fact that for the two excitation polarizations, right and left circular, only one generates a non-zero spin density, the right circular polarization (Figure 5.13c and d). These two behaviors of chirality and manipulation of the local spin density, arise from the constructive and destructive interference of light existing in the optimized nanostructure. Likewise, the mirror structure to the optimized nano-antenna behaves similarly for, this time, a left circular excitation polarization. This mirror structure creates a local hot spot of positive spin density (right elliptical, Figure 5.13e) for excitation by a left circularly polarized wave (negative spin density, Figure 5.13a). Therefore, as the optimized structure, the mirror object creates a non-zero spin density only for one excitation polarization, the left circular polarization (Figure 5.13e and f). From this spin density study, the chiral behavior of these nanostructures, together with the reversed inverse Faraday effect, are thus well explained. Finally, the strong magnetic field generated by these plasmonic structures, considering the low fluence applied (5.3 $\mu J/cm^2$), can be understood by the strong increase of the spin density with a super-circular light [33] up to −70 and 70 depending on the ellipticity (Figure 5.13d and e), which generates strong drift currents. The 3D distributions of spin density are also shown in the Figure 5.4b.

In order to better understand the reversed IFE phenomena with respect to the so-called “classical” IFE, we compare the GA optimized structure with a gold spherical nanoparticle with diameter of 100 nm. The calculations are performed under exact the same excitation conditions for right- and left-circular polarizations. The distributions of stationary magnetic field oriented along Z are shown in the Figure 5.14 below.

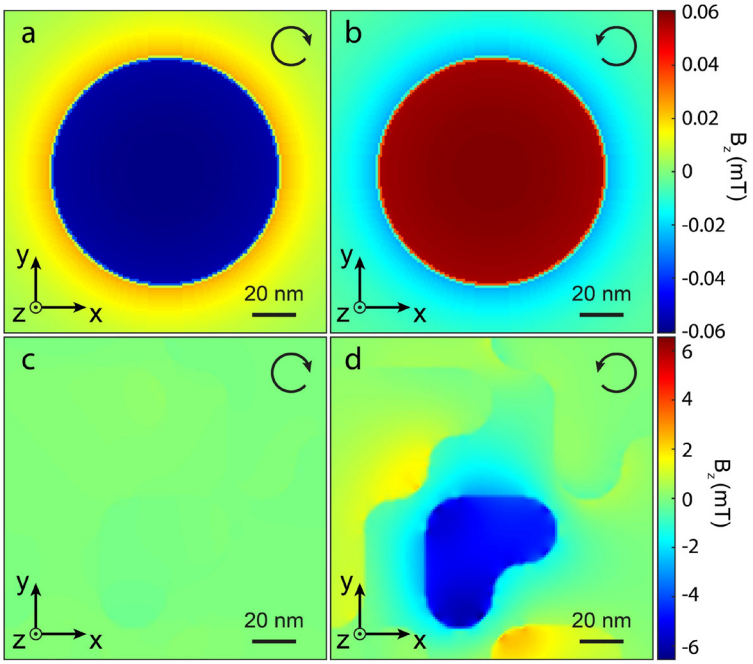

Figure 5.14 *: Stationary magnetic response of the optimized plasmonic nano-antenna and the gold nanosphere. Spatial distribution of the Z-oriented magnetic field generated at the Z-center of a 100 nm nanosphere excited for a) left and b) right circular polarizations. Spatial distribution of the Z-oriented magnetic field generated at the Z-center of the optimized structure excited for c) left and d) right circular polarizations. The black arrows indicate the polarization states of incoming light.*

As one can see, in the case of the gold spherical nanoparticle, for a left-circular polarization (Figure 5.14a), the stationary magnetic field generated by the inverse Faraday effect is negative, and for a right-circular polarization, it is positive with the same size and amplitude (Figure 5.14b).

On the other hand, in the case of the optimized nanostructure, for a right-circular excitation polarization, the stationary magnetic field generated is zero (Figure 5.14c), and for a left-circular excitation polarization, it is maximum, negative, and two orders of magnitude higher in absolute value than that of the spherical nanoparticle. Therefore, it's demonstrated that thanks to the GA optimized structure, we can generate a new process of the reversed inverse Faraday effect, that this phenomenon is chiral, that it is more localized and two orders of magnitude greater in amplitude than in the case of a simple gold spherical nanoparticle described in the ref [22].

5.3 Conclusion

In summary, in this sub-project, we have demonstrated for the first time that the magneto-optical process of the inverse Faraday effect can be a reversed mechanism compared to the so-called “classical” inverse Faraday effect. This new physical behavior results from manipulating the polarization of light locally at the nanoscale. Using an inverse design algorithm (i.e., genetic algorithm) based on natural selection with topology optimization technique same as the one in the chapter 4, we successfully demonstrated the generation of a local elliptical polarization whose helicity was opposite to the circular polarization of excitation incident on the sub-wavelength nanostructure, generating, in turn, this reversed inverse Faraday effect.

Also, we demonstrated that this optimized nanostructure exhibited chirality properties, generating stationary magnetic fields only for one helicity of the incoming light, thanks again to manipulating its polarization locally at the nanoscale. Indeed, the genetic algorithm optimization of this nanostructure selected it to generate a non-zero spin density only for one helicity of the incoming light, the mirror structure generating a magnetization for the opposite handedness. Finally, thanks to the super-circular light created by these nanostructures, a concept which is similar to super-chiral light, which describes an elliptical polarization of light where the optical electric fields are strongly enhanced, the generated $\boldsymbol{B}$-field has an amplitude of 6 mT. This stationary magnetic field is one of the most intense created at these scales and by the inverse Faraday effect, given the low fluence of 53 $\mu J/cm^2$ exciting the optimized nanostructures.

Chapter 6 Femtosecond drift photocurrents

6.1 Introduction

Photocurrents play a crucial role in various applications, including light detection, photovoltaics, and THz radiation generation [90]. Despite the abundance of methods and materials for converting light into electrical signals, the use of metals in this context has been relatively limited. Nanostructures supporting surface plasmons in metals offer precise light manipulation and induce light-driven electron motion. In this chapter, through inverse design optimization of gold nano-antennas, we demonstrate enhanced volumetric, unidirectional, intense, and ultrafast drift photocurrents via a magneto-optical process derived from the inverse Faraday effect described in the chapter 2. This is achieved through fine-tuning the amplitude, polarization, and their gradients in the local light fields. The virtually instantaneous process allows dynamic photocurrent modulation by varying optical pulse duration, potentially yielding nano-sources of intense, ultrafast, planar magnetic fields, and frequency-tunable THz emission. These findings open avenues for ultrafast magnetic material manipulation and holds promise for nanoscale THz spectroscopy.

6.2 Inversely designed Nano-antenna

6.2.1 Introduction

A photocurrent is the flow of electric charges generated when photons are absorbed by a material. This phenomenon plays a critical role in various groundbreaking fields like light detection, solar photovoltaics, lightwave electronics, and THz spectroscopy and imaging [90].

For physicists, a direct photocurrent holds significant importance as it serves as a unique tool to investigate various processes across a wide range of spatial and temporal scales, ranging from femtoseconds to milliseconds and from the mesoscale to the microscale. Hence, understanding photocurrent is crucial to unveil physical and chemical effects due to the intimate connection between photons and electrons. Photocurrents have been instrumental in advancing the development of low-dimensional structures [91], topological materials [92], and the exploration of systems exhibiting symmetry breaking [93, 94]. Their often-ultrafast dynamics contribute to understand out-of-equilibrium transient states [95, 96].

Broadly speaking, the conversion of light into an electrical signal can result from various phenomena. Some, like the p-n junction, are commonly found in everyday technologies, while others, such as current generated by photothermal gradients, are less explored in the literature. There are fascinating prospects involving photo-induced transport of charge carriers in metals. Examples include optical rectification of visible photons through plasmonic nanoscale rectennas [97-99] or the generation of photocurrents by structured light with variations in intensity, phase, and polarization [100]. What makes metals and plasmonics particularly appealing is their ability to fine-tune local optical fields while simultaneously generating electric currents on the same material platform, thereby eliminating the need for complex hetero integration of materials.

Despite recent efforts to understand the interplay of phenomena in these systems [101, 102] including the experiment described in the sub-section 6.3, a comprehensive theoretically framework for manipulating direct photocurrents using plasmonics at the nanoscale is still largely missing. A strategy to engineer their spatial distribution, control their strength, and dictate their direction remains to be rigorously formulated theoretically, optimized through numerical simulations, and verified experimentally. There are physical processes that has been generally overlooked for photocurrent generation: the effect of nonlinear forces. A ponderomotive force is an example of such processes enabling drift currents in the skin depth of a metal parallel to its surface. These drift currents have many advantages: they are relatively simple to model, their generation is almost instantaneous, and they last only as long as the light exposure, so they can be very short when generated by an optical pulse. Moreover, they can be manipulated at will by tuning the intensity of the optical field, its polarization, or its gradients.

Drift currents describe in the chapter 2 can be regarded as a type of optical rectification at the origin of the inverse Faraday effect in metals. Particularly, it was shown that the inverse Faraday effect can be generated by a linear polarization [33] shown in the chapter 2 and the sub-section 6.3, that it can be chiral [103, 104] described in the chapter 4 and 5, or even have its symmetry reversed [103] illustrated in the chapter 5.

In this sub-project, our study builds upon these findings. We demonstrate that a plasmonic nano-antenna specifically inversely designed using genetic algorithm based on topology optimization manipulates light fields at the nanoscale in such a way that a volumetric, unidirectional, intense, and ultra-short photocurrent emerges. Moreover, we also demonstrate that this phenomenon is chiral, i.e., occurring for only one circular polarization state of

incoming light and that it can generate a stationary magnetic field perpendicular to the direction of incident light propagation, which was thought to be impossible with the conventional inverse Faraday effect. Finally, by generating ultra-short, planar, and unidirectional photocurrents, we show that this physical process opens the way to generate a linearly polarized and frequency-tunable THz nano source.

6.2.2 Results and discussions

In the inverse Faraday effect, it is conventionally understood that drift currents have an azimuthal symmetry generating a static magnetization perpendicular to the plane in which the electrons spin. However, as recognized by the plasma community, the nonlinear forces that light applies to the electron sea possess all kinds of symmetries. For instance, ponderomotive forces accelerating charges in a plasma hold radial symmetries [28, 105].

Based on this concept, we inversely designed a complex plasmonic nanostructure, capable of generating a direct drift photocurrent that is intense, unidirectional in the plane of the nano-object, independent of the excitation polarization, and ultrafast. The origin of these exceptional properties can be found in the Equation 5. As shown in this expression, the drift currents can only be created when the product $\left(\nabla \cdot \boldsymbol{E}\right) \cdot \boldsymbol{E}^{*}$ is not zero, i.e., for an elliptical polarization or a circular polarization state of the incoming light. Therefore, manipulating the local polarization state of the light with an adequate design enables to create different ellipticities around the nano-object and a control of the drift currents.

Specifically, in this sub-project, we have inverse-designed a plasmonic nano-antenna in a 30 nm thick gold layer deposited on a glass substrate using a genetic algorithm based on topological optimization shown in Figure 6.1 below.

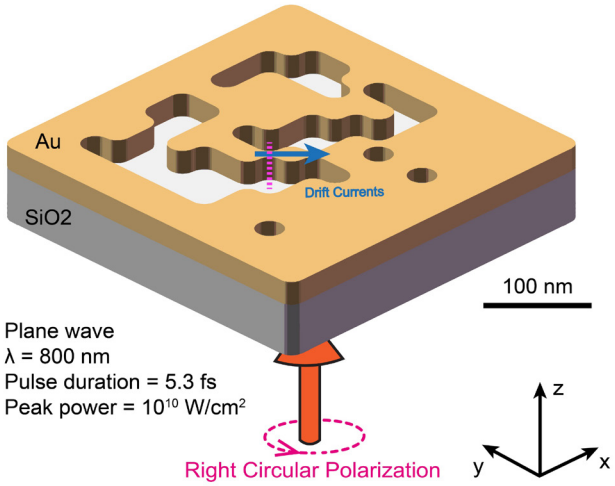

Figure 6.1 *: Optimized structure and excitation conditions. Example of a GA-optimized structure, made in a 30 nm thick gold layer. The 280*280 nm² nanostructure is based on a two-dimensional array of 10*10 elements, each element consisting of metal or air with a size of 28 nm. These dimensions are chosen to facilitate the fabrication of this structure by e.g. nanoscale lithography techniques. For the same reason and to avoid non-physical effects that a numerical approach can generate locally, the corners of the nanostructure are rounded (see Figure 3.4 of the chapter 3). The optical excitation of the nanostructure is modeled by a pulsed plane wave emitted at a wavelength of 800 nm. The pulse is launched from the substrate side and is right circularly polarized. We set the pulse duration at 5.3 fs and the peak power of 10^{10} W/cm², a value same as before which is well below the damage threshold of the material. The blue arrow represents the ultrafast direct currents flowing in a single direction, and the pink dashed line indicates the position of a cross-section.*

In order to generate a strong unidirectional drift current in the plane of the metal layer, the GA optimization objective function consisted in maximizing the local stationary magnetic fields created by the drift currents at the center of the structure and having a vectorial symmetry parallel to the gold surface. The evolutionary history of the nanostructures in connection with the generation of a strong magnetic field by the inverse Faraday effect is shown in Figure 6.2 below.

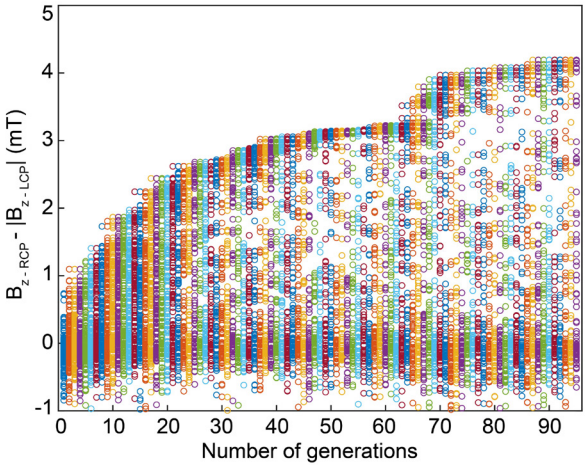

Figure 6.2 *: Evolutionary process. Evolution during the different generations of the optimization function that maximizes the difference* $\boldsymbol{B}_{z-RCP} - |\boldsymbol{B}_{z-LCP}|$*, with* $\boldsymbol{B}_{z-RCP}$ *and* $\boldsymbol{B}_{z-LCP}$ *being the Z-oriented stationary magnetic fields* ***B*** *created by a right or left circular polarization, respectively. Each generation consists of 200 elements. The optimized structure appears after 87 generations.*

As can be seen, after 87 generations the strength of the stationary magnetic field reaches a plateau, and the nanostructure is considered optimized. The Figure 6.3a represents schematically the result of the GA optimization procedure.

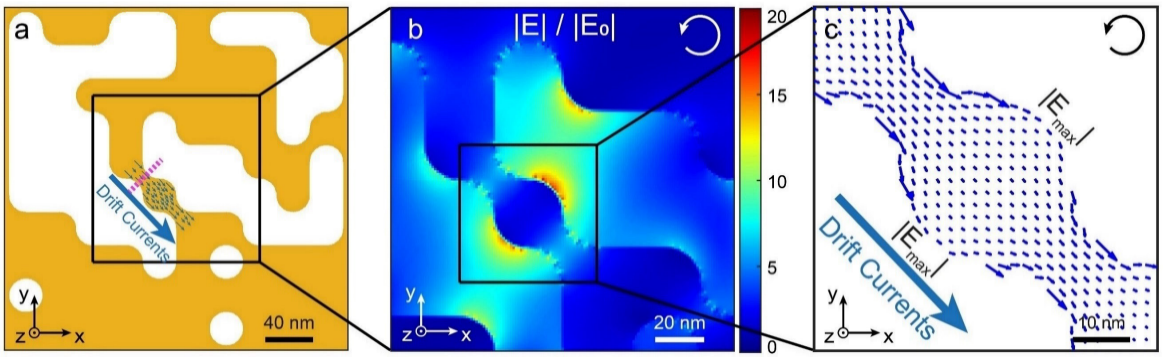

Figure 6.3 *: Optical response of the optimized plasmonic nanostructure and associated drift currents. a) Schematic, in an XY plane, of the GA-optimized structure. b) Spatial distribution of the electric field enhancement at the Z-center of the structure shown in a) for a right circular polarization of excitation. c) Spatial distribution of the drift currents generated at the surface of the structure by the electric field distribution shown in b). The white and black arrows indicate the polarization states of incoming light, the length of the dark blue arrows in c) refers to the relative amplitude of the drift currents.*

The interesting part of the nanostructure is certainly the bridge-like geometry at the center within the black square area in the Figure 6.3a and b. Figure 6.3b shows the distribution and

the increase of the optical electric field at the origin of the drift currents and ***B*** field in the center of this design (represented by a black square in Figure 6.3a) in an XY plane taken at the middle of the metal thickness. From this electric field enhancement distribution and using the Equation 5, we can then plot the distribution of drift currents in the nanostructure as shown in Figure 6.3c. Firstly, drift currents are maximal in a gold strip in the center of the structure but not necessarily where the electric field and field are the strongest. Importantly, the arrows representing the direction of drift currents are all oriented in the same direction in the XY plane, demonstrating the possibility of generating, in a controlled manner, straight and unidirectional DC currents by optical excitation only. It should be also noted that other physical processes may be responsible for generating DC currents, one of which is related to thermal effects, for instance. Although the message of this sub-project is not to compare all these processes, a study of temperature generation in our optimized nano-system for our optical excitation characteristics is described below based on the two-temperature model [106] in collaboration with Jean-François Bryche's group at university of Sherbrook in Canada. As described in the Figure 6.4, the lattice temperature remains extremely modest which is much lower than the melting point of gold material. Furthermore, it is rather homogenous in the gold strip at the center of the nanostructure, implying a very minimal contribution of this physical process to DC current generation.

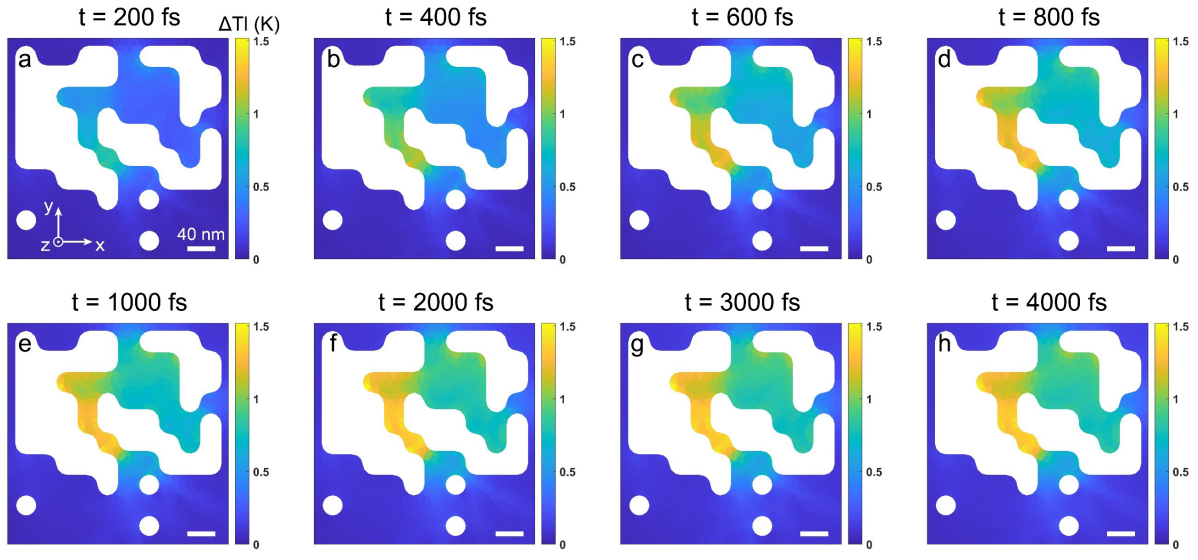

Figure 6.4 *: Spatial distribution of lattice temperature generation in an XY plane at the Z center of the optimized nanostructure for different characteristic times after the optical pulse, a) 200 fs, b) 400 fs, c) 600 fs, d) 800 fs, e) 1000 fs, f) 2000 fs, g) 3000 fs, h) 4000 fs.*

In addition to that, the electronic temperature distribution at an XY plane in the surface of the nanostructure are also relatively low, shown in Figure 6.5 below, for the optical peak powers and pulse durations of incident wave considered here. Thus, the thermal effects generated by the GA-optimized nanostructure under circular polarization of excitations in this study can be fully neglected.

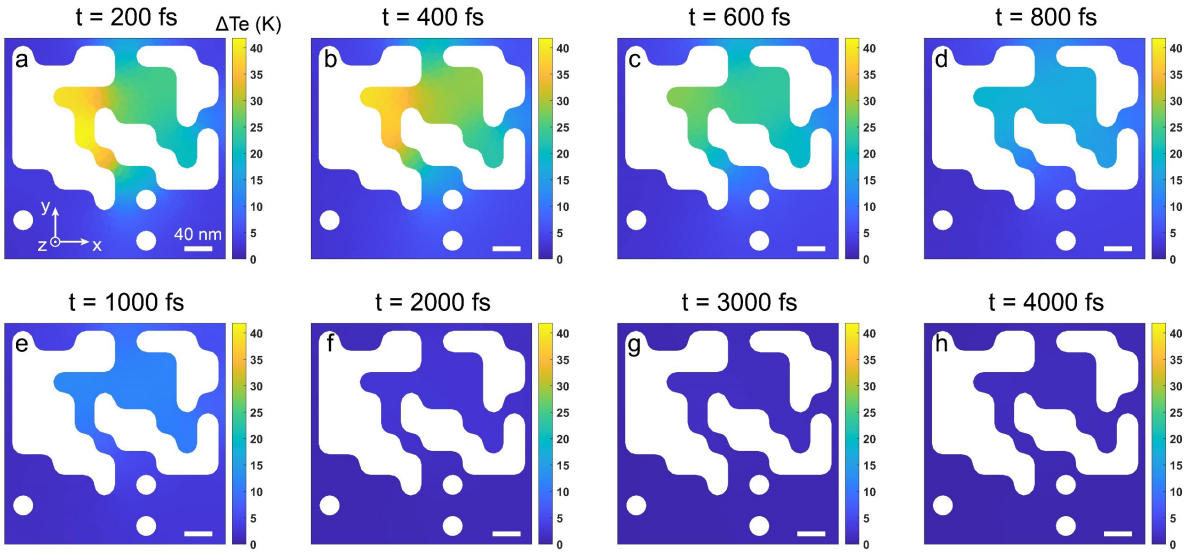

Figure 6.5 *: Spatial distribution of electronic temperature generation in an XY plane at the Z center of the optimized nanostructure for different characteristic times after the optical pulse, a) 200 fs, b) 400 fs, c) 600 fs, d) 800 fs, e) 1000 fs, f) 2000 fs, g) 3000 fs, h) 4000 fs.*

Note that the dynamics of these temperatures do not change with increasing optical pulse duration, as shown in Figure 6.6.

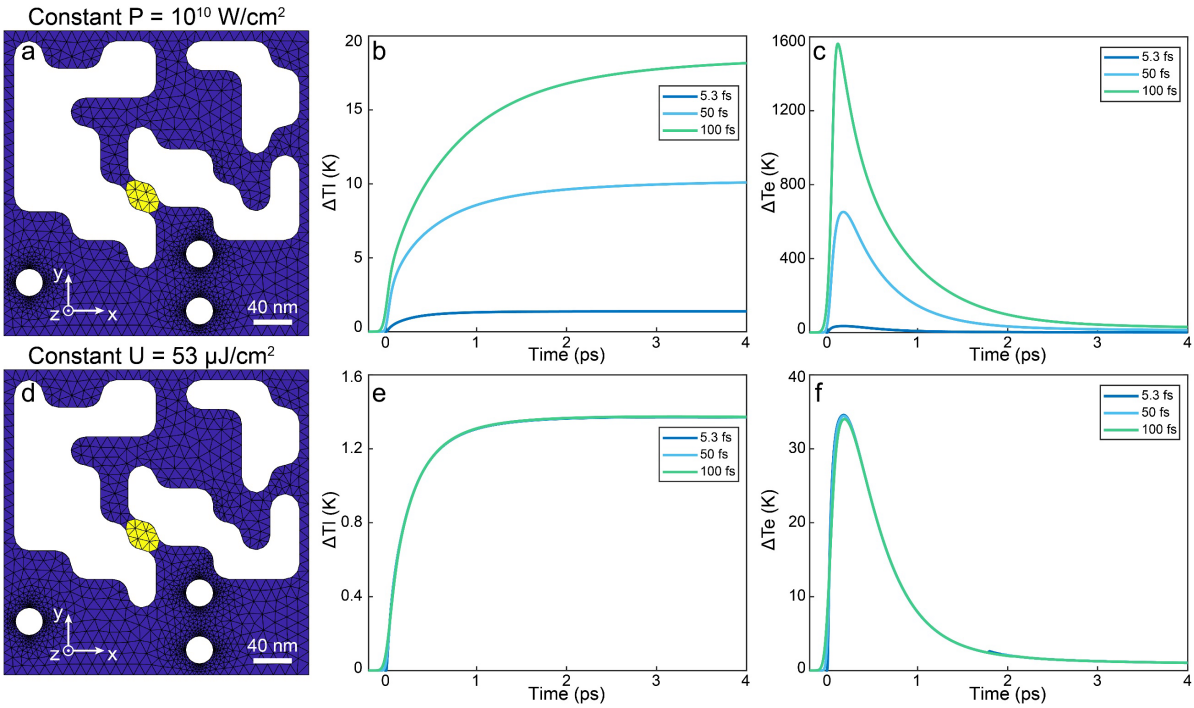

Figure 6.6 *: Time evolution of lattice and electronic temperatures for different optical pulse durations, for a) to c) the same peak power and d) to f) the same energy. a) Schematic of the optimized structure with the yellow section indicating the area of temperature analysis. Time evolution of b) lattice temperatures and c) electronic temperatures for pulses of 5.3, 50, and 100 fs at a peak power of 10^{10} W/cm², showing similar dynamics. d) Schematic of the optimized structure, with the yellow area denoting the temperature study region. Time evolution of e) lattice and f) electronic temperatures for pulses of durations 5.3, 50, and 100 fs, each with an energy of 53 μJ/cm², displaying identical dynamics.*

Conversely, at constant peak power, both lattice and electronic temperatures increase linearly in the studied range with pulse duration, while they remain constant for constant pulse energy, as illustrated in Figure 6.7.

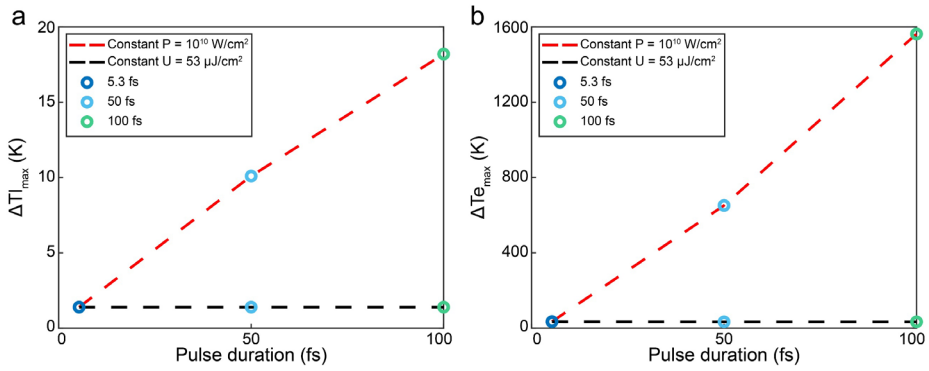

Figure 6.7 *: Evolution of maximum lattice and electronic temperatures based on the characteristics of the optical pulses used. a) Evolution of lattice temperatures for pulse*

durations of 5.3, 50, and 100 fs (represented by colored circles), analyzed under conditions of constant peak power (red dashed line) or constant pulse energy (black dashed line). It is observed that the lattice temperature increases linearly in the studied range with constant peak powers, while remaining steady for constant pulse energies. b) Evolution of electronic temperatures for the same pulse durations (using the same color codes). The results are consistent: electronic temperatures rise linearly in the studied range when the peak power is constant and remain unchanged with constant energy levels.

One way to visualize the vectorial orientation of the DC currents in the metal is to image the resulting vectorial distribution of the stationary magnetic field ***B***. For this purpose, Figure 6.8 represents the distribution of the magnetic field created by IFE in the same plane as Figure 6.3b, c. In particular, Figure 6.8a and b displays respectively the amplitude of the total ***B***-field and the ***B***-field component oriented along Z. Figure 6.8c shows the vectorial distribution in the y'z cross-sectional plane of the metal junction, indicated by a pink line in Figure 6.8a. This distribution of the magnetic field components around the thin gold strip is therefore characteristic of a current flowing unidirectionally in the direction shown by the arrow in Figure 6.3c.

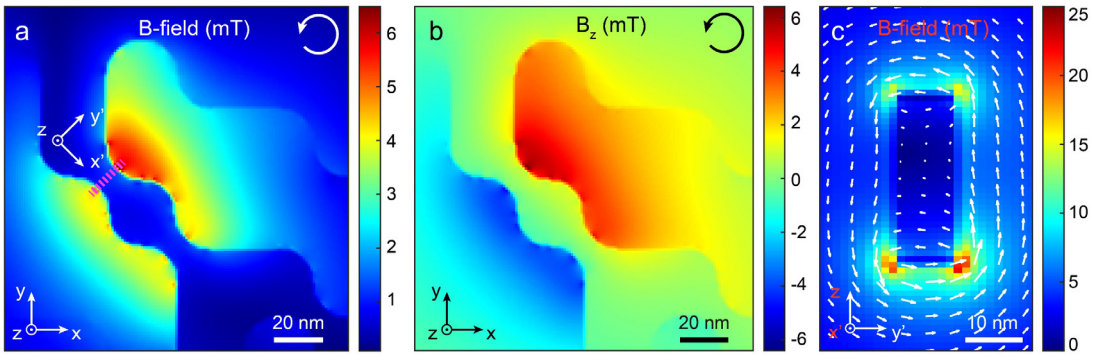

Figure 6.8 *: Magnetic response of the optimized plasmonic nanostructure under a right circular polarization of excitation. a) Spatial distribution of the amplitude of the total magnetic field generated at the Z-center of the structure represented in Figure 6.3a. b) Z-component of the spatial distribution of the magnetic field in a). c) Vectorial distribution in a cross-section plane (y'z) of the metal junction symbolized by the pink line in a). The white and black arrows in a) and b) indicate the polarization states of incoming light, the white arrows in c) represent the orientation of the* ***B*** *field and the colors its amplitude.*

Additionally, the optical electric field enhancement and drift currents at the cross section of the GA-optimized structure under a right circular polarization of excitation, which is symbolized by the dashed pink line in the Figure 6.1 and Figure 6.8a, are shown in Figure 6.9 below. Moreover, we note that in past studies, the orientation of the stationary magnetic fields

generated by optical rectification through the inverse Faraday effect have all been collinear with the direction of incoming light propagation [23, 24, 32].

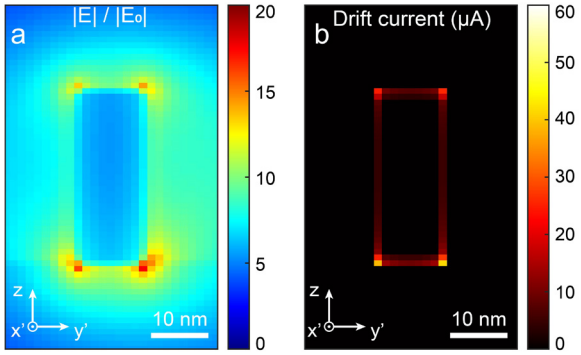

Figure 6.9 *: Spatial distribution of the electric field enhancement in a Y'Z plane of the X'Y'Z coordinate, symbolized by the pink dotted line and shown in Figure 6.8a. Distribution b) of the drift currents described by the Equation 5 in the same plane as a).*

Here, in this sub-project, by manipulating the light at the nanoscale, we demonstrate the creation of an azimuthally polarized stationary magnetic fields around the gold nanostrip (Figure 6.8b, c). This allows for generating a stationary magnetic field above the gold layer parallel to the nanostructure's surface, and thus perpendicular to the direction of incident light propagation. This result has significant implications for applying the inverse Faraday effect to manipulate magnetic processes at the nanoscales [61] and potentially ultrafast scales [107, 108] since many magnetic layers have domains orientation parallel to the sample plane (i.e., XY here).

To further understand why this plasmonic nanostructure creates a unidirectional DC current, we plot in Figure 6.10a below the distribution of the Z-oriented component of the optical spin density in the same plane as Figure 6.3c, which is a parameter related to light polarization state as described in previous chapter (Equation 8). Now, drift currents can emerge in the presence of an elliptical polarization state of light. From Equation 5, a left elliptical polarization state of light creates a drift current in one direction, while a right elliptical polarization state of light generates drift currents in the opposite direction.

With this understanding, the spin density distribution shown in Figure 6.10a sheds light on the vectorial distribution of DC currents shown in Figure 6.3c. On each side of the gold strip, where the currents are the strongest, we concomitantly observe the strongest spin densities of

opposite signs. By symmetry, the generated drift currents are flowing in the same single direction and are oriented in the same way as the red and blue arrows representing the local helicity of the light. These hot spots of so-called super circular light, a concept which is similar to super chiral light related to elliptical polarization of enhanced optical fields [109], are thus at the origin of the strong currents and their straight and unidirectional orientation. The spin density distribution inducing this physical effect is the result of constructive and destructive interferences of the light in the plasmonic nanostructure, interferences that the evolutionary approach of the GA has selected during the optimization process.

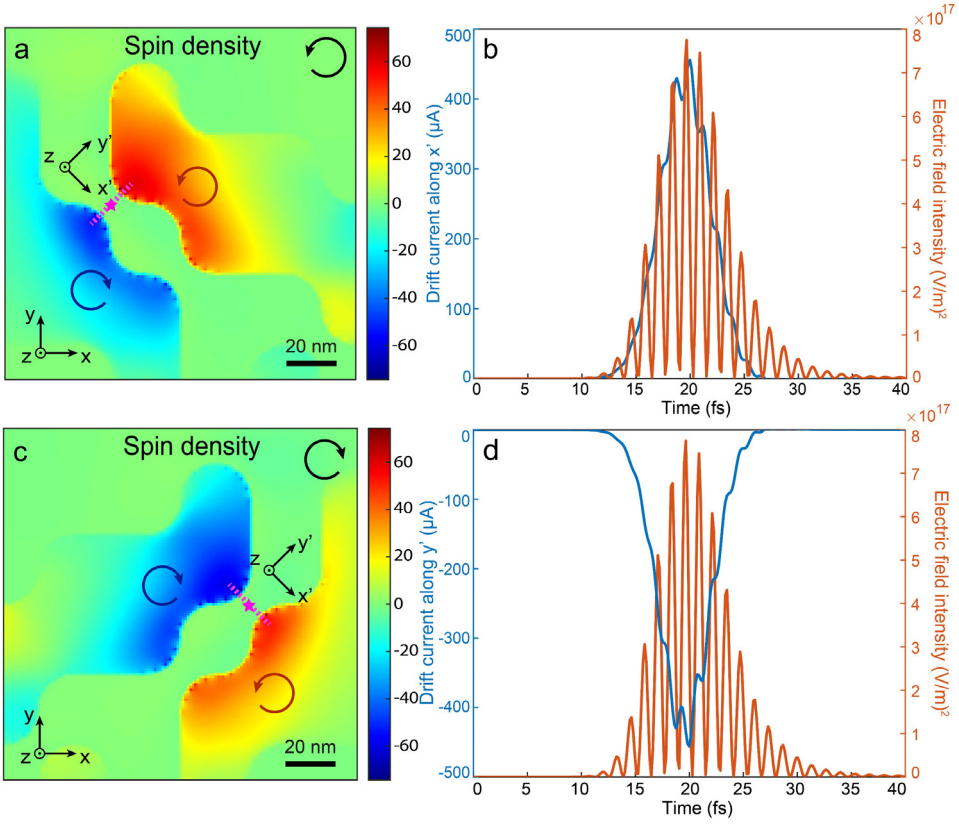

Figure 6.10 *: Spin density distribution and temporal responses. a) Local spin density at the Z-center of the optimized plasmonic nanostructure shown in Figure 6.3a for a right circular polarized excitation. b) Temporal response of the drift currents flowing along X' through the section shown in a) as a dashed line and the electric field intensity at the pink star point shown in a). c) Spatial distribution of the spin density in the same plane and for the mirror structure shown in a) excited by a left circular polarization. d) Temporal response of the drift currents and the electric field intensity, respectively, through the section symbolized by a dotted line and the pink star shown in c). The black arrows indicate the polarization states of incoming light, the blue and red arrows show the direction of local elliptical polarization states.*

Because the nanostructure is excited by an ultrashort optical pulse, we anticipate that the resulting DC current also carry an ultrafast dynamic feature. Figure 6.10b confirms this hypothesis. This Figure 6.10 above represents the instantaneous intensity of the electric field as a function of time at a point on the surface of the structure, symbolized by a pink star in Figure 6.10a and for an optical pulse of 5.3 fs. In the same figure is shown the total drift current generated by this pulse and passing through a cross section of the gold strip represented by the pink dotted line in the Figure 6.10a (Y'Z section in the X'Y'Z coordinate system rotated from the XYZ coordinate system by an angle 45-degree around Z, as shown in the Figure 6.10a). Clearly, an ultrashort photocurrent transient emerges across the section of the gold strip and reaches up to 400 µA with the optical power used in the calculation. The duration of this transient is directly related to the duration of the optical pulse, since when there is no more energy to set the electrons in motion, they slow down immediately. Interestingly, this decay time can be observed in the tiny oscillations of the drift current, which occur when the instantaneous energy in the plasmonic nanostructure is 0 considering a phase shift.

To further demonstrate the potentiality of controlling IFE-induced drift currents at the nanoscale, an additional optimization condition was included in the definition of this nanostructure, consisting in making the inverse Faraday effect chiral. During the selection process by the GA, the nanostructures were selected to generate a stationary magnetic field only for one helicity of the incoming light, i.e., the right circular polarization state of light. Therefore, when a left circular polarization state of light illuminates the nanostructure, the drift currents and the associated stationary magnetic field are nearly zero. The electric field enhancement and drift currents distribution at an XY plane of the optimized nanostructure under a left circular polarization of excitation are shown in Figure 6.11.

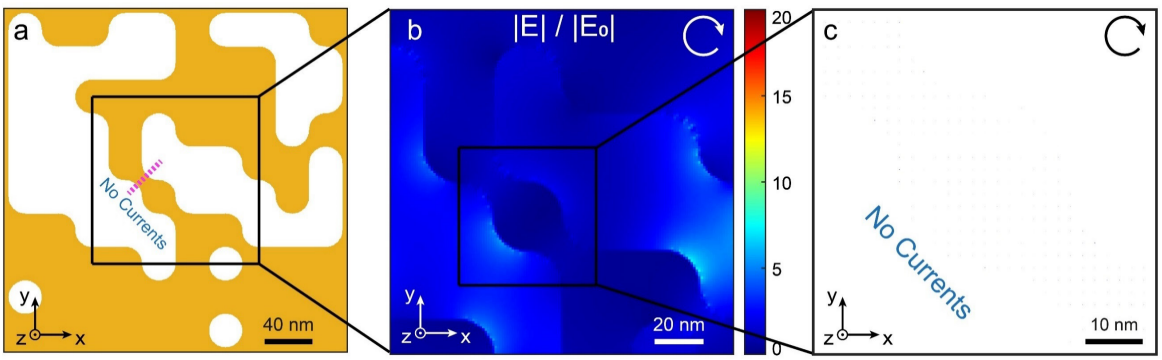

Figure 6.11 *: Optical response of the optimized plasmonic nanostructure and associated drift currents for excitation by a left circular polarization. a) Schematic, in an XY plane, of the GA-optimized structure. b) Spatial distribution of the electric field enhancement at the Z-center of*

the structure shown in a) for an excitation by a left circular polarization. c) Spatial distribution of the drift currents generated (or rather not generated) by the electric field distribution shown in b). The white and black arrows indicate the polarization states of incoming light.

Furthermore, the stationary magnetic field distributions of the GA-optimized structure under a left circular polarization of excitation including total field and its X, Y and Z component are shown below in Figure 6.12.

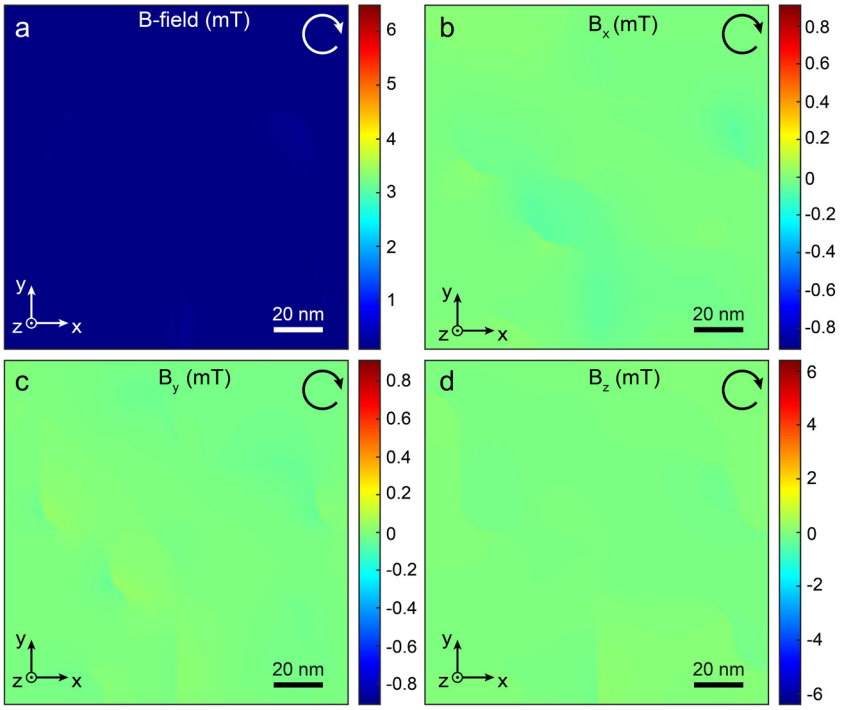

Figure 6.12 *: Magnetic response of the optimized plasmonic nanostructure under left circular polarized excitation. Spatial distribution of the a) total stationary magnetic field and its different components along b) X, c) Y and d) Z, generated (or rather not generated) at the Z-center of the structure shown in the Figure 6.3a. The white and black arrows indicate the polarization states of incoming light.*

Reciprocally, the mirror nanostructure of Figure 6.3a can generate a symmetric spin density only when excited by a left circular polarization (Figure 6.10c) which results in an ultrafast direct current of perpendicular direction in the X'Y'Z coordinate system (Figure 6.10d and Figure 6.13c). The electric field enhancement and drift currents of the mirror nanostructure under a left circular polarization of excitation are shown Figure 6.13.

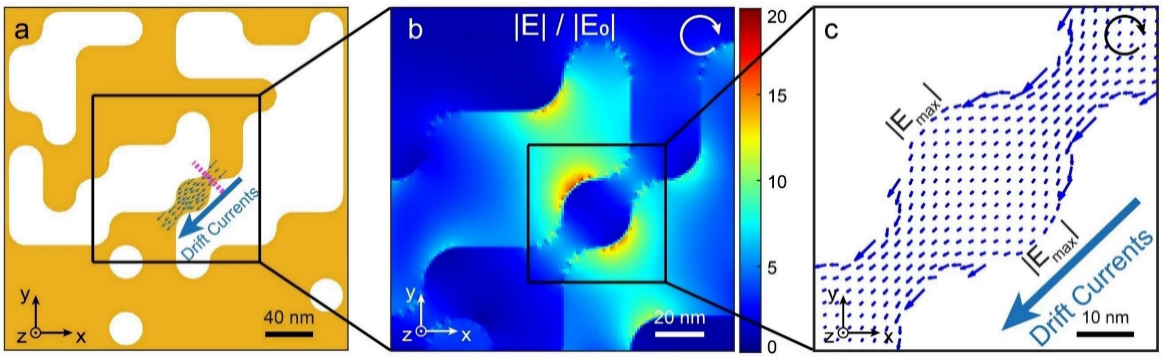

Figure 6.13 *: Optical response of the mirror plasmonic structure. a) Schematic representation of the GA-optimized mirror nano-antenna. b) Electric field enhancement at the Z-center of the mirror structure in the area enclosed by a black square in a). c) Drift currents created by the electric field distribution described in b) via the Equation 5 at the surface of the structure. The white and black arrows indicate the polarization states of incoming light, the length of the dark blue arrows in c) represents the relative amplitude of drift currents.*

Moreover, the stationary magnetic field distributions of the mirror nanostructure (Figure 6.13a) under a left circular polarization of excitation including total field and its X, Y and Z component are shown below in Figure 6.14.

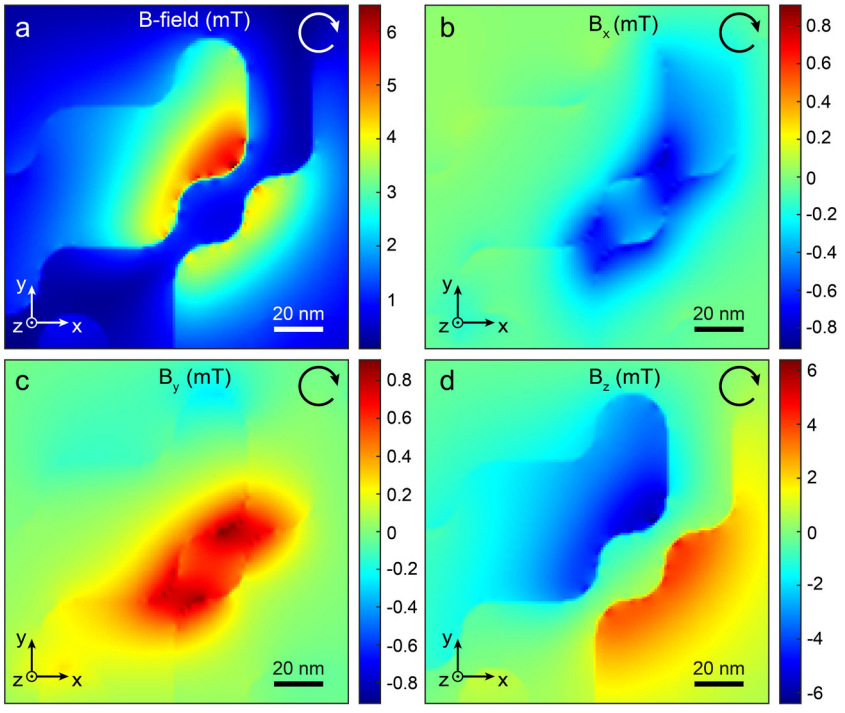

Figure 6.14 *: Magnetic response of the mirror plasmonic nanostructure under a left circular polarization of excitation. a) Spatial distribution of the amplitude of the total stationary magnetic field generated at the Z-center of the structure represented in Figure 6.13a. Decomposition of the spatial distribution of the stationary magnetic field a) into the components*

oriented along b) X, c) Y, and d) Z. The white and black arrows indicate the polarization states of incoming light.

In addition, the electric field enhancement, drift currents and stationary magnetic fields at the cross section of the mirror nanostructure under a left circular polarization of excitation, which is symbolized by the dashed pink line in the Figure 6.10c and Figure 6.13a, are shown in Figure 6.15 below.

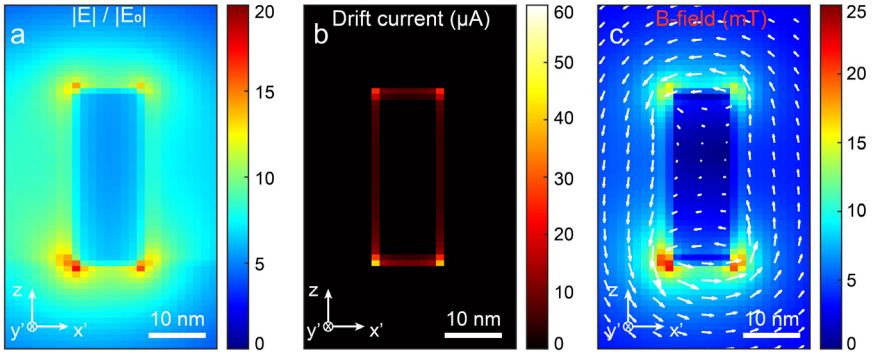

Figure 6.15 *: Spatial distribution of the electric field enhancement in a Y'Z plane of the X'Y'Z coordinate, symbolized by the pink dotted line and shown in Figure 6.13a. Distribution b) of the drift currents described by the Equation 5 and c) of the resulting stationary magnetic field in the same plane as a).*

These results, which show a chirality, are remarkable since this nanostructured landscape enables generating an ultrashort unidirectional current pulse even for a unpolarized excitation. Due to its chirality property, the GA-optimized nanostructure naturally filters the polarizations from the unpolarized incoming fields producing the direct current (principle of chirality and see Figure 6.16-18 for elliptical and linear polarizations of excitation). Therefore, through our optimization approach, we inversely design plasmonic nanostructures generating ultrafast drift photocurrents in one direction for a specific excitation polarization state of incoming light (i.e., RCP) and in another direction for another polarization condition (i.e., LCP).

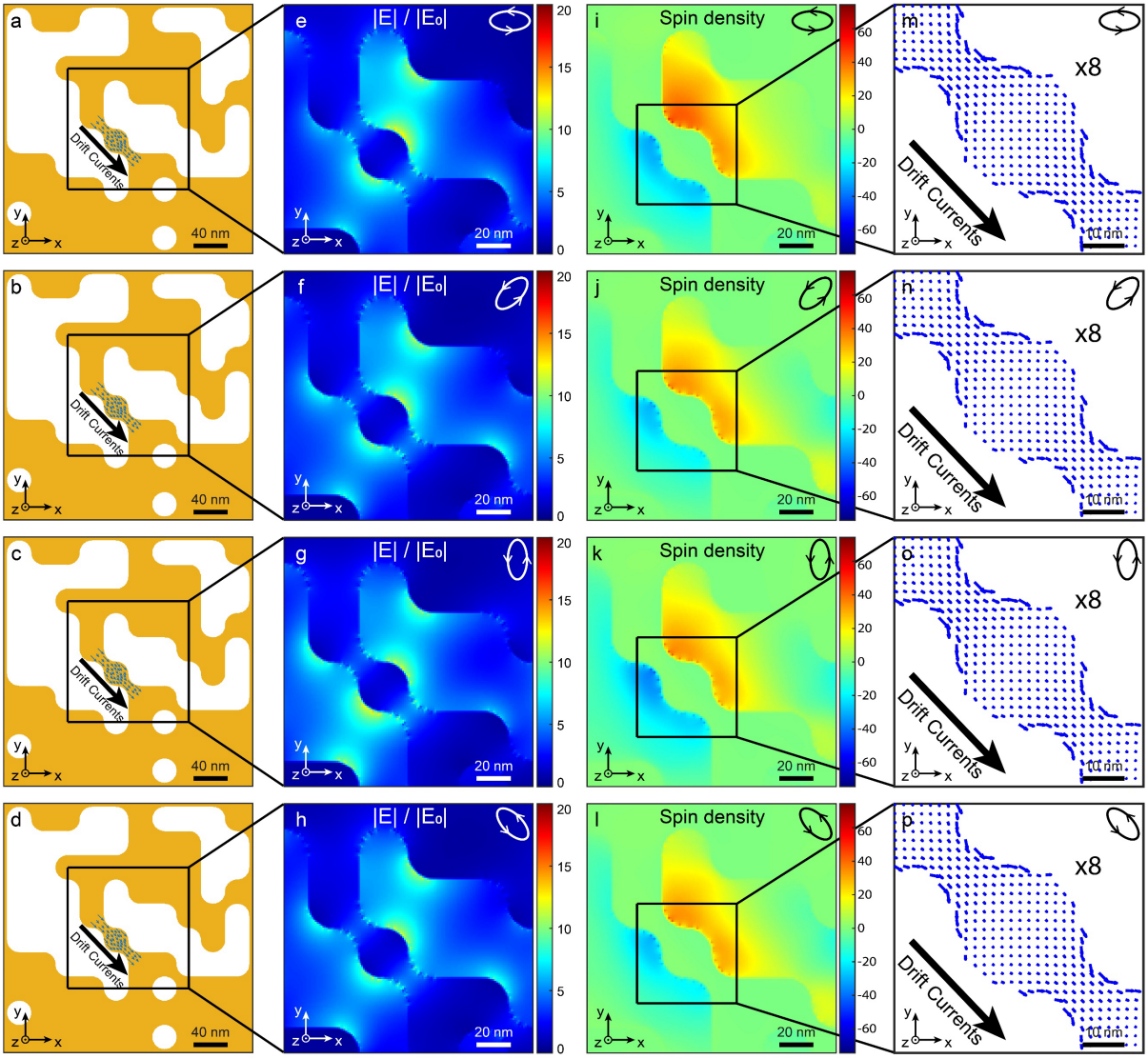

Figure 6.16 *: Optical response of the optimized plasmonic nanostructure and associated drift currents for right elliptical polarizations. a-d) Schematic representation in the XY plane of the GA-optimized structure. e-h) Spatial distribution of electric field enhancement at the Z-center of the structure for right elliptical polarizations at orientations of 0°, 45°, 90°, and 135° with π/8 ellipticity. i-l) Corresponding spatial distributions of spin density at the Z-center of the structure. m-p) Spatial distributions of drift currents generated on the structure's surface due to the electric field and spin density distributions depicted in e-h). The length of the blue arrows in m-p) indicates the relative amplitude of the drift currents (multiplied by 8 with respect to the Figure 6.3c) and the ellipses in the top right of e-p) denote the polarization states of the incoming light.*

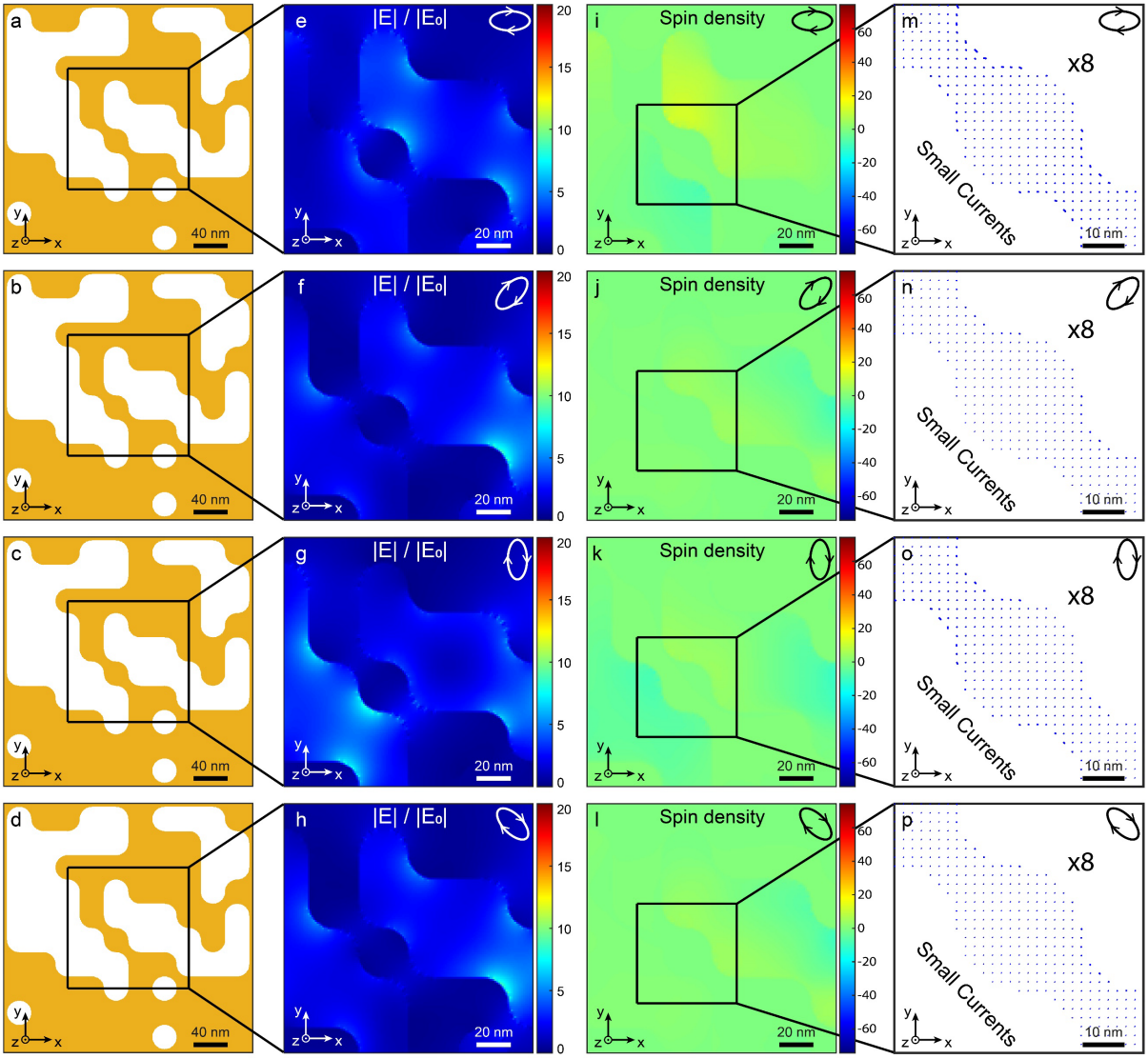

Figure 6.17 *: Optical response of the optimized plasmonic nanostructure and associated drift currents for left elliptical polarizations. a-d) Schematic representation in the XY plane of the GA-optimized structure. e-h) Spatial distribution of electric field enhancement at the Z-center of the structure for left elliptical polarizations at orientations of 0°, 45°, 90°, and 135° with π/8 ellipticity. i-l) Corresponding spatial distributions of spin density at the Z-center of the structure. m-p) Spatial distributions of drift currents generated on the structure's surface due to the electric field and spin density distributions depicted in e-h). The length of the blue arrows in m-p) indicates the relative amplitude of the drift currents (multiplied by 8 with respect to the Figure 6.3c) and the ellipses in the top right of e-p) denote the polarization states of the incoming light.*

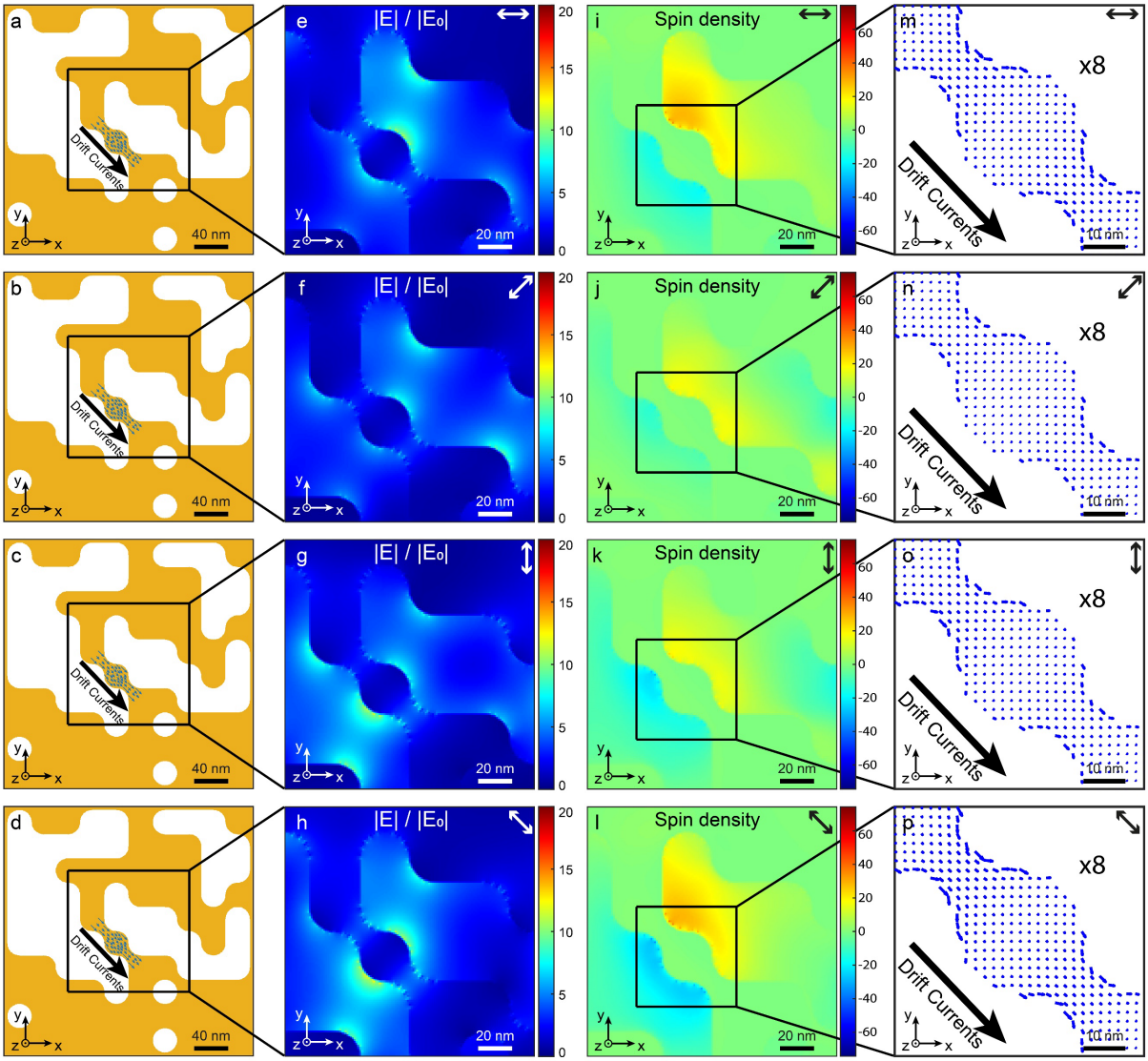

Figure 6.18 *: Optical response and associated drift currents in a GA-optimized plasmonic nanostructure for linear polarizations. a-d) Schematic representation of the structure in an XY plane. e-h) Spatial distribution of electric field enhancement at the Z-center of the structure for linear polarizations at 0°, 45°, 90°, and 135° orientations. i-l) Corresponding spatial distributions of spin density at the Z-center of the structure. m-p) Spatial distributions of drift currents generated on the surface of the structure by the preceding electric field and spin density distributions. The length of the blue arrows in m-p) indicates the relative amplitude of the drift currents (multiplied by 8 with respect to the Figure 6.3c), and the double-ended arrows in the top right of e-p) show the polarization states of the incoming light.*

Based on these findings and drawing inspiration from the potential applications of ultrafast photocurrents for THz generation, we assess the suitability of the transient drift currents to act as a tunable THz nano source. To achieve this, we excite the nanostructure depicted in Figure 6.3a with femtosecond (fs) pulses of varying durations and observe temporal responses of drift photocurrents. Our numerical simulation results are displayed in Figure 6.19a.

Because of the ultrafast current dynamics already highlighted above (see Figure 6.10), an increase of the pulse duration leads to a longer current transient. More importantly, since the peak power of the optical pulses is kept identical, differences in photocurrent intensity are primarily attributed to the more effective power build-up of the nanostructure at longer pulses.

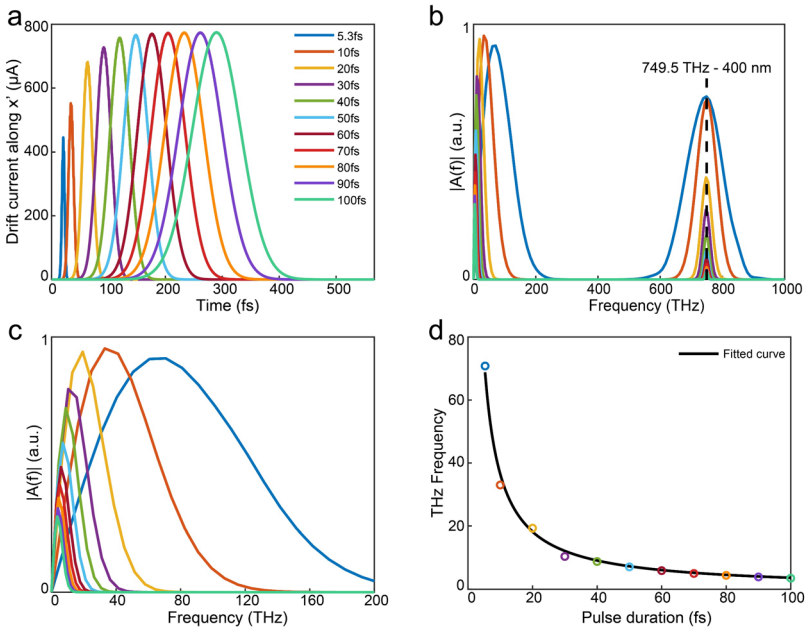

Figure 6.19 *: Generation of tunable THz radiation. a) Time response of the drift photocurrents as a function of the duration of the light pulse exciting the optimized nanostructure described in Figure 6.3a. b) Fourier transform of the time responses shown in a) over the frequency range from 0 to 1000 THz. c) Fourier transform of the time responses shown in a) over the frequency range from 0 to 200 THz. d) Distribution of the THz frequencies generated as a function of the pulse duration used.*

From the temporal responses calculated in Figure 6.19a, we can extract radiation generated at various frequencies by performing a Fourier transform of the time derivative of the drift currents shown in the Figure 6.19a. Figure 6.19b displays these Fourier transforms. The spectrums reveal two frequency components associated with each photocurrent time response: one at low frequencies and another centered at 749.5 THz. The first component, displayed at higher resolution in Figure 6.19c, is the THz radiation produced by the drift currents impulse. The second component corresponds to the second harmonic generation resulting from the second-order nonlinear process [110] described by the Equation 5.

Subsequently, we plot in Figure 6.19d the peak THz frequencies generated by the GA-optimized nanostructure as a function of optical pulse durations based on the Fourier transforms

described in the Figure 6.19c. As expected, these frequencies exhibit an inverse relationship with pulse lengths, ranging from 70 THz to approximately 4 THz for the selected pulse durations. An appealing feature of drift currents transients produced by the inverse Faraday effect is that they not only create a nanoscale, tunable source of THz radiation but also impart linear polarization to that THz radiation, despite the right circular excitation of the incident wave. This is made possible by the unidirectionality of the photocurrents drifting in the gold plane. Considering the light energy absorbed and scattered by the optimized structure, it is estimated that approximately 63% of the incident energy interacts with it. Additionally, by comparing the amplitudes of the conduction currents to those of the drift currents, the conversion rate between these two types of currents is determined to be approximately 1.8%. Consequently, the ideal maximum THz radiation conversion efficiency is estimated to be slightly over 1%, aligning with the efficiencies reported for other THz sources in the literature [111].

6.2.3 Conclusion

In conclusion, we demonstrate that by manipulating the optical fields and field gradients in a plasmonic nanostructure optimized by an inverse design algorithm, unidirectional and direct photocurrents in the metal plane are generated. This is made possible by influencing the local polarization state of light around the GA-optimized photonic nanostructure. Also, thanks to the ability to assign several optimization objectives to the genetic algorithm, the optimized nanostructure creates a direct photocurrent only for one helicity, here the right circular polarization state of light. This chirality imparted to physical response enables generation of these currents even for the unpolarized light. We then confirm that a direct current of the opposite direction is generated in the mirror structure for a left circular polarization state of light, implying that a control of the current flow is possible only by changing the polarization state of light incident on the structure. Also importantly, we demonstrate that through the inverse Faraday effect, unidirectional current pulses in the plane of the metal are generated at ultrafast timescales. These currents can be harnessed to produce ultrafast stationary magnetic fields with unexpected symmetry, defying conventional expectations associated with the inverse Faraday effect.

In addition, the ultrafast drift photocurrents generated in this way offer the potential for creating a versatile and tunable nano source for a linearly polarized THz radiation. Hence, these

findings pave the way to ultrafast in-plane manipulation of magnetic domains and the possibility of conducting ultra-localized THz spectroscopy at the nanoscale.

6.3 Nanostrip and nanorods

6.3.1 Introduction

In this sub-section, we propose a simpler plasmonic nanostructure for generation of unidirectional currents by the same process producing an IFE, i.e., by the creation of drift currents, thanks to the local manipulation of the light polarization. In a recent publication [33] from our group which has been introduced in the chapter 2, we demonstrated that by exciting a gold nanorod with linear polarization at angles of ±45° relative to the nanorod's longitudinal axis, it is possible to manipulate the local spin density and, consequently, the polarization of light around the rod, thereby inducing drift currents in either direction within the rod. Inspired by this theoretical work and the inverse-designed plasmonic nano-antenna shown in the previous section 6.2, by positioning the nanorod adjacent to a gold strip served as a reflective surface, we hypothesized that a mirror image of the nanorod's effects could be projected onto the gold strip (Figure 6.20). This simple configuration is anticipated to facilitate the generation of drift currents in the gold strip in one direction or the other, upon the change in incident polarization. To be specific, by changing the polarization from 45 degree to 135 degree, the local polarization changes from right circular to left circular. Thus, this local helicity of the light generates drift currents in the gold strip oriented in one direction or the other, depending on the helicity considered.

6.3.2 Schematic and basic optimization

A schematic diagram of the nanostructure generating ultrafast direct currents is given in Figure 6.20. The length of nanorod L, the gap between nanorod and gold strip G, the width of gold strip W_{gold} and the thickness of nanorod as well as gold strip T are four parameters which need to be optimized. The objective function here is to maximize the volumetric average of drift current intensity difference between calculation area up and down in the gold strip. More specifically, for these two 3D currents calculation areas with range 200*10*T nm^3 (T represents the thickness of gold strip), we calculate the spatial drift currents intensity distributions and take the volumetric average of each area noted as $\boldsymbol{J}_{up}$ and $\boldsymbol{J}_{down}$, respectively. Therefore, the objective function is given in Equation 9 below.

$$\underset{x}{argmax}\left(\boldsymbol{J}_{up}-\boldsymbol{J}_{down}\right) \tag{9}$$

with $x=\left(L,G,W_{gold},T\right)$ being the dimension parameters of the nanostructure. Figure 6.20 below shows the best dimension parameters we have optimized.

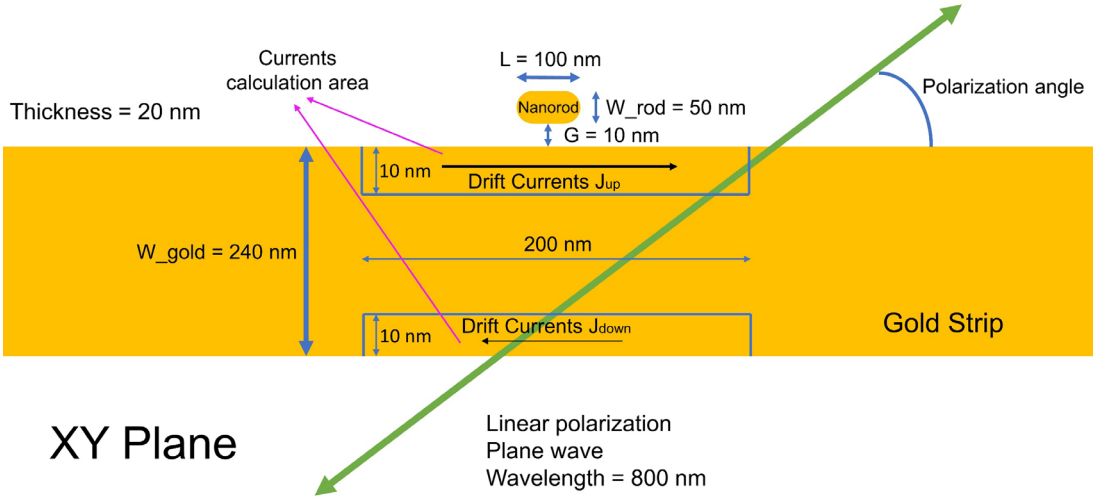

Figure 6.20 *: Schematic of an optimized nanostructure containing a gold nanostrip and a gold nanorod at an XY plane with the same thickness of 20 nm under a linear polarization of excitation.*

Moreover, a linearly polarized light launched right below the structure shown in Figure 6.20 with 45-degree and 135-degree polarization angles are used to perform the simulations. The light is a plane wave with centered wavelength of 800 nm. The peak power density is up to 10^{10} W/cm^2 and the pulse duration is 5.3 fs. Additionally, a Gaussian beam could also be used to replace the plane wave which will have nearly the same effect.

6.3.3 Simulation results and experimental results

The simulation results presented below in the Figure 6.21 are based on the best structure whose dimensions are given above in the Figure 6.20.

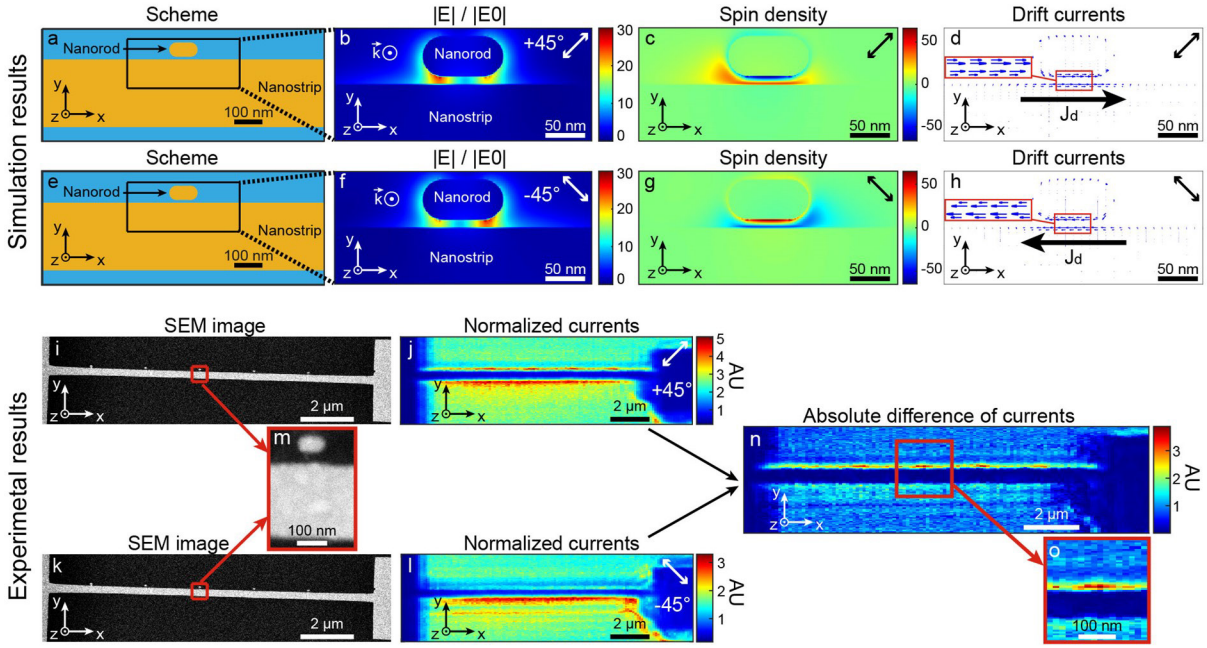

Figure 6.21 *: Plasmonic nanodevice for polarization-controlled photocurrent generation.*

As can be seen in the Figure 6.21, the sequence of subfigures Figure 6.21a-h illustrates the theoretical behavior of our nanodevice. In particular, a gold nanorod positioned close to a gold strip is depicted in Figure 6.21a and e. Figure 6.21b and f display the normalized electric field distributions in the gap between the nanorod and the gold strip for two linear polarizations, oriented at ±45° relative to the long axis of the nanorod upon incoming excitation along the z-axis. Figure 6.21c and g correspondingly show the spin densities in the gap for these excitation polarizations, revealing that the local polarizations in the gap are opposite depending on the linear polarization used. Overall, this setup results in the generation of drift currents within the gold strip, oriented in one direction or another based on the polarization orientations.

On the other hand, collaborating with Dr. Alexandre Bouhelier who is a CNRS research director from the laboratory Interdisciplinary Carnot de Bourgogne (ICB) in university of Bourgogne, we successfully fabricate some samples based on our optimized geometrical parameters using e-beam lithography technique and finished our first experiment for characterizing these photocurrents. The subfigures Figure 6.21i-o focus on the preliminary experimental investigations of this nanodevice mentioned above. Figure 6.21i, k and m feature Scanning Electron Microscope (SEM) images of gold nanorods adjacent to a gold strip, which is connected to electrodes for current measurement. The device is sequentially excited and scanned by a laser with each of the linear polarizations oriented at ±45 degrees from the long

axes of the nanorods. For each laser position, the current flowing through the gold strip is recorded, as shown in Figure 6.21j and l. Given that the thermal effects of gold can also generate photocurrents, Figure 6.21n presents the differential currents measured for each polarization, effectively isolating the thermal contribution. This differential measurement reveals current hot spots at the positions of the nanorods, as seen in Figure 6.21o, significantly indicating the presence of drift currents induced by the nanorods in the gold strip. These findings are preliminary and further experimentation is needed to confirm these results in the future.

6.4 Conclusion

In summary, in this chapter, we demonstrate that unidirectional drift photocurrents are generated through two different nanostructures due to the inverse Faraday effect at the nanoscale.

On the one hand, for the complex inversely designed plasmonic nano-antenna shown in section 6.2 based on topology optimization solved by genetic algorithm, strong unidirectional drift photocurrents are generated at the center of the structure only under a right circular polarization of excitation presenting a chirality which implies that the drift photocurrents can be generated through the nanostructure even under unpolarized light excitations (principle of chirality). In addition to that, it's also demonstrated that the unidirectional drift currents within femtosecond regime generated by the inversely designed plasmonic nanostructure can be used as a tunable THz nano source paving the way for potential applications such as ultra-localized THz spectroscopy at the nanoscale and so on.

On the other hand, for the nanostructure of gold nanostrip and gold nanorods shown in the section 6.3, inspired by the nanostructure shown in the section 6.2 and a recent theoretical work regarding to the linear inverse Faraday effect from our group, two different linear polarizations of excitation with 45-degree polarization angle and 135-degree polarization angle are applied to the nanostructure respectively in order to detect and measure the unidirectional drift currents experimentally. Thanks to the sample nanofabricated with high quality by Alexandre Bouhelier's group using the e-beam lithography technique, the experimental results are in a relatively good agreement with the FDTD simulation results.

Last but not least, more experiments are still ongoing and moving fast in collaboration with Alexandre Bouhelier's group in the laboratory Interdisciplinary Carnot de Bourgogne in

the university of Bourgogne and some advanced techniques such as light polarization modulation will be probably utilized to improve the accuracy and quality of experimental results in the future.

Chapter 7 General conclusion and perspective

The core of my Ph.D. thesis is on studying theoretically and experimentally the inverse Faraday effect at the nanoscale using inversely designed plasmonic nano-antennas. The stationary magnetic fields induced by stationary drift currents can be estimated according to the well-known Biot-Savart law. The stationary magnetic fields generated by plasmonic antennas at the nanoscale and within the femtosecond time range could open the door to ultrafast data storage, ultrafast data processing as well as nano-MRI studies.

In the chapter 1, the motivation of my Ph.D. research is well described. After that, in the chapter 2, the principle of the inverse Faraday effect is introduced at the beginning and the origin of the inverse Faraday effect in metals is then described with a simplified version of drift currents theory. The drift currents formula deduction process inspired by the R. Hertel's paper published in 2006 is also given. The stationary magnetic fields induced by the drift currents can be easily estimated through the Biot-Savart law. Besides that, two recent papers published by our group about the inverse Faraday effect in plasmonic nano-antennas are reviewed in order to better understand the inverse Faraday effect phenomena at the nanoscale and within femtosecond regime. In the chapter 3, to start with, the Finite-Difference Time-Domain (FDTD) is introduced as the numerical method for my Ph.D. projects' simulations due to its high performance in optical simulations. After that, the basic components of the commercial software Lumerical FDTD from ANSYS company are covered as well. Finally, the optimization part including the topology optimization, metaheuristic algorithms such as particle swarm optimization and genetic algorithm which is applied to all my projects as well as the objective function which is the most import part in the inverse design process of plasmonic nano-antennas are also described as preparation part for the following chapters of sub-projects.

In the chapter 4, 5 and 6, three different sub-projects about the inverse Faraday effect in inverse-designed plasmonic nano-antennas realized during my Ph.D. are presented. Due to the plasmonic nano-antenna's ability of manipulating light locally, the inverse Faraday effect phenomena can be easily controlled at the nanoscale and manipulated on demand as well.

Specifically, in the chapter 4, a chiral inverse Faraday effect mediated by an inversely designed plasmonic nano-antenna (Figure 7.1) is theoretically predicted for the very first time. In that sub-project, we demonstrate that by manipulating the spin density of light in a plasmonic

nanostructure, we generate a chiral inverse Faraday effect, creating a strong stationary magnetic field of 6 mT only for one helicity of the incoming light, the opposite helicity producing this effect only for the mirror nanostructure. This new optical concept opens the way to the generation of stationary magnetic fields with even unpolarized light, finding application in the ultrafast manipulation of magnetic domains and processes.

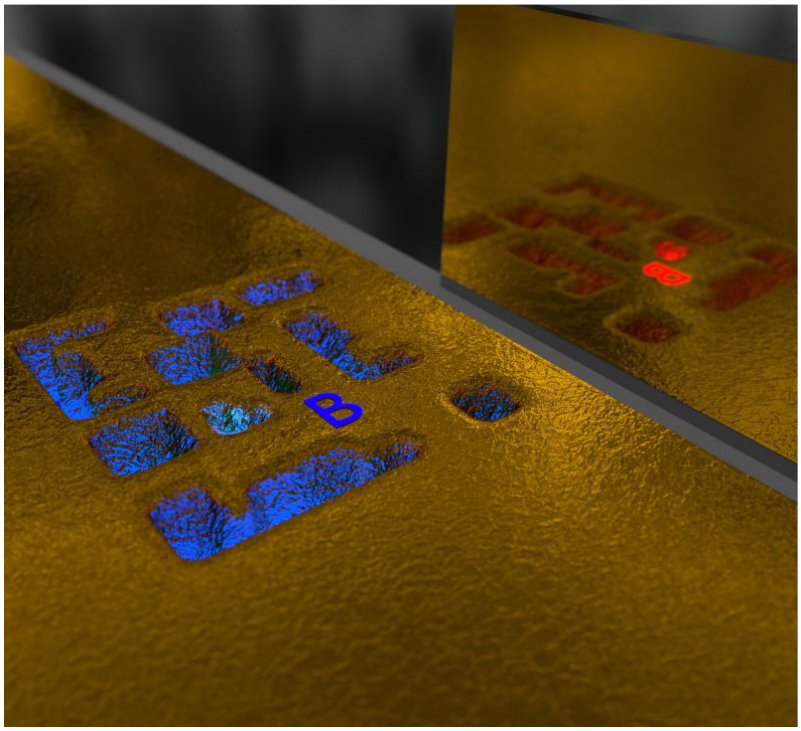

Figure 7.1 *: A chiral inverse Faraday effect mediated by an inversely designed plasmonic nano-antenna shown in the blue aera and its mirror structure presented in the red aera at its right side will generate same effect for another helicity of incoming light.*

Likewise, in the chapter 5, a reversed inverse Faraday effect with respect to the so-called "classic" inverse Faraday effect is theoretically observed with a GA-optimized plasmonic nano-antenna demonstrating that the static magnetization of matter by optical excitation can be of opposite symmetry to what has been commonly assumed (Figure 7.2). This symmetry reversal is made possible also by manipulating light at the nanoscale in a plasmonic nano-antenna which is similar to the one described in the chapter 4. Also, it demonstrates that this new physical phenomenon is still chiral, generating a strong stationary magnetic field only for one helicity of the incident wave, the opposite helicity producing this effect only for the mirror nanostructure.

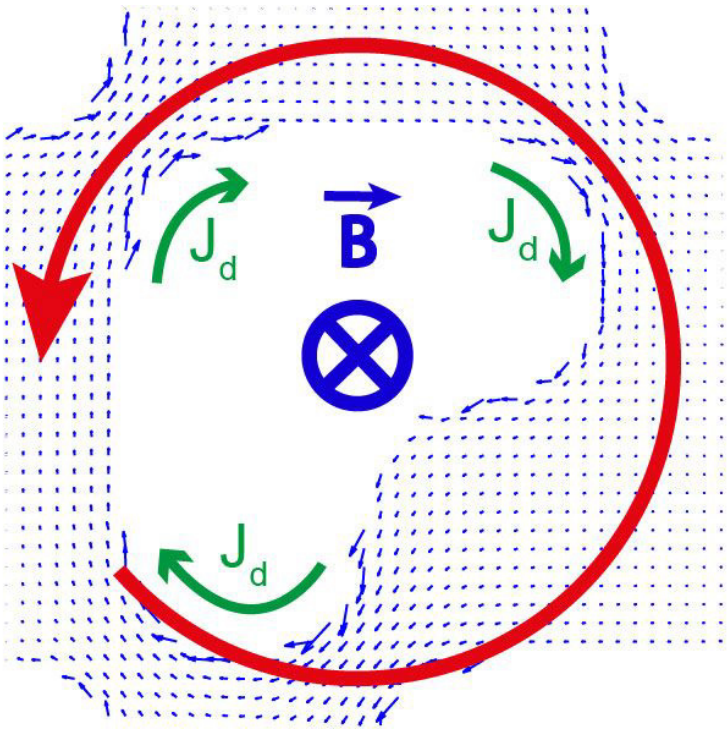

Figure 7.2 *: A reversed inverse Faraday effect is generated through the clockwise reversed drift currents symbolized by the blue arrows and green arrows thus stationary magnetic fields oriented inward is created only under a counterclockwise circular polarization of excitation represented by the red arrow. The length of the blue arrows refers to the relative amplitude of drift currents.*

In addition, in the chapter 6, two different nanostructures, which can generate unidirectional drift photocurrents unlike the circulating drift currents shown in the previous chapters, are both discussed. For the nanostructure made of gold nanostrip and gold nanorods, the experimental results, which are obtained in collaboration with Alexandre Bouhelier's group in the laboratory Interdisciplinary Carnot de Bourgogne, show a good agreement with FDTD simulation results that we acquired in our laboratory. For the complex plasmonic nano-antenna based on topological optimization solved by genetic algorithm, the strong unidirectional currents (the yellow arrow shown in Figure 7.3) are observed theoretically and can be used as a tunable THz nano source for multiple promising applications in THz spectroscopy at the nanoscale.

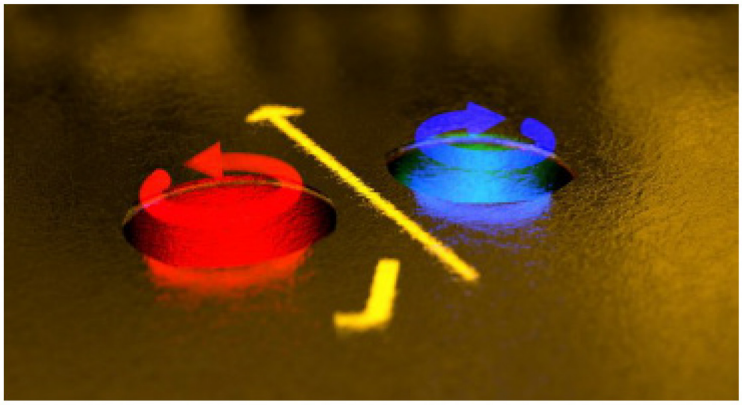

Figure 7.3 *: Unidirectional drift photocurrents symbolized by the straight yellow arrow is generated at the surface of a plasmonic nano-antenna due to its ability of manipulating light locally creating two opposite signs of spin density simultaneously at both sides of a central nanowire part.*

In parallel, my colleagues from Magnetic NanoLight group in our laboratory have already tried multiple nanofabrication methods such as lithography, focused ion beam and helium ion beam fabrication in order to get high quality samples of the GA-optimized structures described in this manuscript for the preparation of future experiments of the inverse Faraday effect in plasmonic nano-antennas. In addition to that, the first experiment of detecting drift currents using a relatively simple nanostructure has been conducted and more experiments for measuring the drift currents are in preparation. Moreover, the experiments for directly detecting the stationary magnetic field induced by the drift currents are also in preparation, and some potential techniques such as magnetic force microscopy, NV center magnetometry could be used in the future.

These series of future experiments can validate my simulation results and prove the inverse Faraday effect generated by plasmonic nano-antennas at the nanoscale. In addition, multiple projects about studying the inverse Faraday effect in plasmonic nano-antennas are still ongoing and moving fast. Furthermore, one of the Ph.D. students in our group has successfully designed a gold nanoring with specific dimensions and light excitations which can generate two opposite drift currents at two edges of the gold nanoring at the same plane thus creating a skymion topology of stationary magnetic field due to the inverse Faraday effect above the nanostructure.

In summary, based on all aspects mentioned above, my research opens a new door to better understand and manipulate the inverse Faraday effect in plasmonic nano-antennas paving a way to ultrafast data storage, ultrafast data processing as well as the generation of THz sources at the nanoscale in the future.

References

1. Pitaevskii, L.P., *Electric Forces in a Transparent Dispersive Medium.* Soviet Physics Jetp-Ussr, 1961. **12**(5): p. 1008-1013.
2. van der Ziel, J.P., P.S. Pershan, and L.D. Malmstrom, *Optically-Induced Magnetization Resulting from the Inverse Faraday Effect.* Physical Review Letters, 1965. **15**(5): p. 190-193.
3. Pershan, P.S., J.P. van der Ziel, and L.D. Malmstrom, *Theoretical Discussion of the Inverse Faraday Effect, Raman Scattering, and Related Phenomena.* Physical Review, 1966. **143**(2): p. 574-583.
4. Deschamps, J., M. Fitaire, and M. Lagoutte, *Inverse Faraday Effect in a Plasma.* Physical Review Letters, 1970. **25**(19): p. 1330-1332.
5. Tsytovich, V., *Magnetic-field generation in collisionless plasmas.* Comments on Plasma Physics and Controlled Fusion, 1978. **4**(3): p. 81-89.
6. Mora, P. and R. Pellat, *Ponderomotive effects and magnetic field generation in radiation plasma interaction.* The Physics of Fluids, 1979. **22**(12): p. 2408-2417.
7. Hertel, R., *Theory of the inverse Faraday effect in metals.* Journal of Magnetism and Magnetic Materials, 2006. **303**(1): p. L1-L4.
8. Ali, S., J.R. Davies, and J.T. Mendonca, *Inverse Faraday Effect with Linearly Polarized Laser Pulses.* Physical Review Letters, 2010. **105**(3): p. 035001.
9. Patel, S.K. and C. Argyropoulos, *Plasmonic nanoantennas: enhancing light-matter interactions at the nanoscale.* EPJ Applied Metamaterials, 2015. **2**: p. 4.
10. Sanz-Paz, M., T.S. van Zanten, C. Manzo, M. Mivelle, and M.F. Garcia-Parajo, *Broadband Plasmonic Nanoantennas for Multi-Color Nanoscale Dynamics in Living Cells.* Small, 2023. **19**(28): p. 2207977.
11. Dregely, D., K. Lindfors, M. Lippitz, N. Engheta, M. Totzeck, and H. Giessen, *Imaging and steering an optical wireless nanoantenna link.* Nature Communications, 2014. **5**(1): p. 4354.
12. Maksymov, I.S., *Magneto-plasmonic nanoantennas: Basics and applications.* Reviews in Physics, 2016. **1**: p. 36-51.
13. Xin, H., B. Namgung, and L.P. Lee, *Nanoplasmonic optical antennas for life sciences and medicine.* Nature Reviews Materials, 2018. **3**(8): p. 228-243.
14. Rasha, H.M. and A.J. Hussein, *Plasmonic Optical Nano-Antenna for Biomedical Applications*, in *Plasmonic Nanostructures*, S. Patrick, Editor. 2023, IntechOpen: Rijeka. p. Ch. 5.
15. Chen, Y., Y. Hu, J. Zhao, Y. Deng, Z. Wang, X. Cheng, D. Lei, Y. Deng, and H. Duan, *Topology Optimization-Based Inverse Design of Plasmonic Nanodimer with Maximum Near-Field Enhancement.* Advanced Functional Materials, 2020. **30**(23): p. 2000642.
16. Feichtner, T., O. Selig, and B. Hecht, *Plasmonic nanoantenna design and fabrication based on evolutionary optimization.* Optics Express, 2017. **25**(10): p. 10828-10842.
17. Earl, S.K., T.D. James, D.E. Gómez, R.E. Marvel, R.F. Haglund, Jr., and A. Roberts, *Switchable polarization rotation of visible light using a plasmonic metasurface.* APL Photonics, 2016. **2**(1): p. 016103.
18. Wang, M., R. Salut, H. Lu, M.-A. Suarez, N. Martin, and T. Grosjean, *Subwavelength polarization optics via individual and coupled helical traveling-wave nanoantennas.* Light: Science & Applications, 2019. **8**(1): p. 76.
19. Yang, L., H. Wang, Y. Fang, and Z. Li, *Polarization State of Light Scattered from Quantum Plasmonic Dimer Antennas.* ACS Nano, 2016. **10**(1): p. 1580-1588.

20. Kharintsev, S.S., A.I. Fishman, S.G. Kazarian, and M.K. Salakhov, *Polarization of near-field light induced with a plasmonic nanoantenna.* Physical Review B, 2015. **92**(11): p. 115113.
21. Sinha-Roy, R., J. Hurst, G. Manfredi, and P.-A. Hervieux, *Driving Orbital Magnetism in Metallic Nanoparticles through Circularly Polarized Light: A Real-Time TDDFT Study.* ACS Photonics, 2020. **7**(9): p. 2429-2439.
22. Cheng, O.H.-C., D.H. Son, and M. Sheldon, *Light-induced magnetism in plasmonic gold nanoparticles.* Nature Photonics, 2020. **14**(6): p. 365-368.
23. Hurst, J., P.M. Oppeneer, G. Manfredi, and P.-A. Hervieux, *Magnetic moment generation in small gold nanoparticles via the plasmonic inverse Faraday effect.* Physical Review B, 2018. **98**(13): p. 134439.
24. Nadarajah, A. and M.T. Sheldon, *Optoelectronic phenomena in gold metal nanostructures due to the inverse Faraday effect.* Optics Express, 2017. **25**(11): p. 12753-12764.
25. Smolyaninov, I.I., C.C. Davis, V.N. Smolyaninova, D. Schaefer, J. Elliott, and A.V. Zayats, *Plasmon-induced magnetization of metallic nanostructures.* Physical Review B, 2005. **71**(3): p. 035425.
26. Hertel, R. and M. Fähnle, *Macroscopic drift current in the inverse Faraday effect.* Physical Review B, 2015. **91**(2): p. 020411.
27. Hora, H., *Laser Plasma Physics: Forces and the Nonlinearity Principle*. Vol. PM250. 2016: SPIE Press. 350.
28. Karpman, V.I. and A.G. Shagalov, *The ponderomotive force of a high-frequency electromagnetic field in a cold magnetized plasma.* Journal of Plasma Physics, 1982. **27**(2): p. 215-224.
29. Tajima, T. and J.M. Dawson, *Laser Electron Accelerator.* Physical Review Letters, 1979. **43**(4): p. 267-270.
30. Hou, X., N. Djellali, and B. Palpant, *Absorption of Ultrashort Laser Pulses by Plasmonic Nanoparticles: Not Necessarily What You Might Think.* ACS Photonics, 2018. **5**(9): p. 3856-3863.
31. Labouret, T. and B. Palpant, *Nonthermal model for ultrafast laser-induced plasma generation around a plasmonic nanorod.* Physical Review B, 2016. **94**(24): p. 245426.
32. Yang, X.Y., Y. Mou, B. Gallas, A. Maitre, L. Coolen, and M. Mivelle, *Tesla-Range Femtosecond Pulses of Stationary Magnetic Field, Optically Generated at the Nanoscale in a Plasmonic Antenna.* ACS Nano, 2022. **16**(1): p. 386-393.
33. Yang, X.Y., Y. Mou, R. Zapata, B. Reynier, B. Gallas, and M. Mivelle, *An inverse Faraday effect generated by linearly polarized light through a plasmonic nano-antenna.* Nanophotonics, 2023. **12**(4): p. 687-694.
34. Kane, Y., *Numerical solution of initial boundary value problems involving Maxwell's equations in isotropic media.* IEEE Transactions on Antennas and Propagation, 1966. **14**(3): p. 302-307.
35. *Finite Difference Time Domain (FDTD) solver introduction*. Available from: https://optics.ansys.com/hc/en-us/articles/360034914633-Finite-Difference-Time-Domain-FDTD-solver-introduction.
36. Gedney, S.D., *Introduction to the Finite-Difference Time-Domain (FDTD) Method for Electromagnetics*. 2011.
37. Sullivan, D.M., *Electromagnetic Simulation Using the FDTD Method*. 2013.
38. Taflove, A., S.C. Hagness, and M. Piket-May, *9 - Computational Electromagnetics: The Finite-Difference Time-Domain Method*, in *The Electrical Engineering Handbook*, W.-K. Chen, Editor. 2005, Academic Press: Burlington. p. 629-670.

39. Johnson, S.G., *Notes on Perfectly Matched Layers (PMLs).* CoRR, 2021. **abs/2108.05348**.
40. Taflove, A. and S. Hagness, *Computational Electrodynamics: The Finite-Difference Time-Domain Method*. 3rd ed. 2005: Artech House Publishers. 1038 pages.
41. *Understanding Mesh Refinement and Conformal Mesh in FDTD*. Available from: https://optics.ansys.com/hc/en-us/articles/360034382594-Understanding-Mesh-Refinement-and-Conformal-Mesh-in-FDTD.
42. *Material Database in FDTD and MODE*. Available from: https://optics.ansys.com/hc/en-us/articles/360034394614-Material-Database-in-FDTD-and-MODE.
43. Rosinha, I.P., K.V. Gernaey, J.M. Woodley, and U. Krühne, *Topology optimization for biocatalytic microreactor configurations*, in *Computer Aided Chemical Engineering*, K.V. Gernaey, J.K. Huusom, and R. Gani, Editors. 2015, Elsevier. p. 1463-1468.
44. Rong, Y., Z.-L. Zhao, X.-Q. Feng, and Y.M. Xie, *Structural topology optimization with an adaptive design domain.* Computer Methods in Applied Mechanics and Engineering, 2022. **389**: p. 114382.
45. Zhang, W., J. Zhu, and T. Gao, *4 - Thermo-Elastic Problems*, in *Topology Optimization in Engineering Structure Design*, W. Zhang, J. Zhu, and T. Gao, Editors. 2016, Elsevier. p. 107-157.
46. Noh, J., T. Badloe, C. Lee, J. Yun, S. So, and J. Rho, *Chapter 1 - Inverse design meets nanophotonics: From computational optimization to artificial neural network*, in *Intelligent Nanotechnology*, Y. Zheng and Z. Wu, Editors. 2023, Elsevier. p. 3-32.
47. Aretz, K., S.M. Bartram, and P.F. Pope, *Asymmetric loss functions and the rationality of expected stock returns.* International Journal of Forecasting, 2011. **27**(2): p. 413-437.
48. Khachaturyan, A., S. Semenovsovskaya, and B. Vainshtein, *The thermodynamic approach to the structure analysis of crystals.* Acta Crystallographica Section A, 1981. **37**(5): p. 742-754.
49. Pincus, M., *Letter to the Editor—A Monte Carlo Method for the Approximate Solution of Certain Types of Constrained Optimization Problems.* Operations Research, 1970. **18**(6): p. 1225-1228.
50. Bonyadi, M.R. and Z. Michalewicz, *Particle Swarm Optimization for Single Objective Continuous Space Problems: A Review.* Evolutionary Computation, 2017. **25**(1): p. 1-54.
51. Mitchell, M., *An Introduction to Genetic Algorithms*. 1998: The MIT Press.
52. Kirkpatrick, S., C.D. Gelatt, and M.P. Vecchi, *Optimization by Simulated Annealing.* Science, 1983. **220**(4598): p. 671-680.
53. Perez, R.E. and K. Behdinan, *Particle swarm approach for structural design optimization.* Computers & Structures, 2007. **85**(19): p. 1579-1588.
54. Feichtner, T., O. Selig, M. Kiunke, and B. Hecht, *Evolutionary Optimization of Optical Antennas.* Physical Review Letters, 2012. **109**(12): p. 127701.
55. Abdel-Basset, M., L. Abdel-Fatah, and A.K. Sangaiah, *Chapter 10 - Metaheuristic Algorithms: A Comprehensive Review*, in *Computational Intelligence for Multimedia Big Data on the Cloud with Engineering Applications*, A.K. Sangaiah, M. Sheng, and Z. Zhang, Editors. 2018, Academic Press. p. 185-231.
56. Boeringer, D.W. and D.H. Werner, *Particle swarm optimization versus genetic algorithms for phased array synthesis.* IEEE Transactions on Antennas and Propagation, 2004. **52**(3): p. 771-779.
57. Desale, S.A., A. Rasool, S. Andhale, and P.V. Rane. *Heuristic and Meta-Heuristic Algorithms and Their Relevance to the Real World: A Survey*. 2015.

58. Hassan, R., B. Cohanim, O.d. Weck, and G. Venter, *A Comparison of Particle Swarm Optimization and the Genetic Algorithm*, in *46th AIAA/ASME/ASCE/AHS/ASC Structures, Structural Dynamics and Materials Conference*.
59. Panda, S. and N.P. Padhy, *Comparison of particle swarm optimization and genetic algorithm for FACTS-based controller design.* Applied Soft Computing, 2008. **8**(4): p. 1418-1427.
60. Ramdania, D.R., M. Irfan, F. Alfarisi, and D. Nuraiman, *Comparison of genetic algorithms and Particle Swarm Optimization (PSO) algorithms in course scheduling.* Journal of Physics: Conference Series, 2019. **1402**(2): p. 022079.
61. Bossini, D., V.I. Belotelov, A.K. Zvezdin, A.N. Kalish, and A.V. Kimel, *Magnetoplasmonics and Femtosecond Optomagnetism at the Nanoscale.* ACS Photonics, 2016. **3**(8): p. 1385-1400.
62. Beaurepaire, E., J.C. Merle, A. Daunois, and J.Y. Bigot, *Ultrafast Spin Dynamics in Ferromagnetic Nickel.* Physical Review Letters, 1996. **76**(22): p. 4250-4253.
63. Maccaferri, N., I. Zubritskaya, I. Razdolski, I.-A. Chioar, V. Belotelov, V. Kapaklis, P.M. Oppeneer, and A. Dmitriev, *Nanoscale magnetophotonics.* Journal of Applied Physics, 2020. **127**(8).
64. Mishra, K., R.M. Rowan-Robinson, A. Ciuciulkaite, C.S. Davies, A. Dmitriev, V. Kapaklis, A.V. Kimel, and A. Kirilyuk, *Ultrafast Demagnetization Control in Magnetophotonic Surface Crystals.* Nano Letters, 2022. **22**(23): p. 9773-9780.
65. Petrucci, G., A. Gabbani, I. Faniayeu, E. Pedrueza-Villalmanzo, G. Cucinotta, M. Atzori, A. Dmitriev, and F. Pineider, *Macroscopic magneto-chiroptical metasurfaces.* Applied Physics Letters, 2021. **118**(25).
66. Zubritskaya, I., N. Maccaferri, X. Inchausti Ezeiza, P. Vavassori, and A. Dmitriev, *Magnetic Control of the Chiroptical Plasmonic Surfaces.* Nano Letters, 2018. **18**(1): p. 302-307.
67. Kirilyuk, A., A.V. Kimel, and T. Rasing, *Ultrafast optical manipulation of magnetic order.* Reviews of Modern Physics, 2010. **82**(3): p. 2731-2784.
68. Fu, K.-M.C., S.M. Clark, C. Santori, C.R. Stanley, M.C. Holland, and Y. Yamamoto, *Ultrafast control of donor-bound electron spins with single detuned optical pulses.* Nature Physics, 2008. **4**(10): p. 780-784.
69. Lu, H.-I., I. Kozyryev, B. Hemmerling, J. Piskorski, and J.M. Doyle, *Magnetic Trapping of Molecules via Optical Loading and Magnetic Slowing.* Physical Review Letters, 2014. **112**(11): p. 113006.
70. Je, S.-G., P. Vallobra, T. Srivastava, J.-C. Rojas-Sánchez, T.H. Pham, M. Hehn, G. Malinowski, C. Baraduc, S. Auffret, G. Gaudin, S. Mangin, H. Béa, and O. Boulle, *Creation of Magnetic Skyrmion Bubble Lattices by Ultrafast Laser in Ultrathin Films.* Nano Letters, 2018. **18**(11): p. 7362-7371.
71. Temnov, V.V., *Ultrafast acousto-magneto-plasmonics.* Nature Photonics, 2012. **6**(11): p. 728-736.
72. Ishii, T., H. Yamakawa, T. Kanaki, T. Miyamoto, N. Kida, H. Okamoto, M. Tanaka, and S. Ohya, *Ultrafast magnetization modulation induced by the electric field component of a terahertz pulse in a ferromagnetic-semiconductor thin film.* Scientific Reports, 2018. **8**(1): p. 6901.
73. Khorsand, A.R., M. Savoini, A. Kirilyuk, A.V. Kimel, A. Tsukamoto, A. Itoh, and T. Rasing, *Role of Magnetic Circular Dichroism in All-Optical Magnetic Recording.* Physical Review Letters, 2012. **108**(12): p. 127205.
74. Fechner, M., A. Sukhov, L. Chotorlishvili, C. Kenel, J. Berakdar, and N.A. Spaldin, *Magnetophononics: Ultrafast spin control through the lattice.* Physical Review Materials, 2018. **2**(6): p. 064401.

75. Greilich, A., S.E. Economou, S. Spatzek, D.R. Yakovlev, D. Reuter, A.D. Wieck, T.L. Reinecke, and M. Bayer, *Ultrafast optical rotations of electron spins in quantum dots.* Nature Physics, 2009. **5**(4): p. 262-266.
76. Schellekens, A.J., K.C. Kuiper, R.R.J.C. de Wit, and B. Koopmans, *Ultrafast spin-transfer torque driven by femtosecond pulsed-laser excitation.* Nature Communications, 2014. **5**(1): p. 4333.
77. Satoh, T., Y. Terui, R. Moriya, B.A. Ivanov, K. Ando, E. Saitoh, T. Shimura, and K. Kuroda, *Directional control of spin-wave emission by spatially shaped light.* Nature Photonics, 2012. **6**(10): p. 662-666.
78. Collins, J.T., C. Kuppe, D.C. Hooper, C. Sibilia, M. Centini, and V.K. Valev, *Chirality and Chiroptical Effects in Metal Nanostructures: Fundamentals and Current Trends.* Advanced Optical Materials, 2017. **5**(16): p. 1700182.
79. Bonod, N., S. Bidault, G.W. Burr, and M. Mivelle, *Evolutionary Optimization of All-Dielectric Magnetic Nanoantennas.* Advanced Optical Materials, 2019. **7**(10): p. 1900121.
80. Wiecha, P.R., A. Arbouet, C. Girard, A. Lecestre, G. Larrieu, and V. Paillard, *Evolutionary multi-objective optimization of colour pixels based on dielectric nanoantennas.* Nature Nanotechnology, 2017. **12**(2): p. 163-169.
81. Krüger, J., D. Dufft, R. Koter, and A. Hertwig, *Femtosecond laser-induced damage of gold films.* Applied Surface Science, 2007. **253**(19): p. 7815-7819.
82. Poole, P., S. Trendafilov, G. Shvets, D. Smith, and E. Chowdhury, *Femtosecond laser damage threshold of pulse compression gratings for petawatt scale laser systems.* Optics Express, 2013. **21**(22): p. 26341-26351.
83. Ernandes, C., H.-J. Lin, M. Mortier, P. Gredin, M. Mivelle, and L. Aigouy, *Exploring the Magnetic and Electric Side of Light through Plasmonic Nanocavities.* Nano Letters, 2018. **18**(8): p. 5098-5103.
84. Sanz-Paz, M., C. Ernandes, J.U. Esparza, G.W. Burr, N.F. van Hulst, A. Maitre, L. Aigouy, T. Gacoin, N. Bonod, M.F. Garcia-Parajo, S. Bidault, and M. Mivelle, *Enhancing Magnetic Light Emission with All-Dielectric Optical Nanoantennas.* Nano Letters, 2018. **18**(6): p. 3481-3487.
85. Singh, A., P.M. de Roque, G. Calbris, J.T. Hugall, and N.F. van Hulst, *Nanoscale Mapping and Control of Antenna-Coupling Strength for Bright Single Photon Sources.* Nano Letters, 2018. **18**(4): p. 2538-2544.
86. Curto, A.G., G. Volpe, T.H. Taminiau, M.P. Kreuzer, R. Quidant, and N.F. van Hulst, *Unidirectional Emission of a Quantum Dot Coupled to a Nanoantenna.* Science, 2010. **329**(5994): p. 930-933.
87. García-Guirado, J., M. Svedendahl, J. Puigdollers, and R. Quidant, *Enantiomer-Selective Molecular Sensing Using Racemic Nanoplasmonic Arrays.* Nano Letters, 2018. **18**(10): p. 6279-6285.
88. García-Guirado, J., M. Svedendahl, J. Puigdollers, and R. Quidant, *Enhanced Chiral Sensing with Dielectric Nanoresonators.* Nano Letters, 2020. **20**(1): p. 585-591.
89. Hanke, T., G. Krauss, D. Träutlein, B. Wild, R. Bratschitsch, and A. Leitenstorfer, *Efficient Nonlinear Light Emission of Single Gold Optical Antennas Driven by Few-Cycle Near-Infrared Pulses.* Physical Review Letters, 2009. **103**(25): p. 257404.
90. Ma, Q., R. Krishna Kumar, S.-Y. Xu, F.H.L. Koppens, and J.C.W. Song, *Photocurrent as a multiphysics diagnostic of quantum materials.* Nature Reviews Physics, 2023. **5**(3): p. 170-184.
91. Yu, W.J., Q.A. Vu, H. Oh, H.G. Nam, H. Zhou, S. Cha, J.-Y. Kim, A. Carvalho, M. Jeong, H. Choi, A.H. Castro Neto, Y.H. Lee, and X. Duan, *Unusually efficient*

photocurrent extraction in monolayer van der Waals heterostructure by tunnelling through discretized barriers. Nature Communications, 2016. **7**(1): p. 13278.
92. Zhang, Y., T. Holder, H. Ishizuka, F. de Juan, N. Nagaosa, C. Felser, and B. Yan, *Switchable magnetic bulk photovoltaic effect in the two-dimensional magnet CrI3.* Nature Communications, 2019. **10**(1): p. 3783.
93. Kastl, C., C. Karnetzky, H. Karl, and A.W. Holleitner, *Ultrafast helicity control of surface currents in topological insulators with near-unity fidelity.* Nature Communications, 2015. **6**(1): p. 6617.
94. Watanabe, H. and Y. Yanase, *Chiral Photocurrent in Parity-Violating Magnet and Enhanced Response in Topological Antiferromagnet.* Physical Review X, 2021. **11**(1): p. 011001.
95. Sun, D., G. Aivazian, A.M. Jones, J.S. Ross, W. Yao, D. Cobden, and X. Xu, *Ultrafast hot-carrier-dominated photocurrent in graphene.* Nature Nanotechnology, 2012. **7**(2): p. 114-118.
96. Son, B.H., J.-K. Park, J.T. Hong, J.-Y. Park, S. Lee, and Y.H. Ahn, *Imaging Ultrafast Carrier Transport in Nanoscale Field-Effect Transistors.* ACS Nano, 2014. **8**(11): p. 11361-11368.
97. Joshi, S. and G. Moddel, *Optical rectenna operation: where Maxwell meets Einstein.* Journal of Physics D: Applied Physics, 2016. **49**(26): p. 265602.
98. Stolz, A., J. Berthelot, M.-M. Mennemanteuil, G. Colas des Francs, L. Markey, V. Meunier, and A. Bouhelier, *Nonlinear Photon-Assisted Tunneling Transport in Optical Gap Antennas.* Nano Letters, 2014. **14**(5): p. 2330-2338.
99. Marinica, D.C., M. Zapata, P. Nordlander, A.K. Kazansky, P. M. Echenique, J. Aizpurua, and A.G. Borisov, *Active quantum plasmonics.* Science Advances, 2015. **1**(11): p. e1501095.
100. Gunyaga, A.A., M.V. Durnev, and S.A. Tarasenko, *Photocurrents induced by structured light.* Physical Review B, 2023. **108**(11): p. 115402.
101. Février, P., J. Basset, J. Estève, M. Aprili, and J. Gabelli, *Role of optical rectification in photon-assisted tunneling current.* Communications Physics, 2023. **6**(1): p. 29.
102. Mennemanteuil, M.M., M. Buret, G. Colas-des-Francs, and A. Bouhelier, *Optical rectification and thermal currents in optical tunneling gap antennas.* 2022. **11**(18): p. 4197-4208.
103. Mou, Y., X.Y. Yang, B. Gallas, and M. Mivelle, *A Reversed Inverse Faraday Effect.* Advanced Materials Technologies, 2023.
104. Mou, Y., X.Y. Yang, B. Gallas, and M. Mivelle, *A chiral inverse Faraday effect mediated by an inversely designed plasmonic antenna.* Nanophotonics, 2023. **12**(12): p. 2115-2120.
105. Mora, P. and R. Pellat, *Ponderomotive effects and magnetic field generation in radiation plasma interaction.* Physics of Fluids, 1979. **22**: p. 2408-2417.
106. Bryche, J.-F., M. Vega, J. Moreau, P.-L. Karsenti, P. Bresson, M. Besbes, P. Gogol, D. Morris, P.G. Charette, and M. Canva, *Ultrafast Heat Transfer at the Nanoscale: Controlling Heat Anisotropy.* ACS Photonics, 2023. **10**(4): p. 1177-1186.
107. Kimel, A.V. and M. Li, *Writing magnetic memory with ultrashort light pulses.* Nature Reviews Materials, 2019. **4**(3): p. 189-200.
108. Mangin, S., M. Gottwald, C.H. Lambert, D. Steil, V. Uhlíř, L. Pang, M. Hehn, S. Alebrand, M. Cinchetti, G. Malinowski, Y. Fainman, M. Aeschlimann, and E.E. Fullerton, *Engineered materials for all-optical helicity-dependent magnetic switching.* Nature Materials, 2014. **13**(3): p. 286-292.

109. Davis, T.J. and E. Hendry, *Superchiral electromagnetic fields created by surface plasmons in nonchiral metallic nanostructures.* Physical Review B, 2013. **87**(8): p. 085405.
110. Wang, F.X., F.J. Rodríguez, W.M. Albers, R. Ahorinta, J.E. Sipe, and M. Kauranen, *Surface and bulk contributions to the second-order nonlinear optical response of a gold film.* Physical Review B, 2009. **80**(23): p. 233402.
111. Fülöp, J.A., S. Tzortzakis, and T. Kampfrath, *Laser-Driven Strong-Field Terahertz Sources.* Advanced Optical Materials, 2020. **8**(3): p. 1900681.

[Manipuler l'effet Faraday inverse par l'utilisation de nanostructures plasmoniques inversement conçues]

Résumé:
L'effet Faraday inverse est un processus magnéto-optique permettant la magnétisation de la matière par une excitation optique porteuse d'un spin non nul de la lumière. Cette interaction lumière-matière dans les métaux à l'échelle nanométrique résulte de la création de courants de dérive via les forces non linéaires que la lumière applique aux électrons de conduction. En particulier, ce phénomène a été considéré jusqu'à présent comme symétrique; les polarisations circulaires droite ou gauche génèrent des champs magnétiques orientés dans la direction de propagation de la lumière ou dans la direction opposée à la propagation. Nous démontrons ici qu'en manipulant localement la densité de spin de la lumière dans des nano-antennes plasmoniques inversement conçues, l'effet Faraday inverse peut être chiral et générer de forts champs magnétiques stationnaires dus aux courants de dérive uniquement pour une hélicité de la lumière entrante; nous démontrons aussi que ce processus magnéto-optique peut avoir sa symétrie inversée, ce qui était considéré comme impossible; et qu'il peut même générer des photocourants de dérive unidirectionnels en tant que nano-source accordable pour un rayonnement THz linéaire. Ce nouveau concept optique de manipulation de l'effet Faraday inverse par des nano-antennes plasmoniques trouve diverses applications dans le contrôle ultrarapide des domaines magnétiques, non seulement dans les technologies de stockage de données ultrarapides, mais aussi dans des domaines de recherche tels que la spectroscopie THz à l'échelle nanométrique, le piégeage magnétique, les skyrmions magnétiques, le dichroïsme circulaire magnétique, la manipulation de matériaux magnétiques, le contrôle du spin, la précession du spin, les courants de spin et les ondes de spin, entre autres.
Mots clés: [Interaction Lumière-Matière, Effet Faraday Inverse, Nanostructure Plasmonique, Conception Inverse, Chiralité, Champ Magnétique Stationnaire]

[Manipulating the inverse Faraday effect using inversely designed plasmonic nanostructures]

Abstract:
The inverse Faraday effect is a magneto-optical process allowing for the magnetization of matter through optical excitation carrying a non-zero spin of light. This light-matter interaction in metals at the nanoscale arises from the generation of drift currents via the nonlinear forces applied by light to the conduction electrons. Particularly, this phenomenon has been conventionally considered symmetrical; right or left circular polarizations generate magnetic fields oriented either in the direction of light propagation or in the direction opposite to propagation. We demonstrate here that by locally manipulating the spin density of light in inversely designed plasmonic nano-antennas, the inverse Faraday effect can be chiral and generate strong stationary magnetic fields due to drift currents only for one helicity of incoming light; furthermore, we demonstrate that this magneto-optical process can have its symmetry reversed, which was considered impossible; and it can even generate unidirectional drift photocurrents as a tunable nano-source for linear THz radiation. This novel optical concept of manipulating the inverse Faraday effect by plasmonic nano-antennas finds diverse applications in ultrafast control of magnetic domains, not only in ultrafast data storage technologies but also in research areas such as nanoscale THz spectroscopy, magnetic trapping, magnetic skyrmions, magnetic circular dichroism, magnetic material manipulation, spin control, spin precession, spin currents, and spin waves, among others.
Keywords: [Light-Matter Interaction, Inverse Faraday Effect, Plasmonic Nanostructure, Inverse Design, Chirality, Stationary Magnetic Field]